

**INTERACTIVE FEEDBACKS OF CLIMATE, MINERALOGY, AND
MICROBIOLOGICAL COMMUNITIES ON SOIL CARBON:
A DEEP SOIL WARMING EXPERIMENT**

A THESIS SUBMITTED TO THE GRADUATE DIVISION OF THE
UNIVERSITY OF HAWAI‘I AT MĀNOA IN PARTIAL FULFILLMENT
OF THE REQUIREMENTS FOR THE DEGREE OF MASTER OF SCIENCE
IN
NATURAL RESOURCES AND ENVIRONMENTAL MANAGEMENT

December 2019

By

Casey R. McGrath

Thesis Committee:

Susan E. Crow, Chairperson

Nhu H. Nguyen

Carl I. Evensen

Keywords: climate change, soil carbon, Andisols, tropical soils, deep soil warming, Hawai‘i

ProQuest Number: 27548324

All rights reserved

INFORMATION TO ALL USERS

The quality of this reproduction is dependent on the quality of the copy submitted.

In the unlikely event that the author did not send a complete manuscript and there are missing pages, these will be noted. Also, if material had to be removed, a note will indicate the deletion.



ProQuest 27548324

Published by ProQuest LLC (2020). Copyright of the Dissertation is held by the Author.

All Rights Reserved.

This work is protected against unauthorized copying under Title 17, United States Code
Microform Edition © ProQuest LLC.

ProQuest LLC
789 East Eisenhower Parkway
P.O. Box 1346
Ann Arbor, MI 48106 - 1346



Graduate report, written in partial fulfillment of the degree requirements of the College of Tropical Agriculture and Human Resources, Department of Natural Resources and Environmental Management Master of Science.

DEDICATION

To Jeanne Eva McGrath, for teaching me to keep courage.

ACKNOWLEDGEMENTS

First and foremost, I would like to thank my thesis committee of Dr. Susan E. Crow, Dr. Nhu H. Nguyen and Dr. Carl I. Evensen for their mentorship. Dr. Nguyen generously provided lab space, knowledge and patiently invested many hours of discussion into the microbial development of this thesis. Dr. Evensen helped to get this project off the ground at the Lyon Arboretum and always provided a wealth of expertise to the thesis discussion. Committee chair, Dr. Crow, oversaw the development of both the project and myself as a person and consistently challenged me to think beyond the norm and to become a stronger woman in science.

I would especially like to thank Dr. Caitlin Hickes Pries of Dartmouth College, whom I consider an honorary thesis committee member, for letting me shadow her in the beginning of my graduate school journey and for her patience, knowledge and inspiration she willingly provided throughout the study. This study would not have progressed without the hard work of the Lyon Arboretum staff. Many thanks to Pia Ruisi-Beasres, Liloa Dunn, Uncle Rob, Uncle Nate, Hua and Tristan Williams for all their work in taking care of the fieldsite, as well as Dr. Rakan Zahawi and Jessica Adinolfi for their expertise and support.

A large part of this project is indebted to the members of the UH Manoa MESH Lab including Dr. Brian Glazer, Stanley Lio and Katherine Hardy. The development and programming of the sensor system is owed all to their hard work and patience. Also, thanks to Ryan Kurasaki of the UH Manoa Ag Engineering department for probe design and creation.

The success of this project was possible because of numerous project interns including Steven Attilio, Kaelin Sylva, and Garland Rogers. I would especially like to thank Mathilde Duvallet, for her intense dedication to the project during her 5 month internship. I would also like to thank my labmates, Hannah Hubanks, Daniel Richardson, Jon Wells, Elaine Vizka, Steven

Heisey, and Iswhora Dhungana, for their advice, compassion and friendship during these 2 years.

To Christine Tallamy Glazer, thank you for all your support in the lab, field and beyond.

Other NREM faculty who also provided invaluable insight include Dr. Creighton Litton, Dr. Russell Yost, Dr. Adel Yokahana, and Dr. Richard Kablan, who helped propel the project forward and NREM office staff of Megan Parker, Lisa Kam, Allision Arakawa, and Adrian Elduque who were always dedicated to taking care of the project's needs.

Finally, I would like to thank members of the Newman Holy Spirit Parish, my friends, and family for supporting me physically, emotionally and spiritually through my journey to become a better scientist, but more importantly, a better person.

ABSTRACT

Climate change conversely is the largest issue facing humanity today. Natural systems exist that could potentially sequester large reservoirs of carbon (C) from the atmosphere and aid in the preservation of global ecosystems while long term solutions to destructive human behavior are enacted into policy. Soils are one such system with high potential to drawdown carbon and reduce atmospheric greenhouse gas concentration. This benefit may only occur if the mechanisms for stabilizing and storing carbon are not overwhelmed by the interactive effects of rapid warming on multiple soil processes. Volcanic ash derived Andisols, with a high concentration of poorly and non-crystalline minerals, have a strong affinity to stabilize C and offer a unique study system to test hypotheses about mineral control on carbon stabilization and protection from disturbance losses (Giardina et al. 2014; Crow et al., 2015). Andisols unique affinity to C may hold the key in utilizing an understudied, but critical carbon sequestration management tool within the global C cycle.

Interactive feedbacks of climate, mineralogy, and microbial communities on the soil C balance will determine the net soil C balance under a changing environment. In Hawaiian Andisols organo-mineral associations are strong soil C-protection mechanisms leading to large soil C stocks. Existing evidence from non-Andic soils suggests that increased soil temperature escalates microbial activity in the soil and consequently soil respiration rates throughout the soil profile, implying declining C stocks if metabolic losses outweigh input gains. However, how the intensive warming predicted with climate change by 2100 will impact C cycling and storage in Andisols is unknown. On a 200 m² hillslope of a wet montane Andisol, soil was heated using a randomized design that allowed for a temperature gradient of ambient to +4°C across sampling depths (20, 40, 60, 80, and 100 cm). After a year of deep soil warming during which soil respiration and flux

throughout the soil profile was measured, the warming response ranged from 0.89 to 17,000 mg CO₂ m⁻³ hr⁻¹ across the gradient of temperature and depth. Generalized additive modeling (GAM), indicated that overall, the amount of C released from the soil did not significantly increase in response to warming at depth. GAM also confirmed the hypothesis that poorly and non-crystalline minerals (hydroxylamine hydrochloride extractable Al + 0.5Fe, and the active Fe ratio), derived from the volcanic ash parent material, was the primary driver of the lack of CO₂ response. Another significant driver limiting the CO₂ response was ΔpH (pH_{KCl} - pH_{H2O}), with possible positive net colloid charges stabilizing organic matter. Bacterial and fungal diversity measured by high-throughput sequencing at 20 and 40cm were significantly more diverse than those at 60, 80 and 100cm. The significant relationship of mean CO₂ produced in response to warming and poorly and non-crystalline minerals suggests the strong organo-mineral protection mechanisms found in Hawaiian Andisols could be considered as a C management tool.

TABLE OF CONTENTS

ACKNOWLEDGEMENTS.....	iv
ABSTRACT.....	vi
TABLE OF CONTENTS.....	viii
LIST OF TABLES	x
LIST OF FIGURES	xi
CHAPTER 1 : LITERATURE REVIEW	1
1.1 Climate Change and Global Temperature Rise	1
1.2 Global Soil C Cycle	4
1.3 Soil Microbial Communities.....	10
1.4 International Soil Experimental Network (iSEN).....	11
1.5 Importance of Tropical Soils: Hawaiian Andisols.....	13
CHAPTER 2 : SURFICIAL SEASONALITY OF AN ANDISOL.....	19
2.1 Introduction.....	20
2.2 Objectives and Hypotheses	22
2.2.1 Objective.....	22
2.2.2 Hypothesis.....	22
2.2.3 Prediction	22
2.2.4 Justification	22
2.2.5 Approach.....	23
2.3 Methods.....	24
2.3.1 Site Selection and Description	24
2.3.2 Field Methods	26
2.4 Results.....	30
2.5 Discussion	41
2.6 Conclusion	42
CHAPTER 3 : NOVEL, LOW COST SENSOR NETWORK.....	43
3.1 Introduction.....	44
3.3 Methods.....	46
3.3.1 Fieldsite design	46
3.4 Results and discussion	53
3.5 Conclusion	57

CHAPTER 4 : INTERACTIVE FEEDBACKS OF CLIMATE, MINERALOGY AND MICROBIAL COMMUNITIES ON SOIL CARBON.....	60
4.1 Introduction.....	61
4.2 Objectives and Hypotheses	63
4.2.1 Objective	63
4.2.2 Hypothesis.....	63
4.2.3 Prediction	63
4.2.4 Justification.....	64
4.2.5 Approach.....	65
4.3 Methods.....	66
4.3.1 Field Sampling	66
4.3.2. Laboratory Analysis.....	67
4.3.3 Data Analysis	70
4.4 Results.....	75
4.4.1 Interactive effects of warming on CO ₂ produced	75
4.4.2 Microbial depth dependence	97
4.5 Discussion	104
4.6 Conclusion	112
LITERATURE CITED	117
APPENDIX A. The depths associated with each sample ID.....	122
APPENDIX B. Fick's law CO ₂ production calculations.....	124
APPENDIX C. Quality check plots for the top three optimization equations.....	125
APPENDIX D. Qiime 2.0 ITS pipeline taken from Nhu Nhogen Microbiology lab	127
APPENDIX E. Qiime 2.0 16S pipeline taken from Nhu Nhogen Microbiology lab	132

LIST OF TABLES

Table 4.1 Timeseries parameters from weekly sampling at fieldsite	73
Table 4.2 One time soil sampling parameter results.	74
Table 4.3 Table of the top ten model iterations from the global model dredging.....	89
Table 4.4 Table of the models of the strongest terms from “maunal” dredging.....	91
Table 4.5 Summary of 16S and ITS sequencing results.	102
Table 4.6 Summary of count of species found per guild (ITS).....	102

LIST OF FIGURES

Figure 1.1 RCP 8.5 model predictions for average changes in global air and soil temperature....	4
Figure 1.2 Global aboveground biomass and belowground SOC stocks.....	6
Figure 1.3 Microbial respiration response rate to an increase in temperature across biomes.....	9
Figure 1.4 Distribution of the 10 soil orders found in the Hawaiian archipelago.....	18
Figure 2.1 Sampling the collars via the GRACENet protocol	19
Figure 2.2 Seasonal variation in soil respiration as predicted by Davidson et al.	21
Figure 2.3 Location of the fieldsite at the Lyon Arboretum, Honolulu, HI.....	24
Figure 2.4 Site development shown before clearing and after clearing.....	25
Figure 2.5 Contour map of Lyon Arboretum fieldsite.....	26
Figure 2.6 Collar for GRACENet protocoland 130cm soil pit	29
Figure 2.7 Heatmaps of the surficial CO ₂ flux form Sept '17 to Sept '18.....	33
Figure 2.8 Evidence of ungulate disturbance on February and March 2018.	34
Figure 2.9 The mean flux, soil temperature, and moisture of the static chambers	34
Figure 2.10 Heatmaps of the surficial CO ₂ flux.....	37
Figure 2.11 ACF plot of the mean flux of CO ₂ timeseries	38
Figure 2.12 The decomposed timeseries of the mean flux of CO ₂	39
Figure 2.13 Soil pit profiles from 0 to 130cm at the Lyon Arboretum fieldsite.....	40
Figure 3.1 Soldering the cable to the soil temperature sensor	43
Figure 3.2 Randomization design for the hillslope at Lyon Arboretum	47
Figure 3.3 Diagram of the 2.5m heating probe with monitoring temperature sensor.....	48
Figure 3.4 The temperature sensors, dataloggers and control center.....	50
Figure 3.5 Livestream database of the real time soil temperatures.....	50

Figure 3.6 Gas well design at the Lyon Arboretum.....	52
Figure 3.7 Average soil temperature for ambient soil temperature sensors and heater	53
Figure 3.8 Δ soil temperature between average ambient and heated soil temperatures	53
Figure 3.9 Average soil temperature across the fieldsite	55
Figure 3.10 Average Δ soil temperature and average volumetric water content	56
Figure 4.1 Looking upslope at the fieldsite at the Lyon Arboretum.....	60
Figure 4.2 Relationship between soil respiration and intensified warming over time.....	64
Figure 4.3 Soil sampling using the JMC Environmentalist's Subsoil Probe.....	66
Figure 4.4 Sodium pyrophosphate extractions.....	69
Figure 4.5 Soil temperature raw data timeseries at each depth across the fieldsite.....	75
Figure 4.6 The seasonality of soil temperature at the fieldsite by depth	76
Figure 4.7 Volumetric water content (VWC) raw data timeseries at each depth	77
Figure 4.8 The seasonality of volumetric water content (VWC) at the fieldsite	78
Figure 4.9 CO ₂ produced by depth section for the raw data timeseries.....	79
Figure 4.10 Correlation matrix for the mean seasonally adjusted timeseries parameters.....	80
Figure 4.11 PCA of the parameters considered for model analysis	81
Figure 4.12 Δ CO ₂ produced vs. Δ seasonally adjusted temperature over time.....	82
Figure 4.13 CO ₂ produced plotted against non-crystalline concentration.	83
Figure 4.14 Mean CO ₂ produced against the active Fe ratio with a GAM smoother.	84
Figure 4.15 Mean CO ₂ produced against Δ pH with a GAM smoother.....	85
Figure 4.16 Quality check plots for global model of log(CO ₂) response	86
Figure 4.17 Smoothers fit for each parameter of the global model individually	86
Figure 4.18 Results of global model dredge using “MuMIn” package in R.....	88

Figure 4.19 Log-transformed CO ₂ produced plotted against Δ soil temperature)	93
Figure 4.20 Log-transformed CO ₂ produced plotted against Δ pH	94
Figure 4.21 Log-transformed CO ₂ produced plotted against Active Fe ratio.....	94
Figure 4.22 Log-transformed CO ₂ produced plotted against non-crystalline mineral.....	95
Figure 4.23 Log-transformed CO ₂ produced plotted against carbon	95
Figure 4.24 CO ₂ produced plotted against the top predictors of CO ₂ produced at the fieldsite ..	96
Figure 4.26 Alpha rarefaction curve for observed taxonomic units for 16S.....	97
Figure 4.27 Alpha rarefaction curve for observed taxonomic units for ITS	98
Figure 4.28 Boxplot of Shannon Diversity Index (H') for 16S (bacteria) data	99
Figure 4.29 Boxplot of Shannon Diversity Index (H') for ITS (fungi) data.....	99
Figure 4.30 Boxplot of Species Richness (S) for 16S data.....	100
Figure 4.31 Boxplot of Species Richness (S) for ITS data	101
Figure 4.32 Relative bacterial activity and relative fungal activity (Pietikainen et al, 2005)....	110

CHAPTER 1 : LITERATURE REVIEW

1.1 CLIMATE CHANGE AND GLOBAL TEMPERATURE RISE

IPCC predictions in global air temperature

Climate change is the rise of average global temperatures and its wide-ranging impacts that have been witnessed within the last century. These global impacts include increased instance of natural disasters, rising sea levels, loss of biodiversity, higher prevalence of vector borne disease and other major effects that impact the wellbeing of society and global ecosystems. This rise in global temperature is mainly anthropogenically sourced from fossil fuel emissions which adds to the overall concentration of greenhouse gases (GHG). GHG absorb and emit thermal radiation trapping heat within the atmosphere and raise the global temperature. As we enter a new era of combating climate change, it is critical to understand the many nested positive feedback systems making up the Earth system that collectively can create issues for the sustainability of human societies.

An accelerated and necessary movement of international governmental bodies to develop stronger climate science predictions for the effects of GHG on nested positive feedback natural processes is underway. The Intergovernmental Panel on Climate Change (IPCC) , is the most widely recognized scientific and intergovernmental body in this effort. Since 1989, the IPCC has published five reports detailing the findings of the latest climate science through intensive collaboration within the scientific community. The most recent report predicts the global average temperature anomaly will increase 4°C, by 2100 (Pachauri et al., 2015) . This prediction represents “the business as usual model” (RCP 8.5) which is a likely scenario given the rise in GHG emissions over the last century.

Carbon dioxide (CO₂) as a powerful greenhouse gas

The last century witnessed exponential increases in GHG emissions. There was a dramatic increase in GHGs brought about by the economic and population growth of the industrial revolution. Through the burning of fossil fuels, there has been a great rise in the atmospheric concentration of carbon dioxide (CO₂). Fossil fuels contain extremely old carbon (C) that oxidizes into the atmosphere through combustion. The increased concentration of CO₂ in the atmosphere is unmistakably linked to this ancient C signature from the of burning fossil fuels. The IPCC reports that 78% of total GHG emissions from 1970 to 2010 originated from fossil fuels, and since pre-industrial times CO₂ levels in the atmosphere have increased by 40% (Pachauri et al., 2015)

CO₂ has the highest radiative forcing, or a net increase in the amount of energy reaching Earth's surface, out of all other GHGs. 40% of CO₂ emissions are retained in the atmosphere, 30% are absorbed by the ocean (contributing to ocean acidification) and the 30% are taken up by terrestrial systems (Pachauri et al., 2015). As CO₂ emissions continue to rise, there will be severe landscape and climatic shifts reinforcing strong positive feedback loops of many natural cycles.

Climate change in Hawaii

Hawaii is not immune to the destructive effects of climate change. As a small archipelago, Hawaii is more likely to have quicker, tangible effects of intensified natural disasters, sea level rise and loss of biodiversity compared to larger continents. Average air temperature in Hawaii has increased 0.17°C per decade in the last 40 years, bringing specific challenges to Hawaiian landscape and climate (Eversole and Andrews, 2014). Northeasterly trade winds and total precipitation have declined causing widespread drought. Even with an overall trend of drought, climatic shifts cause some areas to receive excessive rain resulting in flash floods that threaten

infrastructure and lives (Eversole and Andrews, 2014). These destructive effects are harming the natural systems Hawaii relies on for its economy.

One of the most critical natural resources to Hawaii's economy is the ocean. Threats to Hawaiian coastal and marine environments pose severe risks for its large fishing and tourism industry. Since the industrial revolution, the sea level has risen 1.5 to 3.3cm per decade and is expected to accelerate to 0.3 to 1m by the end of this century (Eversole and Andrews, 2014). This rise in sea level threatens those who live and work along the coast. Added to this, marine environments are taking up more CO₂ compared to pre-industrial eras causing ocean acidification with an expected pH decrease between 0.1 and 0.4 within the next century (Eversole and Andrews, 2014). Ocean acidification damages the biodiversity of coral reefs which are crucial to the health of Hawaii's fisheries. The extensive damage associated with climate change is a hazard to the health of Hawaii's economy and natural ecosystems.

Climate changes effects on soil

Climate change not only affects the atmosphere and ocean, it affects the living and breathing skin of the Earth, soil. Soils are comprised of minerals, organic solids, gases, liquids and living organisms. Soils are a medium for plant growth, engineering, organism habitat, filtering water, recycling nutrients, and facilitating interactions with atmospheric properties (Brady and Weil, 2005). It is imperative to understand the linkages between global climate change and soils. Global air temperature has been increasing only slightly faster than the temperature of shallow and deep soils (Figure 1). The anomalies in soil temperature at 1m of depth have been consistent across all soil types with those at the surface (Pries et al., 2017). This linkage between air and soil

temperatures demonstrates the importance to explore how soil processes may be affected by rising temperatures.

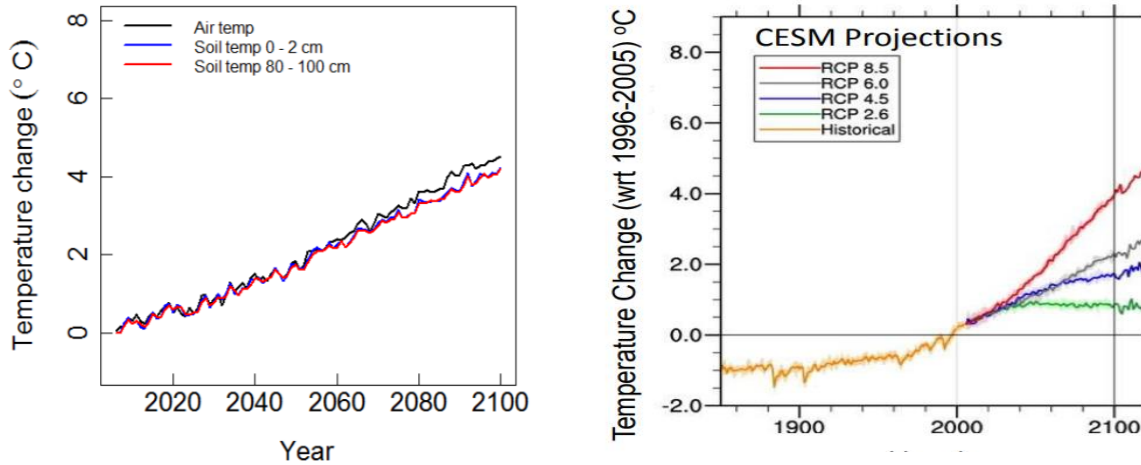


Figure 1.1 RCP 8.5 model predictions for average changes in global air and soil temperature in shallow (0-2cm) and deep (80-100cm) profiles (left). The four IPCC RCP climate model projections for average global air temperature (right).

1.2 GLOBAL SOIL C CYCLE

Soils as a C sink

Carbon is known as the building block of life. Soils are the chief natural system in the terrestrial carbon cycle, holding more carbon than the atmosphere and vegetative biomass combined (Field and Raupach, 2004). As aforementioned, soils are made up of minerals, water, gases and organic matter. Although organic matter makes up the smallest fraction of soil, it is a critical component in its' physical, chemical and biological functioning. SOM is made of dead organic flora and fauna material that is decomposed by soil microbes. Organic matter impacts the structure of soil mitigating erosion, improving water quality and providing nutrients for growing food, timber and other terrestrial resources. Soil organic matter (SOM) is linked to the overall wellbeing of an ecosystem and without SOM there can be widespread ecosystem failures (Ontl and Schulte, 2012).

The amount of SOM in specific soil types is defined by the abiotic, biotic and anthropogenic inputs of the surrounding environment. Some of the abiotic influences on SOM include climate, mineralogy, landscape position and fire occurrence. Biotic factors include amount of accessible organic material, chemical composition, relative allocation of plant inputs and the existing soil food web (Jackson et al., 2017). Anthropogenic factors include land use and historical management strategies. SOM is comprised of compounds with high carbon content, therefore soil organic carbon (SOC) is often related to the amount of organic matter in the soil (Ontl and Schulte, 2012). It is important to understand how carbon is inputted into the soil to understand this relationship.

SOC enters the soil via several pathways. First, photosynthesis converts light and CO₂ into energy for plants by the leaves. This C is then transferred underground by the roots as photosynthates, which then are metabolized by the microbes within the soil. Carbon is also added directly by dead root biomass. Other sources of SOC include dead aboveground vegetation and carrion. These biotic sources are quickly decomposed by soil microbes since they provide rich available sources of carbon. The aboveground biomass is closely related to belowground SOC stocks and varying across dissimilar climatic conditions (Figure 2). Understanding how carbon stocks vary across different climate regions can help to accurately predict how soils may react the abrupt and sometimes irreversible changes of climate change.

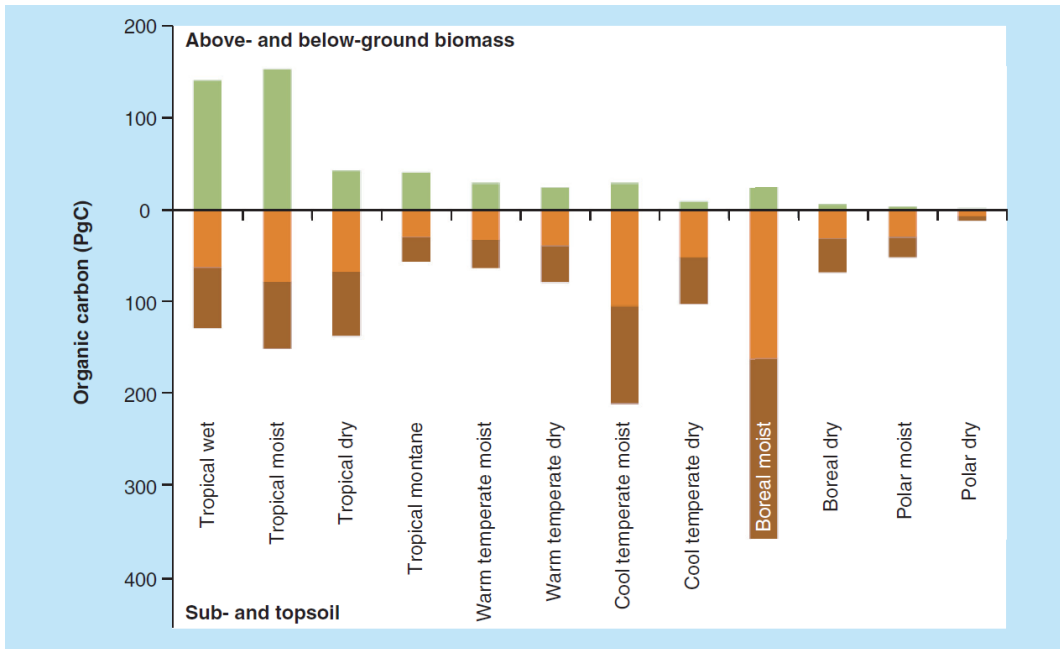


Figure 1.2 Aboveground biomass (green) and belowground SOC stocks in topsoil (orange) and subsoil (brown) by IPCC climate regions (Scharlemann et al. 2014).

Soils input of C into atmosphere and SOM decomposition

Quantifying accurate global SOC stocks has proven to be a difficult task. Many studies have tried to quantify global SOC stocks since some of the first estimates in 1951, but due to the complex nature of the system there is always heavy uncertainty. The most recent estimates of global SOC stocks estimate 1500Pg of C existing within the soil (Scharlemann et al., 2014). However, this soil carbon is not stationary and is constantly cycling through the carbon cycle. SOC specifically changes rapidly with land use change. Historically, SOC stocks were dramatically altered through land use change, like unsustainable forestry and poor agricultural practices (Jackson et al., 2017). In the tropics alone there is a net loss of $1.6 \pm 0.8 \text{ Pg C y}^{-1}$ from the soil arising from the lack of sustainable management strategies like no till, and selective logging (Smith, 2008). When vegetation is removed from a landscape and soil is overturned, SOC that was

once protected is exposed at the soil surface and vulnerable to oxidation. Further understanding of the mechanisms driving carbon turnover is needed to mitigate CO₂ from land use change.

When looking to mitigate atmospheric CO₂, understanding the intrinsic mechanisms driving the soil carbon cycle is critical. Soil microbes are the greatest players in cycling SOC from the soil to the atmosphere. Microbes metabolize and respire C resulting in atmospheric CO₂. 60Gt of C is released annually via respiration by soil microbes which is seven times the annual emissions from fossil fuels (Solomon et al., 2007). Soil microbes consist of many species of bacteria, fungi, protozoa, ameboma, nematodes, earthworms, and arthropods all playing a different role in C cycling. These organisms aid in the productivity of the soil through nutrient acquisition, nitrogen (N) cycling, C cycling and soil formation. Within the C cycle, bacteria and fungi host up to 100% of the decomposition services (van der Heijden et al., 2006). The massive role that soil microbes play in the C cycle make them a vulnerable group to changes through global temperature rise.

Modeling soil respiration with rising temperature

One of the anticipated consequences of rising global air temperatures is augmented soil warming. A study by Pietikainen et al. (2005) observed soil respiration rates in bacteria and fungi communities across a 40°C temperature gradient in agricultural and forest soil. The agricultural soil had a high pH with low organic matter content and the forest soil had a low pH and high organic matter content. The soils were incubated in a laboratory setting at different temperatures ranging from 0°C to 40°C. The study found that “the respiration rate at 45°C was around 120 times higher than at 0 °C in the agricultural soil and 70 times higher in the humus soil” (Pietikainen et al., 2005). The results of this study translate to higher soil temperatures mean higher soil respiration rates. Like this study, many studies now are observing how temporal changes affect soil respiration

rates. Unique soil characteristics exist in a broad range of climates making datasets on soil respiration important for validating global models on the pressures of climate change on SOC stocks.

Current models predicting soil respiration follow either a linear, exponential or Arrhenius relationship with rise in temperature. Linear and exponential models fail to present an unbiased estimate of respiration rate. There is high variability within these models which underestimate respiration at lower temperatures while overestimating respiration at higher temperatures (Lloyd and Taylor, 1994). The best model in predicting soil respiration over temperature changes is an Arrhenius type equation. The Arrhenius equation was originally developed for enzyme kinetics but is now widely used for temperature relationships. It is less biased than other models because at high temperatures the rate of reaction levels off. Rates of soil respiration leveling off at higher temperatures is consistent with the literature and therefore is a more accurate representation of these system. Another way of predicting respiration rate changes is using the Q10 value. Q10 is the rate of change in a system with an increase in temperature by 10°C. It is used to measure the temperature sensitivity of the rates of metabolic enzyme activity in microbes. The typical enzymatic Q10 reaction is around 2, meaning the rate of metabolic enzyme activity doubles with an increase of temperature by 10°C. The rate of Q10 varies within different ecosystems based off existing SOC stocks and soil moisture (Meyer et al., 2018)

Soil respiration over depth in temperate and arctic systems

Many soil respiration studies have focused on arctic systems. Arctic systems are high priority for SOC stock modeling because of immense vulnerability of C existing in permafrost. With rapid warming, permafrost soils have incredible potential to release immense amount of C to

the atmosphere. A study by Bekku et al. (2003), compared the rates of soil respiration of arctic, temperate and tropical soils across several temperature gradients. Temperate soils had lower temperature dependence than arctic and tropical soils which showed higher rates of temperature dependence at higher temperatures (Figure 3). This study displays how soil respiration rates change with climatic zones, even if they experience the same degree of warming. The inherent properties of the soil within each diverse climatic zone make each relationship with soil warming and respiration rates unique. These results further emphasize the need for soil warming experiments to take place in the understudied tropical environments.

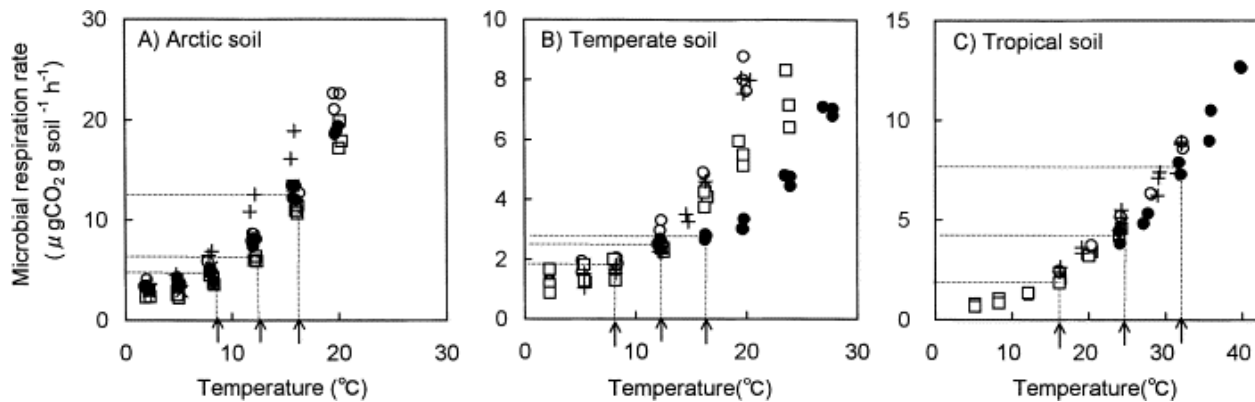


Figure 1.3 Microbial respiration response rate to an increase in temperature across arctic, temperate and tropical soils (Bekku et al., 2003).

Rates of soil respiration need to be addressed by climatic zone and most critically, depth. Older C tends to be deeper within the soil profile and the effects of deep soil warming are widely understudied. A study by Pries et al. (2017) observed rates of deep soil respiration within a temperate forest. The soil temperature was heated to 4°C above ambient temperatures to mimic the effects predicted by the IPCC RCP 8.5 business as usual model for 2100 (Pries et al., 2017). Earlier soil warming studies failed to look at the entire soil profile by focusing on shallow soils

(up to 15-20cm). Pries et al. (2017) reported one of the first deep soil warming studies by observing soil respiration at depths up to 100cm. The inclusion of the deep soil profile revealed annual soil respiration rates increased by 3% with the 4°C warming (Pries et al., 2017). This 3% increase is an immense amount when considering the net CO₂ soils release into the atmosphere annually. This study further addresses the need for “whole soil” warming experiments.

1.3 SOIL MICROBIAL COMMUNITIES

Impact of warming on microbial abundance

Determining the effect of deep soil warming has on atmospheric CO₂ involves focusing on the microbes responsible for this respiration. It has been found that as the soil warms microbial abundance increases up to a certain threshold. Pietikainen et al. (2005) found that with soil warming, bacterial abundance was fourteen times greater in an agricultural soil (low OM) and nine times greater in the forest humus soil (high OM) than without warming. Bacterial abundance plateaued around 45°C suggesting a threshold of warming that decouples the relationship between soil temperature and respiration. Optimum temperatures for fungal growth were 25 to 30°C. Beyond 30°C, there was a dramatic decrease in fungal abundance suggesting that at higher temperatures there is an alteration in the balance of these two groups of organisms. Bacteria may have higher abundance as temperature increases while fungal abundance may decrease. This study looked at the instantaneous changes in the fungal and bacterial communities with warming, rather than long-term changes. There may be different results in species composition of bacteria and fungi with the long-term changes climate change will bring.

Microbial community structure and the effects of a pH gradient

Another large effect on soil microbial community structure is soil pH. On a global scale, soil pH influences soil bacterial communities stronger than fungal communities. Generally bacterial diversity and community structure has a strong positive relationship with soil pH, while fungal diversity and community structure is uncorrelated or weakly correlated with soil pH (Rousk et al., 2010). The Rothamsted Research station in Harpenden, UK is a long-term experiment examining the effects of a gradient of pH from 4.5 to 8.3 on soil microbial communities. Rousk et al (2009) found that at this site, bacterial growth was highest at the more basic end of the pH gradient and declined by a factor of 5 towards acidic pH values. Fungal growth was highest in the more acidic environments and declined by a factor of 5 as pH became more basic (Rousk et al., 2009). Rousk et al (2009) also found that basal soil respiration rates decreased by 30% from a pH of 8.3 towards the more acidic pH of 4.5. pH itself can be a measure of predicting the structure of microbial communities, however the “spillover” or indirect effects of a change in soil pH remain unknown, especially in tropical soils. Beyond effecting microbial community structure, pH effects the solubility of different elements, nutrient availability, biogeochemical cycles, CO₂ flux, and the flux of other greenhouse gases (CH₄ and N₂O) (Lammel et al., 2015). Therefore, the effects of pH are wide ranging and call for more empirical data across different soil types to predict how soil properties effect microbial communities and consequently rates of soil respiration.

1.4 INTERNATIONAL SOIL EXPERIMENTAL NETWORK (ISEN)

Call for global soil C experiment network

Several efforts are underway to quantify the effects of soil warming on global soil carbon. The proposed International Soil Experimental Network (iSEN) is expanding the database efforts for deep soil warming experiments. This network calls for replicated deep soil warming

experiments across different climatic zones to predict how SOC stocks may be affected by soil warming. The network seeks input from individual scientists, science administrators, land managers, students, institutions and the public to expand its database, providing resources for database users to assure the quality and homogeneity of the data. The iSEN network works like a business franchise providing “recipes” or protocols with individual lab principal investigators providing their own funding. This design allows for global synthesis deep profile soil experiments while minimizing costs (Torn et al., 2015). By globalizing soil carbon studies, projections can be determined for the effects of climate change on different soil types around the globe. Along with this, gaps in the database efforts can be identified.

Lack of tropical soils in network

Existing soil carbon experiments are lacking in tropical climates. iSEN reports most of its long-term carbon experiments in arctic and temperate zones. Arctic climates, as aforementioned, are a large focus of SOC studies because of the melting of permafrost which can release large amounts of carbon. Most temperate climate studies, within the iSEN network, are affiliated with public institutions and universities that are in temperate climates. Tropical systems are scarce in comparison to these two ecoregions. Tropical systems, especially those on islands, are extremely vulnerable to climate change and should be integrated into the iSEN.

Along with a gradient in climates, it is important to have a gradient of soil types integrated into the iSEN. Global soil types vary in physical, chemical and biological characteristics. The highest level of taxonomy of soils recognized by the U.S. Department of Agriculture (USDA) is the National Resource Conservation Service (NRCS) Soil taxonomy classification of the twelve main soil orders. These twelve soil orders are distinguished by dominant physical, chemical and

biological properties. It is these different soils that provide many of the key nutrient cycles relied on for Earth's crucial ecosystem processes. One of these soil orders, Andisols, hold vast amounts of carbon compared to other soil orders. Andisol deep soil experiments are lacking in the iSEN. This gap in the iSEN database data identifies the critical need for tropical Andisols deep soil experiments.

1.5 IMPORTANCE OF TROPICAL SOILS: HAWAIIAN ANDISOLS

Andisol global distribution and intrinsic C stabilization properties

Andisols are volcanic ash-derived soil, found mostly in the Pacific “Ring of Fire” region. They cover more than 120 million hectares worldwide spanning a diversity of climate and soil types (Dahlgren et al., 2004). Andisols can be found in tropical regions such as, Central and South America, Indonesia, and Hawaii. They are a volcanic soil order, found in less than 1% of the world yet, hold 5% of the worlds C (Matus et al., 2014) . There are several properties in the mineralogy of Andisols that make them a key aspect of C sequestration. SOC is transformed by bacterial activity and stabilized into organo-mineral complexes that have been found to be abundant in andic soils (Matus et al, 2004; Torn et al, 1997; Post and Kwon, 2000). The organo-mineral complexes are governed by poorly and non-crystalline structure minerals (Crow et al., 2015) The poorly and non-crystalline structure has higher surface area for sorption of organic C than crystalline structures.

These poorly and non-crystalline mineral particles are found across the Hawaiian Islands from volcanic origins. Volcanic ejecta from Hawaiian volcanoes is comprised of lava and tephra. Through the early weathering stages, there is a rapid dissolution of Si, Fe, Al and non-hydrolyzing cations (ie. Ca and Mg). This is due to the higher mass concentrations of volcanic glass in Andisol parent material compared to other igneous rock parent material types (Lowe, 1986; Gislason et al.,

1996). Through the intermediate stages of weathering, the non-hydrolyzing cations are leached from the soil retaining Si, Fe and Al ions which then precipitate into poorly and non-crystalline solid phases (Chadwick et al., 2003). This is especially true in humid tropical climates, where heavy annual precipitation promotes advanced leaching of the non-hydrolyzed cations. The late stages of Andisol weathering transforms these poorly and non-crystalline minerals into crystalline minerals like kaolinite and gibbsite (Chadwick and Chorover, 2001).

The relationship between temperature history and weathering time follows the Arrhenius relationship. The degree of weathering is less likely influenced by time, but more so by climatic factors, like temperature (Hodder et al., 1996). This relationship further demonstrates the need for advancing the knowledge of how tropical soils will react to climate changes. The area of focus for Andisol SOM storage potential is the intermediate weathering stage, due to the concentration of organo-mineral high surface area and charge. If this stage is rapidly lost due to changing climates, then the carbon stabilization properties of andic secondary minerals could be overwhelmed and accelerate to late stage crystalline mineral phase that have much less C stabilization potential.

The intermediate stage of Andisols involves high concentrations of Fe and Al organo-mineral particles, which have a strong affinity to C. Organic matter complexes with Fe and Al oxides as mechanism for OM stabilization forming aggregates protected from microbial degradation. (Hernández-Soriano, 2012). The C ratio with poorly and non-crystalline minerals increases with depth (Matus et al., 2014). This stabilization of C by mineral complexation is heightened by the fact that, deep subsoil C is better protected from decomposition than topsoil C, making Andisols a robust C stabilizer soil at depth. However, it is noted that detailed knowledge is lacking in organic matter composition and degradation at depth in Andisols (Matus et al., 2014). This poses the question; how will different compositions of organic matter be affected by microbial

groups across the entire depth of the soil? The accessibility of the SOM to different functional groups of microbes, existing at depth, is the key to understanding how soil respiration rates may be affected. Furthermore, Andisols have high contributions in alkyl C that is resistant to chemical oxidation and increases their C storage, because SOC is less likely to react to oxygen to create atmospheric CO₂ (Rivas et al., 2012). With these stabilization properties in Andisols it was found that SOC stock and turnover did not vary across a 5°C mean annual temperature (MAT) gradient in a tropical montane forest system (Giardina et al. 2014). It should be noted that the MAT gradient is not representative of the intensive warming over a short time period that may result from climate change. Therefore, the stability of the carbon sequestration properties under the pressures of climate change are still unknown.

Andisols and physicochemical mechanisms for soil carbon stabilization and destabilization

The mechanisms driving SOM stabilization and destabilization in Andisols vary dependent on physical and chemical factors. It is unknown why some soil organic matter is destabilized and decomposed readily while other SOM lasts stabilized for eras (Schmidt et al., 2011) . Rather than the old view of humus (SOM rich particles) as the main stage of organic matter, Lehman and Kleber present SOM as a continuum for which organic matter is constantly being degraded. The traditional view sees SOM as stable humus that is makes up SOC stocks; the emergent view focuses on the flow of carbon through microbial access and degradation rather than seeing SOM as a single stock of carbon (Lehmann and Kleber, 2015).

Like the Lehmann and Kleber soil continuum model (SCM) for the fate of organic matter, Harden et al. 2017 takes the same approach for processes controlling SOC pools (de)stabilization. These mechanisms span more than the three categories (physical, chemical, biological) in terms

of the driving mechanisms for stabilization. Both papers lean towards modifying the old view of separating soil carbon processes and ecosystems and looking at them across continuums. This point further illustrates the need for soil carbon networks that span spatial and temporal gradients to determine SOC pools and their (de)stabilization mechanisms (ISCN and ISEN). Shifting towards understanding gradients rather than independent categories seems to be the future of soil carbon science. Schmidt et al. (2011) emphasizes this point of researching the deep soil C gradient. Little is understood about deep soil C, even though it contributes to half the world's C stocks (Schmidt et al., 2011). Consistent with literature about Andisols, reactive mineral surfaces make C less accessible to microbes especially at depth. It also has been found that microbial biomass decreases with depth. The uncertainties that exist in the relationships of SOM across depth especially in the aggregates of mineral components of Andisols, leaves much to be studied.

These Al and Fe mineral components are hard to detect by X-Ray Diffraction (XRD) machine since they are non-crystalline and therefore are inferred. The Al and Fe content of minerals are determined widely using oxyhydroxides (or hydroxylamine), sodium pyrophosphate and citrate dithionite extractions. Silica (Si) is also used to determine the amount of Al and Fe minerals in the soil since these minerals are weathered from the clay particles of silica solids and can be determined by the same three extraction method (Parfitt, 2009) .The Al:Si molar ratio in the soil varies dependent on whether the soil is silica rich or aluminum rich. The aluminum rich mineral component of Andisols is derived from the leaching of Si from clay particles during Andisol formation. There is a positive relationship between the oxalate-extractable Si and the total Al content in the soil. The Al remains *in situ* while the Si is leached out (Nanzyo, 2002). Various kinds of soils can be formed from volcanic ash depending on the individual set of soil forming factors at different sites. Among these soils, Andisols or Andosols show unique properties mostly

due to abundant non-crystalline materials such as allophane, imogolite, Al-humus complexes, ferrihydrite and so on. Highly porous structures made of aggregated non-crystalline Andisol materials have a light and fluffy nature, accommodating large amounts of both plant-available and hygroscopic water. They show many other unique physical properties different from other soils. Moreover, Andisols have unique chemical properties, including aluminum-rich elemental composition, large amount of humus accumulation in A horizons, variable charge characteristics, high phosphate retention capacity, high affinity for multi-valent cations, high KCl-extractable and water-soluble Al in non-allophanic Andisols at an acidic to weakly acidic pH range, and so on. Finally, topics related to biological activity in volcanic ash soils are discussed regarding P supply from apatite and K supply from biotite for crops in fresh volcanic ash, effects of KCl-extractable and water-soluble Al on soil-borne diseases, adsorption characteristics of viruses on Andisols and P tropistic root growth of Brassica plants in P-deficient Andisols (Nanzyo, 2002) . Secondary minerals within the tephra deposits can host a Al:Si molar ratio of ~1.0 to ~2.0. Minerals with an Al:Si ratio of ~2.0 are categorized as “proto-imogolite” allophones because of the hollow tubular structure lending itself to the imogolite particle shape (Parfitt, 2009) . Therefore, Si is an important indicator of Al in the soil. Overall, there are many inherent properties of Andisols that make them hold strong potential for C stabilization if managed correctly.

Andisols in Hawaii (land use)

Andisols in Hawaii are not being used to their greatest potential. The inherent properties of Andisols that make them have a strong affinity to C are jeopardized by land use changes and poor land management. 39% of Hawaii’s land area is classified as Andisols falling under varying land use conditions (Torn et al., 1997). These land usages can exist from cropland, pasture, forest,

conservation land and urban. When these soils are poorly managed, they can lose the structure that makes them effective at stabilizing carbon at higher rates than other soil orders. Poor management includes clear cutting, poor tillage and lack of erosional controls. It is crucial to conserve these soils through proper management techniques so that the inherent soil properties can be preserved as a potential C sinks as climate change intensifies. Determining the inherent mechanisms driving SOC stabilization in Hawaiian Andisols will inform management decisions so these mechanisms can be preserved.

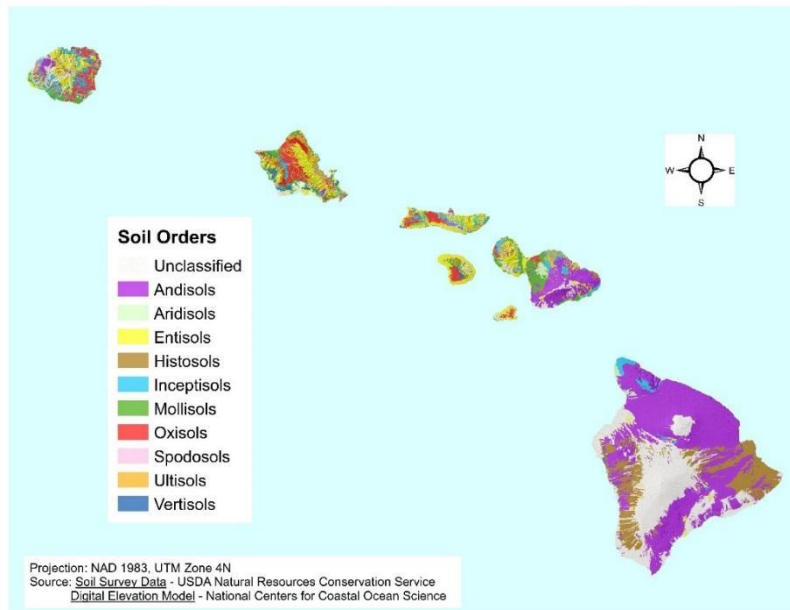


Figure 1.4 Distribution of the 10 soil orders found in the Hawaiian archipelago (Andisols are in purple Hawaii Soil Atlas, 2018).

CHAPTER 2 : SEASONALITY OF SURFICIAL SOIL CARBON FLUX ON A TROPICAL
HAWAIIAN ANDISOL



Figure 2.1 Sampling the collars via the GRACENet protocol upslope in the fieldsite at the Lyon Arboretum in September 2017

2.1 INTRODUCTION

The seasonal fluctuations of surficial soil carbon are an important component to understanding the global carbon cycle. The near surface of the soil profile (<30cm) holds vast amounts of carbon that are vulnerable to climate and land use changes (Smith, 2008). Because of the small magnitude of seasonal temperature fluctuations near the equator, tropical systems experience different seasonality effects on soil respiration than systems in higher latitudes. The relationship of seasonality and carbon flux in the upper Northern hemisphere is well documented, especially in the vulnerable peatlands, but the effects of seasonality in high carbon environments like tropical forests is poorly understood. In climates like peatlands of colder temperature regimes, soil respiration is relatively more sensitive to temperature, but more information is needed within all climate types to understand how soil carbon pools may react to future changing temperatures (Lloyd and Taylor, 1994). Focusing on the seasonality of surficial CO₂ fluxes in understudied tropical forests is a critical proponent to the future of climate change models given the large potential reservoirs of carbon that lay vulnerable to rising temperatures.

The lack of seasons in the equatorial tropical region is related to the small change in solar radiation throughout the year. Unlike the upper latitudes which receive a wider range of solar angles lending to the presence of wider temperature ranges, the tropics receive a smaller range of solar angles resulting in very little temperature fluctuations throughout the year. This isothermic temperature regime results in less dramatic seasonal changes causing less effect on ecological processes: however, the tropics do experience seasonal changes of soil moisture. In a tropical forest in Thailand it was found that soil respiration was mostly influenced by soil moisture rather than by soil temperatures (Hashimoto et al., 2004). Well drained soils however are less affected by changes in precipitation than poorly drained soils (Davidson et al., 1998). This means that in

tropical soils the precipitation regime can be more important than the temperature regime, however soil properties like drainage are also critical to understand the changes in the rate of soil respiration.

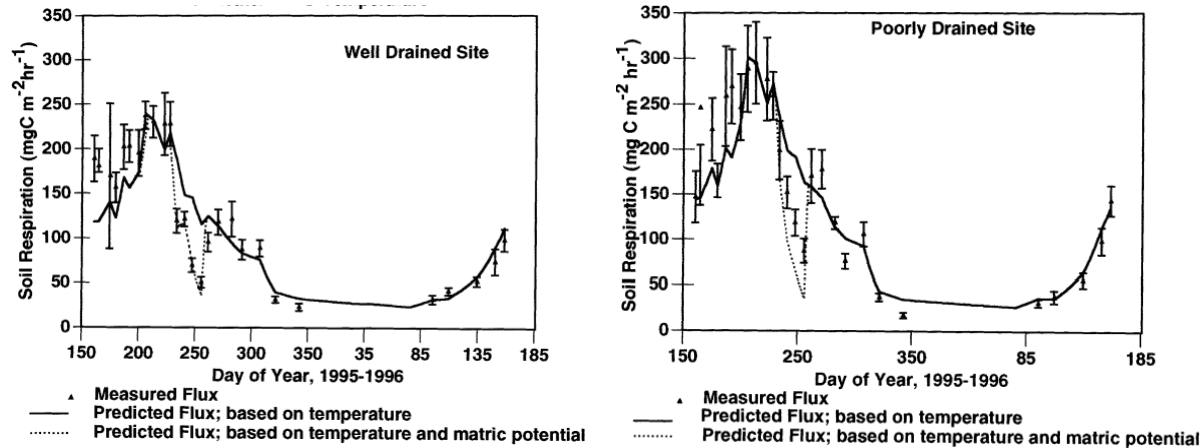


Figure 2.2 Seasonal variation in soil respiration as predicted by soil temperature and soil moisture for a well-drained soil (left) and a poorly drained soil (right) in a temperate forest from the Davidson et al. study (1998).

By understanding the drivers of soil respiration seasonality within tropical soils climate models can inform predictions on how the soil carbon cycle may change with a changing climate. By looking at micro changes across an annual cycle, the macro changes that may come in the next decades with changes in precipitation and soil temperature can be better understood. A Hawaiian tropical Andisol presents an ideal study soil to look at seasonal soil respiration cycles given its isothermal temperature regime, but varied precipitation regime and unique soil properties.

2.2 OBJECTIVES AND HYPOTHESES

The objectives are outlined below along with the corresponding hypothesis, broken down into a prediction, justification, and approach.

2.2.1 Objective

The objective of this study is to determine if a seasonality effect exists on surficial carbon storage in a tropical Hawaiian Andisol.

2.2.2 Hypothesis

Given the small annual temperature fluctuation for the study site, if the Arrhenius relationship between temperature and surficial CO₂ flux is true across latitudes, then there will be little to no seasonality effect on surficial soil carbon on a Hawaiian tropical soil.

2.2.3 Prediction

Because the isothermic temperature regime at the study site there will be little to no effect of annual changes in temperature on the surficial soil carbon flux.

2.2.4 Justification

Linkages between soil respiration and rising temperature suggest that increased soil temperature escalates microbial activity in the soil and consequently soil respiration rates (Fang and Moncrieff, 2001). Given the isothermic temperature regime there will not be a seasonal effect on soil respiration as measured by CO₂ flux. Given the well-drained properties of the study soil, it

is unlikely that seasonal changes in precipitations will significantly affect soil moisture to increases soil respiration.

2.2.5 Approach

The approach to determining the seasonality effect was biweekly sampling of surficial soil carbon flux using a static chamber network. The CO₂ flux was interpolated into heatmaps by kriging to visually assess for changes in CO₂ flux biweekly. To assess seasonality further, tests for autocorrelation between sampling dates were applied to determine if a lag effect exists.

2.3 METHODS

2.3.1 Site Selection and Description

The fieldsite is located at the Lyon Arboretum, Honolulu, HI (21.3330° N, 157.8015° W).

The Lyon Arboretum is 78.3 hectares with an elevation range of 137-564m above sea level. The average annual temperature is 25.6° C with an annual temperature range of 11.1 to 32.2° C. The Lyon Arboretum receives an average of about 4190 mm of rainfall annually at the experimental field site. Over a century ago, the Lyon Arboretum was rangeland for cattle. Today the Lyon Arboretum has been cultivated back into a haven for tropical plants from around the world, with an emphasis on plants native to the Pacific Islands/Asian region. This landscape provides a unique habitat for research, outreach and education, regarding the study of diverse Hawaiian ecosystems.



Figure 2.3 Location of the fieldsite on the island of Oahu at the Lyon Arboretum, Honolulu, HI

The fieldsite itself is located behind the visitor's center building at the Lyon Arboretum. This location provides the benefit of convenient access to electricity, which is required for this manipulative warming experiment. The initial ground cover of the site was completed cleared in preparation of the experiment. Manual clear cutting occurred in June of 2017 of the understory vegetative cover consisting mostly of the invasive *Hedychium flavescens*. Some low vegetative ground cover was kept mitigating soil erosion on the site. The topography of the fieldsite is an 18% slope, determined by a topographic survey in August 2017. The fieldsite was weeded weekly to eliminate the establishment of deep roots which can influence the overall carbon flux in the soil.



Figure 2.4 Site development shown before clearing (left) and after clearing (right).

The fieldsite soil is classified as an Andisol by the Web Soil Survey (NCRS). This selected hillslope consisted of soil that had not been disturbed in over twenty years. This specific Andisol is part of the Tantalus soil series described in the Hawaii Soil Atlas. The Hawaii Soil Atlas describes the series as “medial over pumiceous or cindery, ferrihydritic, isothermic Typic Hapludands” The pH at the field site ranges from 5.0 to 6.6. The surficial CO₂ seasonality field study was conducted for one year, from September 2017 to September 2018.

2.3.2 Field Methods

Static chamber network and gas well CO₂ flux gradient method

A static chamber network was established across the fieldsite following the GRACEnet Chamber-Based Trace Gas Flux Measurement protocol to understand fluxes in surficial soil respiration. Surficial soil respiration was measured from ‘collars’ which are two-piece static polyvinyl chloride (PVC) plastic chambers with 10cm diameter and 30cm in height that were vertically installed into the soil 20cm down with 10cm above the soil surface. PVC heads were placed on the chamber lip edge with a top septum installed for gas sampling. When not sampling, the PVC heads were removed from the chamber lip to avoid development of anaerobic respiration. There was a total of 64 collars within the network established in a grid network 2m apart from each other (*Figure 2.5 Contour map of Lyon Arboretum fieldsite with the placement of the 64 collars (black dots, elevation is in meters, as shown in the colored contours)Figure 2.5*).

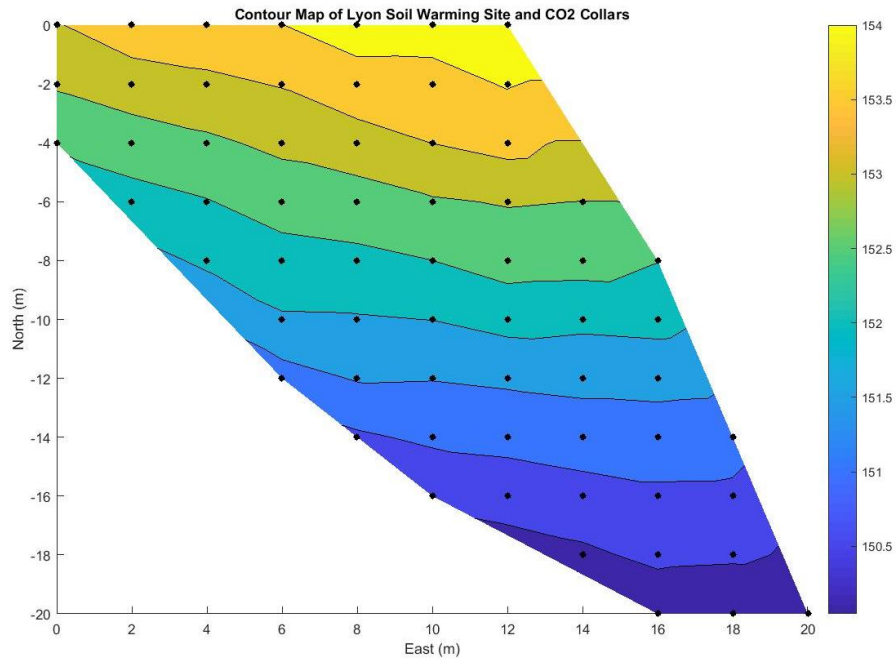


Figure 2.5 Contour map of Lyon Arboretum fieldsite with the placement of the 64 collars (black dots, elevation is in meters, as shown in the colored contours).

Collar gas sampling from the headspace took place biweekly starting in September 2017 until September 2018, allowing for a full year of sampling. Some collars had standing water during the routine sampling time and were omitted from the sampling scheme for those days and the missing values were interpolated. The collars were sampled with a 10ml syringe every 15 minutes for 60 minutes, creating five sampling time points. 5ml of the gas extracted with the syringe was inserted into a 5ml vacuum evacuated exetainer. All gas samples were then run on the Perkin Elmer Clarus 590 GC to determine the concentration of CO₂ in ppm in each sample. The resulting ppm concentrations were then converted into mg CO₂-C m⁻² hr⁻¹. These values were then developed into “heatmaps” in MATLAB which display the flux of CO₂ for each time step.

Preliminary soil pit sampling

Soil pit sampling was completed in November 2017. A 1.3m pit was dug on the down slope of the site to take sample cores along the profile. Starting from the top of the pit a 100g soil sample was taken every 10cm, totaling 14 samples collected overall. These soils samples were then analyzed for moisture content and Fe, Al, Si, C, and N. Moisture content was found by weighing the field moist sample and then placing that sample in a 105°C oven to get the 105°C dry weight. The equation for the moisture content of a single sample is below in Equation 6:

$$\frac{wt_{moist} - wt_{dry}}{wt_{dry}} \quad \text{Equation 2.1}$$

Where wt_{moist} is the field moist weight and wt_{dry} is the dry weight of each sample for the 105°C oven. Fe, Al and Si were measured using three different extraction protocols, including hydroxylamine hydrochloride, citrate dithionite, and sodium pyrophosphate extractions. For the hydroxylamine hydrochloride extraction 0.100g of field moist soil was weighed and added to a 50ml Falcon tube. Then, 25ml of 0.25M hydroxylamine hydrochloride and 0.25M hydrochloric acid was pipetted into each Falcon tube and placed on an end over end shaker for 16 hours. After, the samples were centrifuged at 1500rpm for 20 minutes and filtered through 52 Whatman paper. Samples were stored in the fridge before being shipped for analysis.

For the citrate dithionite extraction, 0.500g of field moist soil was weighed and added to a 50ml Falcon tube. Then 8g of sodium citrate, 0.50g of sodium dithionite and 30ml of deionized water was added to the Falcon tube, which was then capped and shook for 15 seconds and then uncapped to off gas. The Falcon tubes were then capped again and placed on an end over end shaker for 16 hours. Once off the shaker the solution was transferred into 50ml volumetric flasks and 12µl of Power Floc solution was added to each tube and covered with parafilm to shake for

15 seconds. Next the flasks were filled to volume with deionized water and shaken again for 15 seconds. The solution was then transferred back into the 50ml Falcon tubes and the samples were centrifuged at 1800rpm for 30 minutes and filtered through 52 Whatman paper. Samples were stored in the fridge before being shipped for analysis of Fe, Al and Si concentration.

For the sodium pyrophosphate extraction, 0.25g of field moist soil was weighed and added to a 50ml Falcon tube. Then, 25ml of 0.1M sodium pyrophosphate solution was pipetted into each Falcon tube and placed on an end over end shaker for 16 hours. After the samples were centrifuged at 20,000rpm for 15 minutes and filtered through 52 Whatman paper. Samples were stored in the fridge before being shipped for analysis of Fe, Al and Si concentration. Before being shipped all extractions had 15ml of solution added to 15ml Falcon tubes. 75 μ l of Yttrium was added to each 15ml Falcon tube for quality control. Then the samples were shipped to UH Hilo Analytical Laboratory for ICP analysis. C% and N% were analyzed by the Element Analyzer (EA) from 60°C oven dried samples.

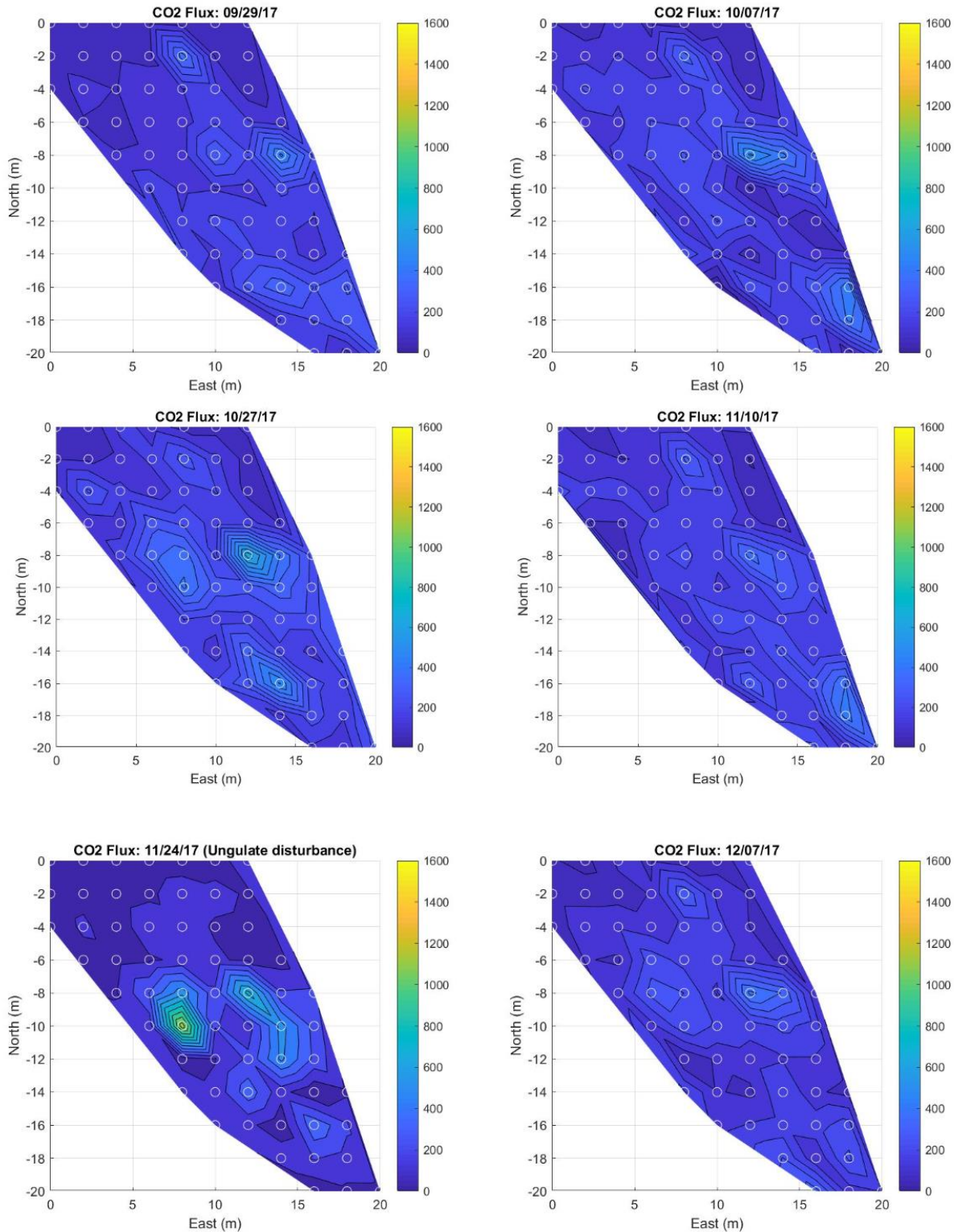


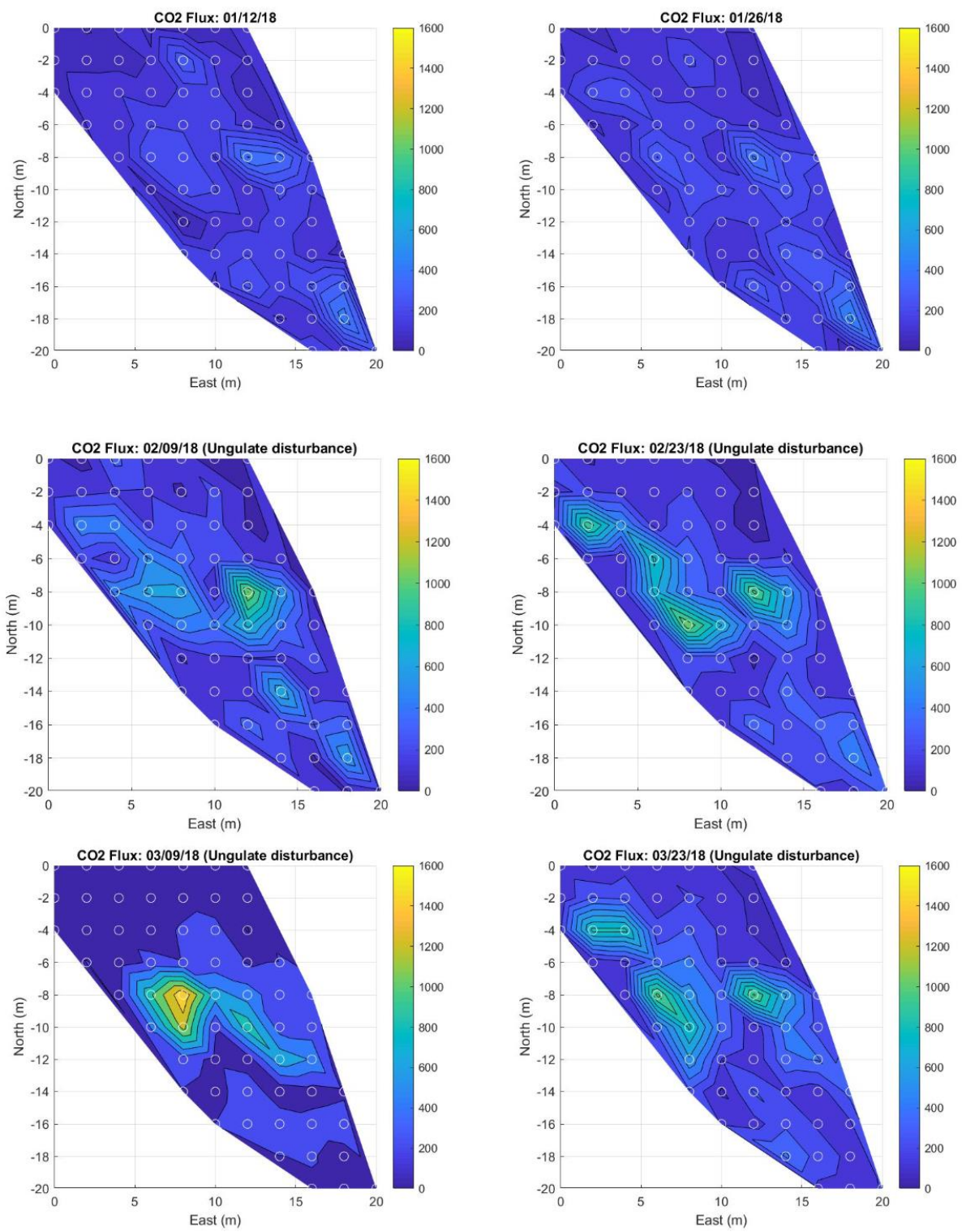
Figure 2.6 Collar for GRACENet protocol being used during sampling (left). 130cm soil pit dug for preliminary characterization (right).

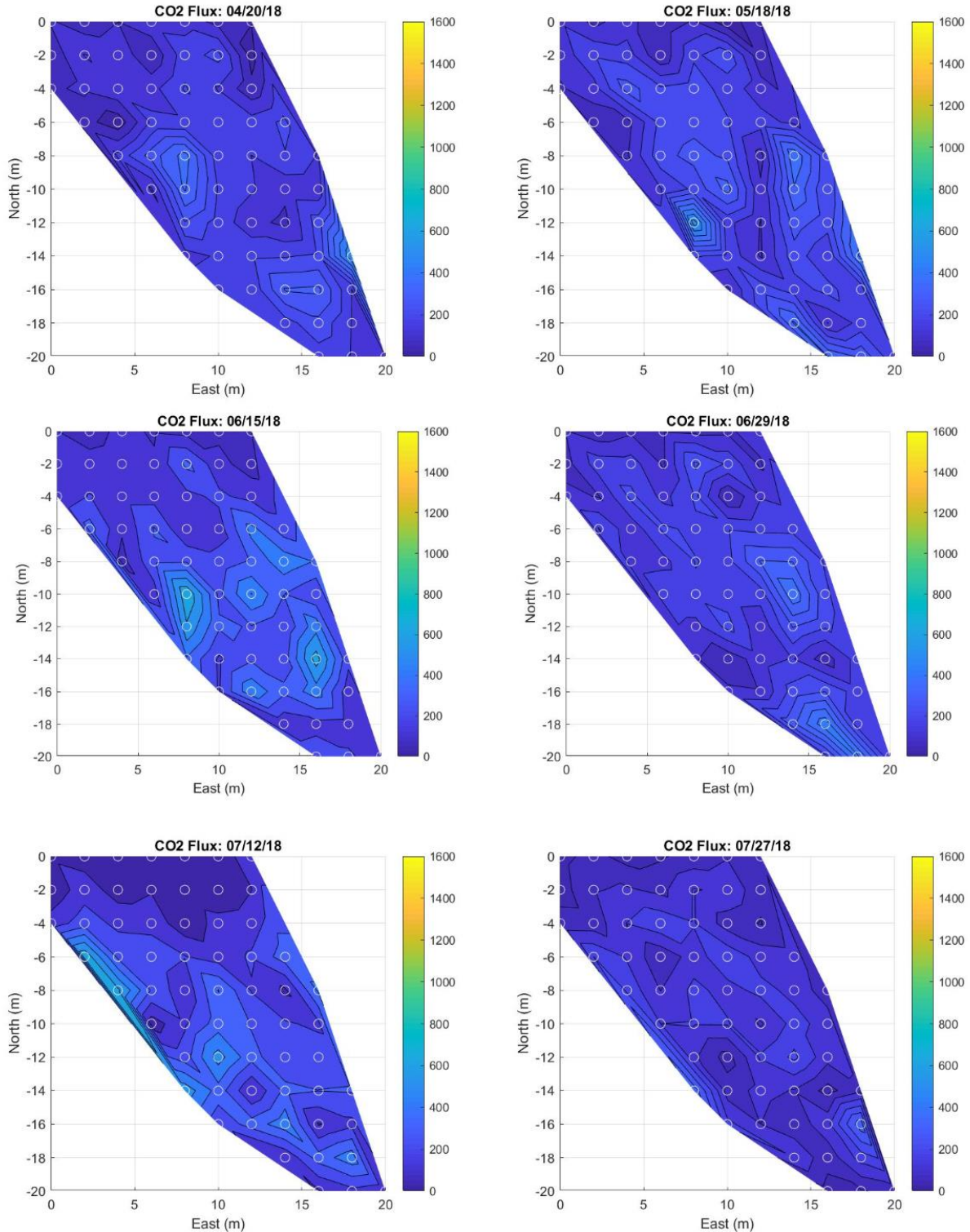
Data Analysis

The analysis of seasonality at the study site is a two-part process. Using the MATLAB contour package biweekly CO₂ flux heatmaps were created using isolines from the data grid. There were two sets of heatmaps created, one with the disturbance effect from ungulates and one without the disturbance effect to display seasonality. To statistically test seasonality an autocorrelation function was used to determine the correlation between near time sampling points (lags). An Augmented Dickey Fuller test to test stationarity was used on the mean CO₂ flux produced for each biweekly sampling. Finally, the raw data seasonal trend was extracted to determine what the effect of seasonality was on the data using a Fourier transformation.

2.4 RESULTS







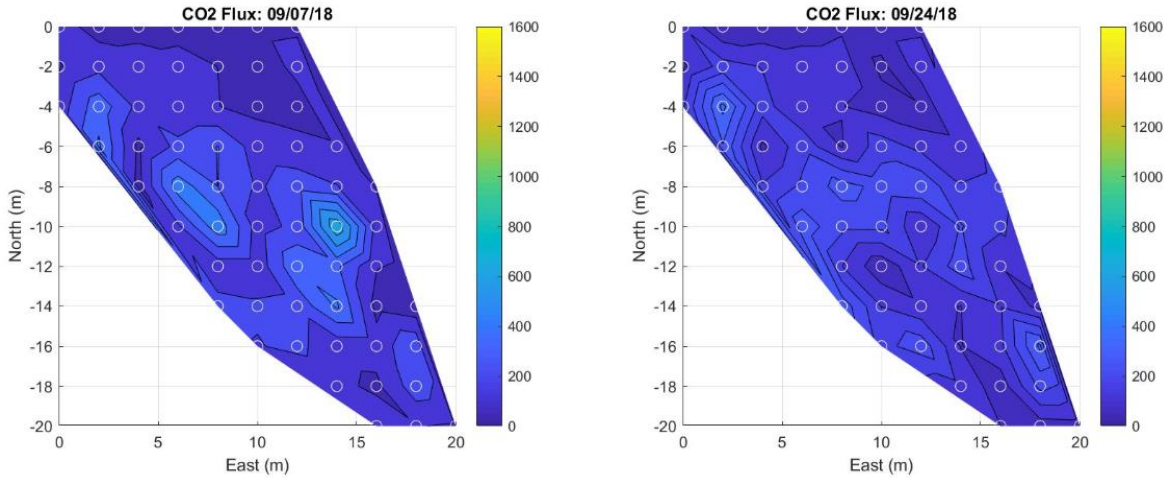


Figure 2.7 Heatmaps of the surficial CO₂ flux ($\mu\text{g CO}_2\text{-C m}^{-2} \text{ hr}^{-1}$) from September 2017 to September 2018 with ungulate disturbance shown by the yellow “hotspots” at the fieldsite in the Lyon Arboretum .

There was little to no change in the surficial carbon flux when including the presence of ungulate disturbance. In late November 2017 and February and March of 2018 there was a disturbance effect created by the grubbing of feral pigs in the center of the fieldsite. This effect is clear in the maps of surficial flux over the time of sampling by the green and yellow “hotspots” on the otherwise blue (color of relative low CO₂ flux) heatmaps (Figure 2.7) . The top panel of Figure 2.9 of the average CO₂ flux from the biweekly sampling shows a large peak around February to March where ungulate activity was the highest. Evidence of the ungulate grubbing in late February can be found in Figure 2.8. Around this time the Lyon Arboretum also reported higher than usual populations of feral pigs on the property.



Figure 2.8 Evidence of ungulate disturbance on February and March 2018 in the center of the fieldsite at the Lyon Arboretum.

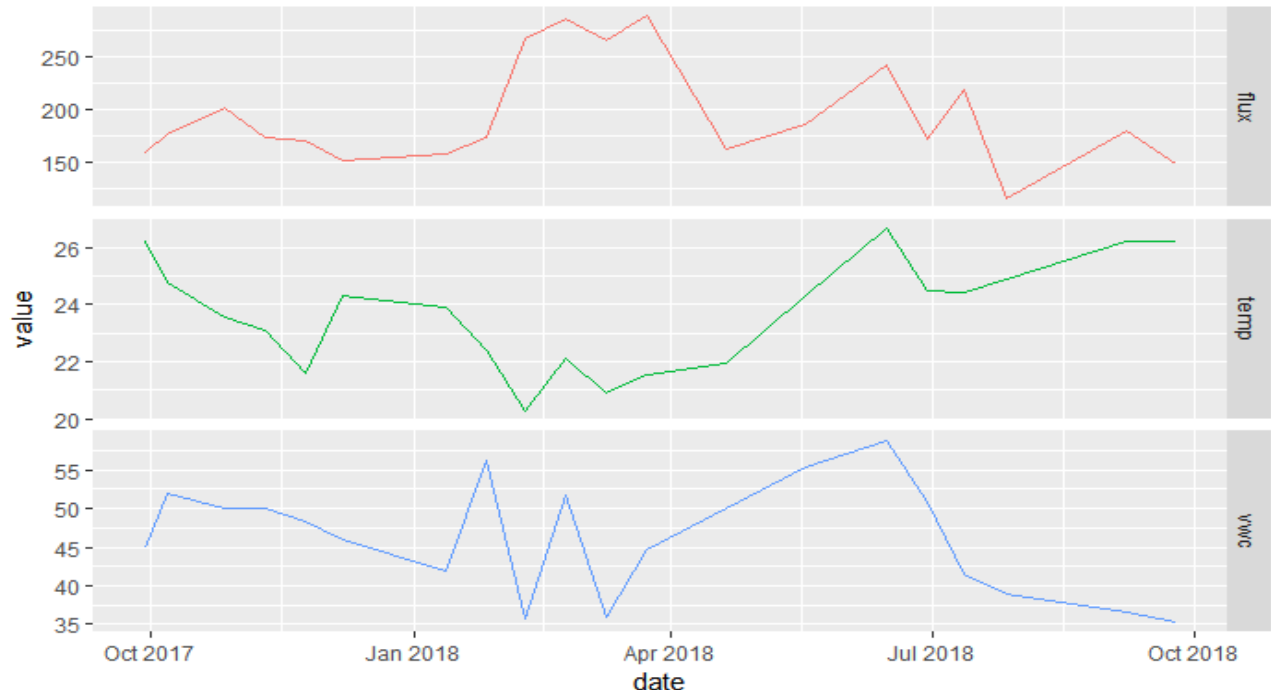
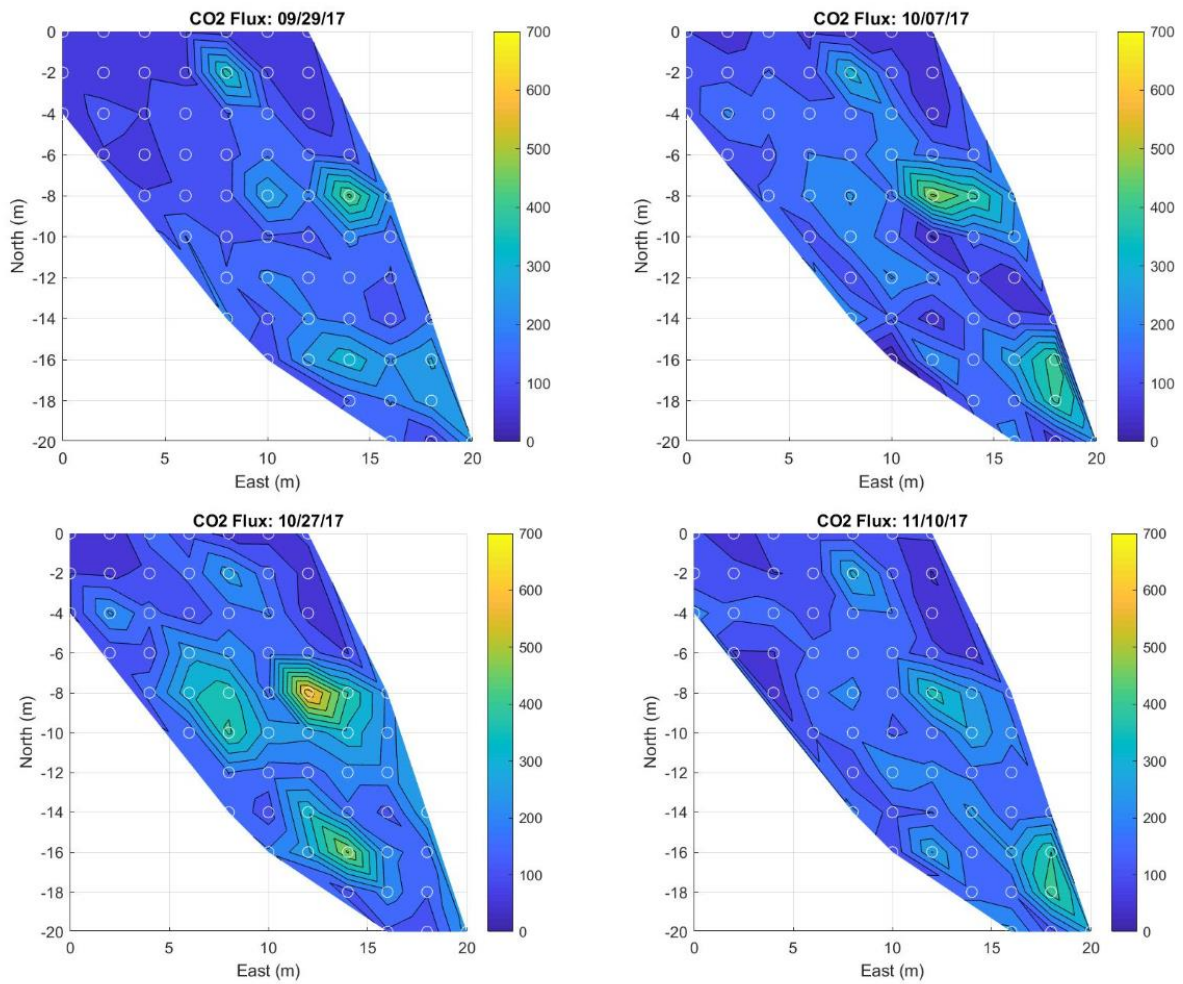
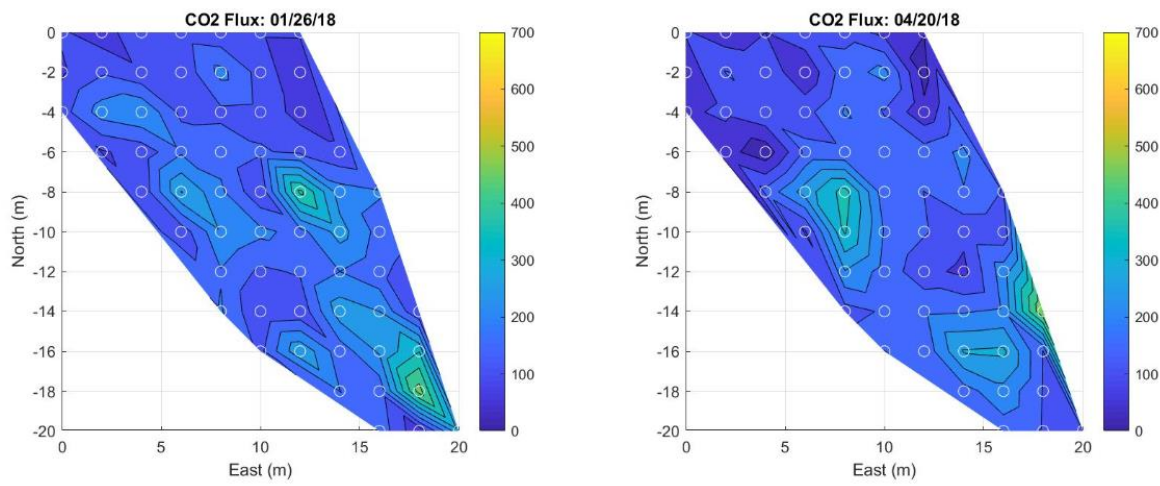
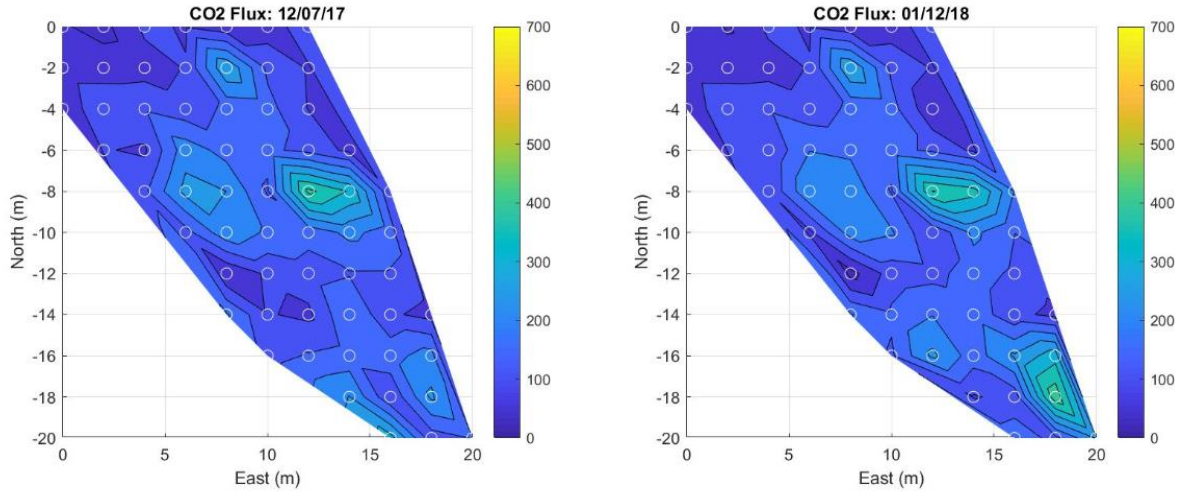


Figure 2.9 The mean flux ($\text{mg C-CO}_2 \text{ m}^{-2} \text{ hr}^{-1}$) (top), soil temperature ($^{\circ}\text{C}$) (middle), and volumetric water content (VWC %) (bottom) of the static chambers from September 2017 to September 2018 at the fieldsite hillslope.





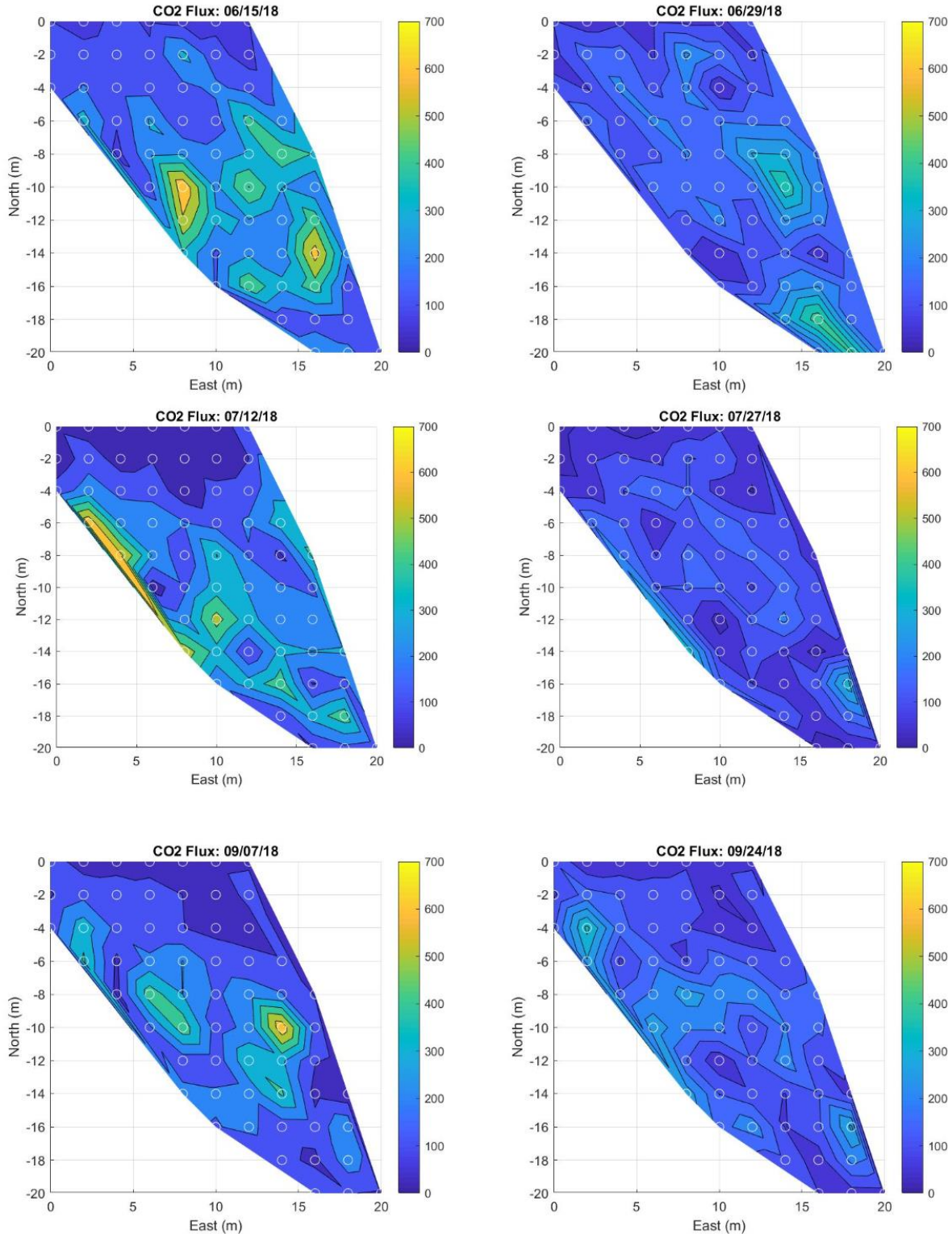


Figure 2.10 Heatmaps of the surficial CO₂ flux ($\mu\text{g CO}_2\text{-C m}^{-2} \text{ hr}^{-1}$) from September 2017 to September 2018 excluding the ungulate disturbance effect at the fieldsite at the Lyon Arboretum.

In Figure 2.10 the ungulate disturbance was removed and there is some visible evidence that suggests seasonality in surficial CO₂ across the seasons. The summer months of June and July shows “hotspots” of CO₂ flux shown by the brighter yellow and green colors as compared to the darker blue colors that dominate the heatmaps. The seasonality effect across mean CO₂ flux is shown in Figure 2.11 by an autocorrelation (ACF) plot. The spikes between lags that are above or below the blue dashed lines show evidence of autocorrelation among the data. To test this trend further an Augmented Dickey Fuller (ADF) test was used to test stationary or lack of a seasonal component to the data. The ADF test produced a p-value > 0.05 (P= 0.91), which supports the null hypothesis that the data is nonstationary and contains a seasonal component.

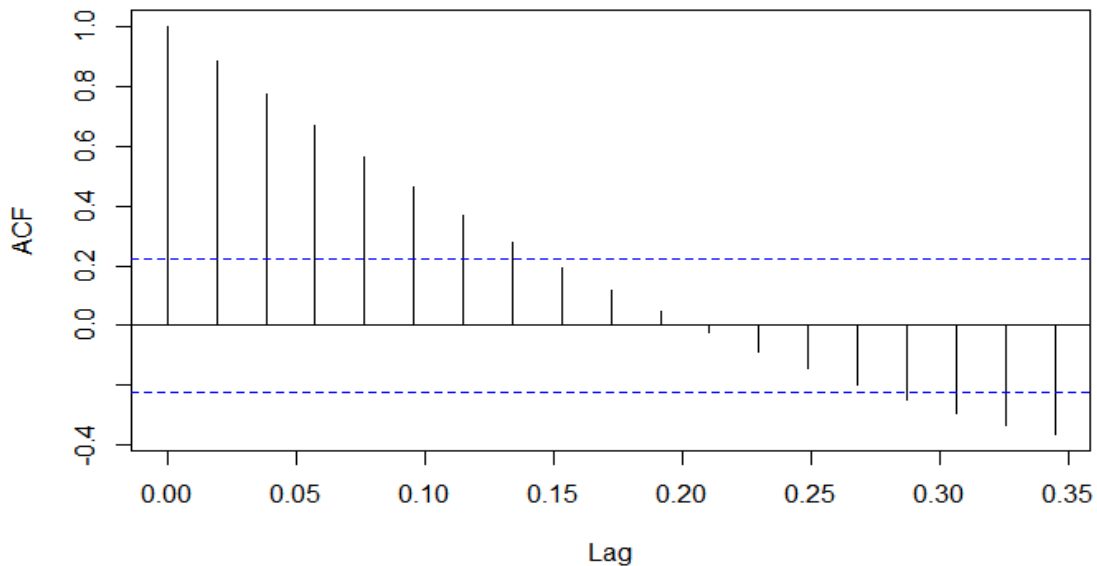


Figure 2.11 ACF plot of the mean flux of CO₂ timeseries from September 2017 to September 2018. Augmented Dickey Fuller Test (ADF) p-value = 0.91 ($\alpha = 0.05$, alternative = stationary)

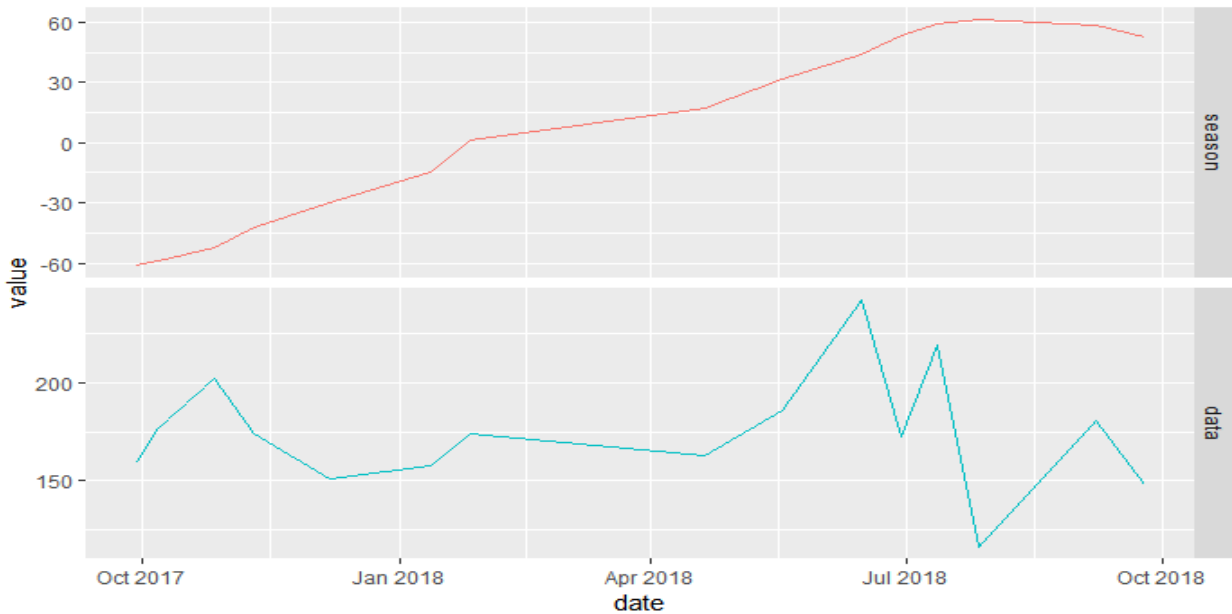


Figure 2.12 The decomposed timeseries of the mean flux of CO₂ from September 2017 to September 2018 into seasonal effect and raw data with the ungulate disturbance effect removed.

A Fourier's transformation was used to extract the seasonal trend from the year of data from September 2017 to September 2018. Figure 2.12 shows higher CO₂ flux in the summer months than in the late fall or winter. Figure 2.9 also found higher soil temperature and soil moisture in the summer months leading to correlation with the timestamp of the higher CO₂ flux.

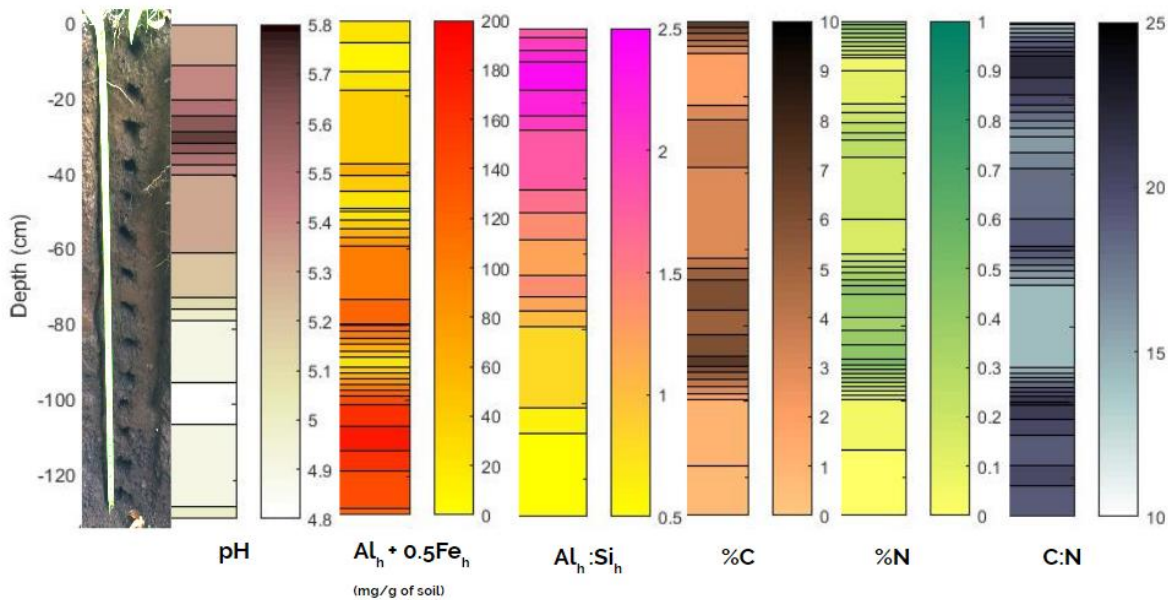


Figure 2.13 Soil pit profiles from 0 to 130cm at the Lyon Arboretum fieldsite for pH, Non crystalline minerals ($\text{Al}_h + 0.5\text{Fe}_h$), $\text{Al}_h:\text{Si}_h$ ratio, %C, % N and C:N ratio from November 2017 sampling.

The soil pit sampling from each 10cm of the 130cm pit show the results from pH, C, N and non-crystalline mineral tests. The pH gets more acidic in moving down the profile. The non-crystalline mineral content ($\text{Al}_h + 0.5\text{Fe}_h$) increases with depth. The Al:Si ratio ($\text{Al}_h:\text{Si}_h$) decreases with depth. The carbon content (%C) is highest at the surface and between 60 to 80cm. Nitrogen content (%N) is also the highest at the surface and 60 to 80cm. The C:N ratio is greatest 0 to 20cm and 100 to 130cm. The soil pit sampling results were used as preliminary data to inform the deep soil warming experiment in Chapter 4.

2.5 DISCUSSION

The initial hypothesis that there is no seasonal trend for the CO₂ flux at the surface on the study site was rejected. There is a seasonal trend among the yearlong sampling period from September 2017 to September 2018. Initially the heatmaps of the surficial CO₂ flux showed hotspots in the months of February and March, which were also months at which ungulate disturbance is documented (Figure 2.78). At the sampling locations where there was visible grubbing from ungulates there are also visible “flare ups” in microbial activity as predicted by increased surficial CO₂ flux (Figure 2.8). Ungulates increase the quantity and quality of nutrients in the soil from the surface organic matter and therefore increase the material available for microbial decomposition (Hobbs 1996). In Switzerland, grubbing by the same species of feral pig (*Sus scrofa*) found in Hawaii, increased CO₂ flux by 23.1% compared to plots that did not experience grubbing (Risch et al., 2010). Given the high amounts of carbon within tropical soils found here in Hawaii, the increase of CO₂ flux by grubbing of invasive feral pigs presents an important issue left to be studied. It is unlikely that feral pigs will influence large scale emissions, however, without proper culling, populations could increase CO₂ emissions dramatically.

With the disturbance effect from feral pigs removed, there is still an existing seasonality effect present in the heatmaps. In the summer months of June and July there is an increase in the mean CO₂ flux most likely because rising air temperatures increase soil temperatures (Figure 2.10). However, the small change in winter to summer temperatures is unlikely to be the only factor effecting CO₂ flux. Soil moisture is strongly correlated with microbial activity and has a parabolic effect on microbial activity, with too dry or too wet soil decreasing microbial metabolism. The summer months with higher soil temperature also saw higher soil moisture (Figure 2.9). The relationship between soil temperature, moisture and CO₂ flux will be tested in Chapter 4 further.

2.6 CONCLUSION

The initial hypothesis that the sites surficial CO₂ flux does not have a seasonal component was rejected. Using an autocorrelation plot (ACF) of the average surficial CO₂ flux across the timeseries, there was evidence of a seasonal effect show by the relationship between lag periods. The seasonality effect was determined further using an Augmented Dickey Fuller (ADF) test for stationarity. The P value of 0.91 ($\alpha = 0.05$) supports the null hypothesis that the data is non-stationary. Since the sampling period was under 2 years minimum to detect a seasonal trend of CO₂ flux, we were unable to use traditional timeseries seasonality detection methods. Instead, Fourier transformation was used to detect sine and cosine signals in the data. Two periods were detected by the Fourier transformation suggesting surficial soil respiration has a period of higher CO₂ flux and lower CO₂ flux.

There was higher CO₂ flux in the summer months for the sampling period of September 2017 to September 2018, which proved to be a statically significant seasonal effect. The amount of CO₂ flux was a function of soil temperature and soil moisture and this relationship will be explored further in Chapter 4. The lack of representative temperature and soil moisture observations across the entire fieldsite effects the ability to show possible correlations between soil temperature and soil mositure changes and changes in CO₂ flux

The effect of ungulates increasing CO₂ flux was shown by this study and could be studied further as an important component of invasive species management. The ungulates created large hotspots of soil respiration with their rutting, showing their unique effect on soil microbiology.

CHAPTER 3 : CREATION OF A LOW-COST TEMPERATURE NETWORK FOR
MANIPULATIVE DEEP SOIL WARMING EXPERIMENTS



Figure 3.1 Soldering the cable to the soil temperature sensor (left). Intern Mathilde holding up the completed soil temperature sensors (right).

3.1 INTRODUCTION

The critical need for soil warming experiments across diverse climates and soil types is felt now more than ever. Greenhouse gases like carbon dioxide (CO₂), methane (CH₄) and nitrous oxide (NO₂) have been rising since the industrial revolution and raising the global air temperature by trapping heat emitted by the Earth's surface. This rise in air temperature is expected to affect many natural processes like precipitation, sea level rise and biodiversity. One of the less appreciated effects of this temperature rise is the effect on soil. Global soil temperatures are expected to rise at the same rate as global air temperatures affecting many soil processes in return (Pries et al., 2017). Soil gas exchange, water holding capacity, agricultural productivity and carbon (C) storage are some of the important soil processes that could be affected by climate change.

Quantifying the consequences climate change may bring to soil processes is one of the hardest tasks climate change modelers face because of lack of empirical data (Crowther et al., 2016). Most models focus on the impact of rising CO₂ on the landscape; however, it is difficult to get accurate prediction on how the rise of CO₂ will impact the future without observed evidence of the soil temperature and soil respiration relationship for different climate types. The International Soil Experimental Network (iSEN) is a call to fulfill this niche for research on the effects of soil warming on the release of CO₂ from the soil, especially in the severely understudied deep soil (>30cm) (Torn et al., 2015). This network is still developing and lacks many of the critical soil and climate types that are especially vulnerable to climate change.

Arctic and temperate systems comprise the vast majority of soil warming experiments. Arctic systems make up most soil warming experiments because of the distinct threat of permafrost melting as air temperatures at the poles increase rapidly and the SOC that has been locked within the soil for millennia is now exposed to decomposition. Temperate systems also are covered by

the soil experimental network because of their proximity to universities and research institutions that can support systems that require many resources and trained staff. Tropical systems are nearly absent from the network of soil warming experiments. Tropical systems, especially those on islands, are extremely vulnerable to climate change and should be integrated into the iSEN.

Current designs for soil warming experiments can be costly and require resources many research institutions may not have available. One experiment in the boreal forests of Maine heated only the upper 5cm of the surface soil using buried heating cables (Rustad and Fernandez, 2004). This design neglects the important effects of warming on deep soil which is predicted to hold up to 80% of the worlds SOC beyond 20cm (Jobbágy and Jackson, 2000). Another study on the effects of soil warming took place on a temperate Alfisol, used both buried heating cables and deep soil heating rods (Pries et al., 2017). This study included the important deep soil component heating the soil 2.6m down the soil profile. The design included a manipulated soil heating treatment of ambient +4°C and a control with no heating, lacking a gradient of soil heating treatments. Given the uncertainty within climate models, a gradient of heating treatments could provide valuable information for different scenario outcomes strengthening the models. The Spruce and Peatland Responses Under Climatic and Environmental Change (SPRUCE) project studied the effects of whole ecosystem warming on a boreal forest. Large enclosed chambers heated plots of soil and forest via infrared heaters and deep soil heating rods to establish a gradient of temperatures expected from varied global temperature rise projections (Hanson et al., 2017). This study is one of the most effective in including temperature gradients for whole ecosystem heating, however, systems like this are very costly. In order to include soil and climate types that are currently absent from the iSEN network, low cost soil warming experimental methodologies must be explored.

3.3 METHODS

3.3.1 Fieldsite design

Randomization scheme for heating, monitoring and sampling

The objective of this study was to create a low cost, novel temperature system network to study the effects of a gradient of soil heating on the fate of soil organic carbon (SOC) in a tropical soil. This experimental methodology looked at the effects of a gradient of heating, from 0-4°C above ambient temperatures on various soil processes involving SOC. To create a non-biased sampling scheme, locations of soil heating, soil temperature monitoring and soil sampling were determined using a randomized block design. The site was delineated into 5 blocks of similar area and surficial soil C flux using the GRACEnet protocol data from Chapter 2. Areas of existing “hotspots” were not included in the blocking scheme allowing a homogenized initial surficial soil C flux before manipulative heating was started.

The five randomized blocks were gridded into 1x1m sections to randomly select the locations of the five heating probes. Using the list of gridded 1x1m sections per block, atmospheric noise was used to determine which grid intersection would be the location of each of the five heating probes. Figure 3.2 shows the locations of the five heating probes for the five blocking within the randomized design. Location selection for the gas wells (for measuring CO₂ produced) and soil temperature sensor sampling locations also used the randomization by delineating the 1x1m grids into quadrats and selecting ten locations for sampling by each of the five blocks. To ensure equal distribution of depths of interest per block, two of each sampling depth of interest of 20, 40, 60, 80 and 100cm were assigned to each block (Appendix A). Ambient soil temperature sensors were selected to control the rate of heating for the heating probes. The ambient soil temperature sensors were selected from the original 50 soil temperature sensors based off their

proximity from the heaters (outside the zone of heating) at a depth of 60cm An additional five temperature sensors were installed at the expected radius of heating of 0.7m from the heating probes at 60cm in depth to monitor the rate of soil heating.

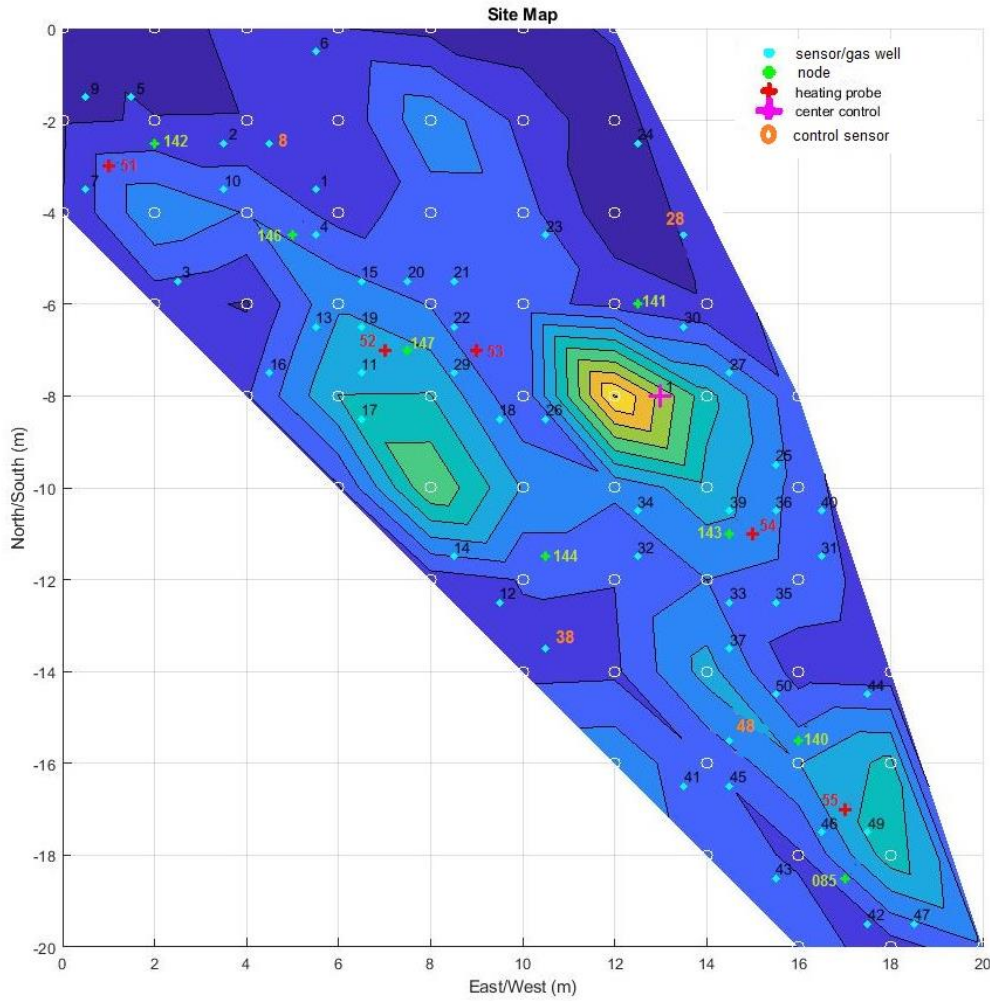


Figure 3.2 Randomization design for the hillslope at Lyon Arboretum, including the locations of the sensors, data loggers (node), heating probes, central data logger (center control) and the control sensors overlaid on the surficial soil respiration “hotspots”

Heating probes and temperature sensors design

The five heating probes were produced from 3/4in. Electric Metallic Tube (EMT) conduit with a custom welded pointed tip for installation purposes. The heating probes were 2.5m in length

to allow for full profile heating. The heating probes had 2.5m of conductive electrical wire (120V, 10W/ft, Brisk Heating SLCAB Self Regulating cable) running down the length of the conduit and coral sand filled around the cable to allow heat to conduct to the outside of the EMT conduit. Each heating probe included its own temperature sensor to monitor the rate of soil warming at a depth of 60cm with a radial distance of 0.7m away from the probe. The heating probes warmed the soil +4°C (IPCC RCP 8.5 model) above the ambient soil temperature using a proportional–integral–derivative (PID) controller, which turned the heaters on and off. The ambient soil temperature used for the PID controller was averaged from four temperature sensors outside the expected radius of heating at a depth of 60cm and the average ambient temperature +4°C was the target temperature for the heaters.

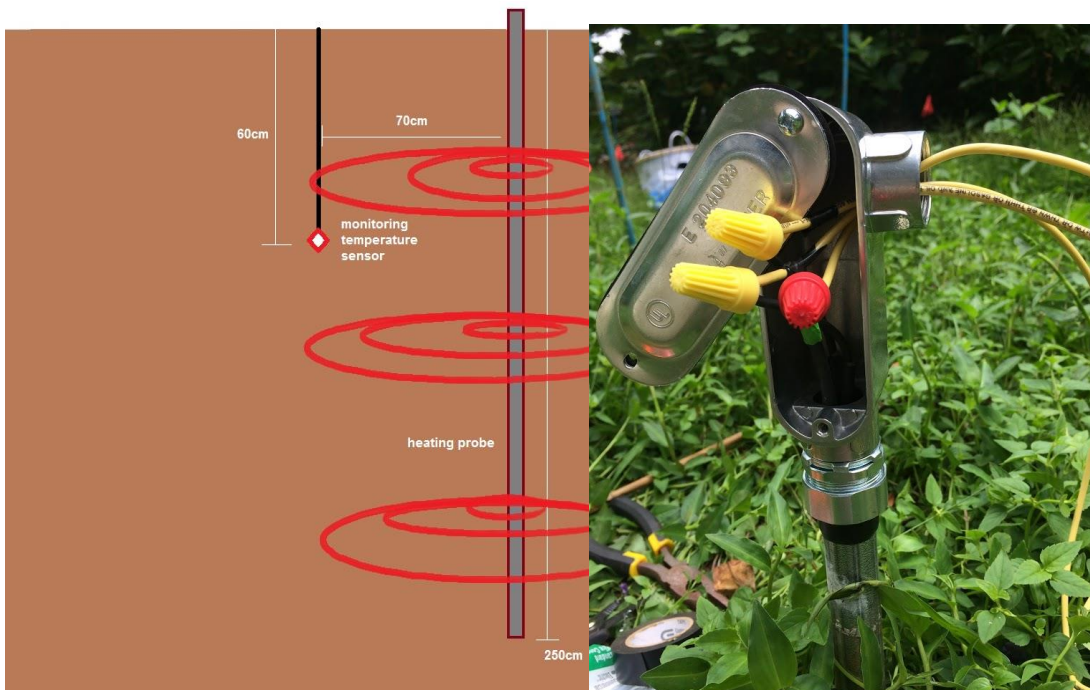


Figure 3.3 Diagram of the 2.5m heating probe with monitoring temperature sensor 0.7m away within the soil profile (left). The wiring connection on the inside of the heating probe in the field (right).

The temperature sensor consisted of a single sensor mounted on a board (TSYS01, custom made by UH Manoa MESH lab) and enclosed in a 3ml polystyrene test tubes filled with epoxy. The test tubes were used as an inexpensive sensor waterproofing substitute to more technical heat shrink wrap and found to have equal conductivity capacity. Using a small soil probe the temperature sensors were installed at each depth of interest for the sampling locations across the site. The temperature sensors were connected to a multiplexer (Texas Instruments, TCA9548A, custom made by UH Manoa MESH lab) by multi-conductor cable (Digi-Key, 4 Conductor Multi-Conductor Cable Slate 26 AWG Foil). The multiplexer forwarded digital signals from the temperature sensors to a datalogger (Raspberry Pi 3, Model B - ARMv8) enclosed in a weatherproof case (1450 Pelican case). The datalogger then logged the temperature sensor readings every 30 seconds and sent it to the control center via Ethernet (CAT6 Outdoor UV Resistant Ethernet Cable). The control center is the main data logger that manages the output signals from the temperature sensor data loggers and uploaded the data via Wi-Fi for remote data access via <http://grogdata.soest.hawaii.edu/>. The control center also housed the PID controller for the regulation of the heating probes as well as the power source for the temperature sensor data loggers and the heating probes which gets power from the Lyon Arboretum visitors center. AC power is provided to the heating probes and a DC converter is used to provide DC power to the temperature sensor data loggers.



Figure 3.4 The temperature sensor and multi-conductor cable inside the epoxy filled test tube (left). The multiplexer connected to the datalogger in the casing (center). The main control center for the temperature sensors and heating probes (right).



Figure 3.5 Diurnal soil temperature cycling at 20cm from the SMART Ala Wai project's livestream database of the real time soil temperatures at the study sites at the Lyon Arboretum for September 4 to 7 2019 with the scroll over option to select a single timepoint showcased.

Gas wells

Gas wells were used to measure soil respiration at depth. The gas wells were made of 1/4in. stainless steel seamless tubing (Swagelok). The gas wells were cut to correspond with the

depths of interest for soil respiration sampling (20, 40, 60, 80, 100cm) when installed at 45° to minimize any influence from existing preferential flow paths. Three gas wells were installed at each of the sampling locations to determine the flux gradient per the depth section and calculate the CO₂ produced by Fick's Law (Appendix B, Equation 3.1) and the diffusion coefficient (Equation 3.2) (Moyes and Bowling, 2013).

$$F = -D \frac{dc}{dt}$$

Equation 3.1

Where F is the flux, D is the diffusion coefficient and $\frac{dc}{dt}$ is the change in concentration over time. The diffusion coefficient was determined by Equation 2:

$$D = D_{ao} \left(\frac{T}{293.15} \right)^{1.75} \left(\frac{101.3}{P} \right) \xi$$

Equation 3.2

Where D_{ao} is the diffusion coefficient of CO₂ in soil, T is temperature in °C at time of sampling, P is local atmospheric pressure in kPa, and ξ is a dimensionless tortuosity factor. The CO₂ produced by depth section was possible by installing gas wells at the depth of interest - 20cm, the depth of interest, and the depth of interest + 20cm. For the depth of interest of 20cm, a surface collar was used along with a gas well at 20cm and 40cm to get the flux gradient.

Proper installation of the gas wells was very important to ensure accuracy of the CO₂ produced per depth section. A wooden guide was used to guide each gas well in at 45°. A carbon steel rod was inserted into the hollow gas well allowing it to be hammered into the profile without being inundated with soil. The carbon steel rod was then removed, and the hollow gas well was topped with a 1/4 in brass straight union (Swagelok) with a septum at the top. The gas wells sat for

one month before field sampling in order to avoid any effects from the initial disturbance of installation.



Figure 3.6 Cross section of a sample set of gas wells within the soil profile (left). Gas wells installed in the field topped with straight unions (right).

Soil moisture probes

Soil moisture is an important function of soil temperature and soil respiration, therefore we also sampling soil moisture. Soil moisture was measured using a 1.5m 2000 Diviner soil moisture probe (Sentek) at 30 locations across the fieldsite and connected to the temperature sensor and gas well sampling locations within a 0.5m radius of the soil moisture probe. The probes were a onetime installation of the probe plastics fitted with a waterproof cap on top at the soil surface. The soil moisture is measured via conductivity with a Diviner soil moisture rod. This method of measuring soil moisture is widely used and not part of the novelty of the study. There were issues with the Diviner soil rod not reading soil moisture correctly in August 2019 and therefore the Lyon weather station with a surface soil moisture probe was used to interpolate the soil moisture along with existing data, while the replacement part for the Diviner rod was acquired.

3.4 RESULTS AND DISCUSSION

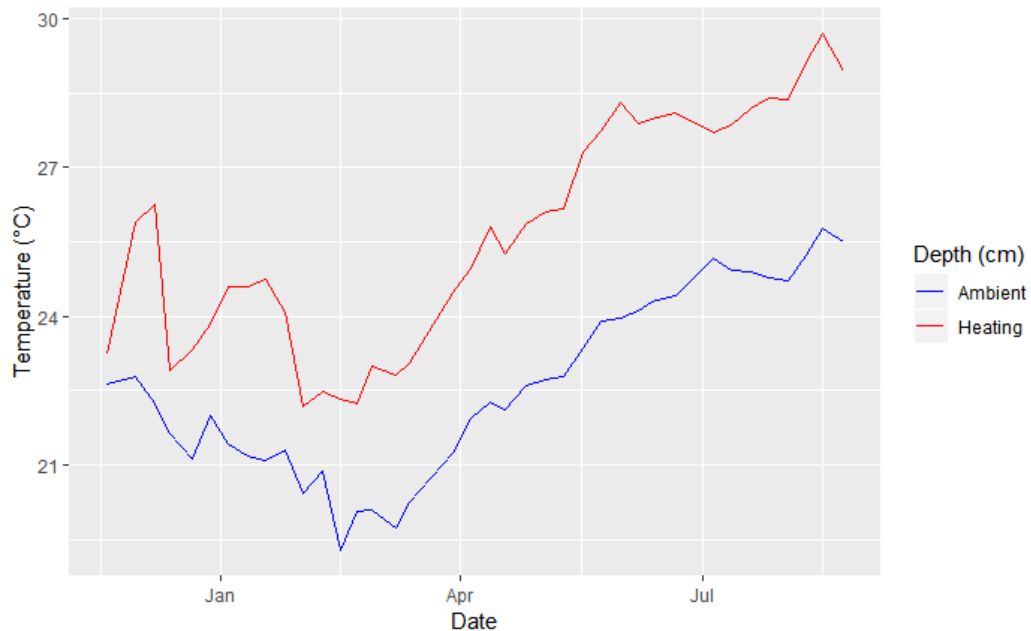


Figure 3.7 Average soil temperature for ambient soil temperature sensors and heater controller temperature sensors (at 60cm) for the sampling time period at the Lyon Arboretum.



Figure 3.8 Δ soil temperature between average ambient soil temperature and heated soil temperatures for the sampling time period at the Lyon Arboretum. The red dashed line is the target delta soil temperature of 4°C (ICP RCP 8.5 projection.), the yellow dashed line is the mean Δ soil temperature.

The ambient soil temperature sensors follow the same trend as the heated soil temperatures sensors but there is a difference in mean soil temperatures between ambient and heated because of the targeted +4°C from ambient to heating the soil profile (Figure 3.7). Figure 3.8 is a detailed plot of this difference overtime as heated soil temperatures – ambient soil temperatures. Before April the average Δ soil temperature varied greatly, because of many technical difficulties. After April the system was able to maintain an average Δ soil temperature between 3 - 4°C. Even though the average Δ soil temperature varied significantly, individual soil temperature sensors within the radius of heating were able to maintain the +4°C across the timeseries, preserving the initial target of a gradient of soil temperatures.

There are several inconsistencies within the average Δ soil temperature across time that were consequences of creating low cost pilot temperature system for a deep soil warming experiment. In late November 2018, the heating system was turned on and the initial ramp up to +4°C for the heaters is shown by December 2018 (Figure 3.8). In late December 2018, there was vandalism to the site that compromised some of the dataloggers and required completely new installations of sensors and dataloggers at the site. This affected the ability to communicate with some of the ambient and heating control temperature sensors therefore there is a dip in the heating across the site because the PID controller was compromised by lack of data to control the heaters. In both late February and July 2019, there were connectivity problems to the internet via the Visitors Center. Unanticipated maintenance required the internet be shut off for several days which did not allow the sensors to communicate with the heaters. In this situation the heaters are programmed to shutdown to avoid catastrophic overheating of the soil which could destroy microbial communities. These unexpected shutdowns in the heating made maintaining an ambient +4°C soil temperature at the radius of heating difficult however, Figure 3.9 displays how a +4°C

soil temperature was still maintained at locations within the radius of heating. Therefore, the goal of a gradient of heating from 0-+4°C soil temperature was still acquired.

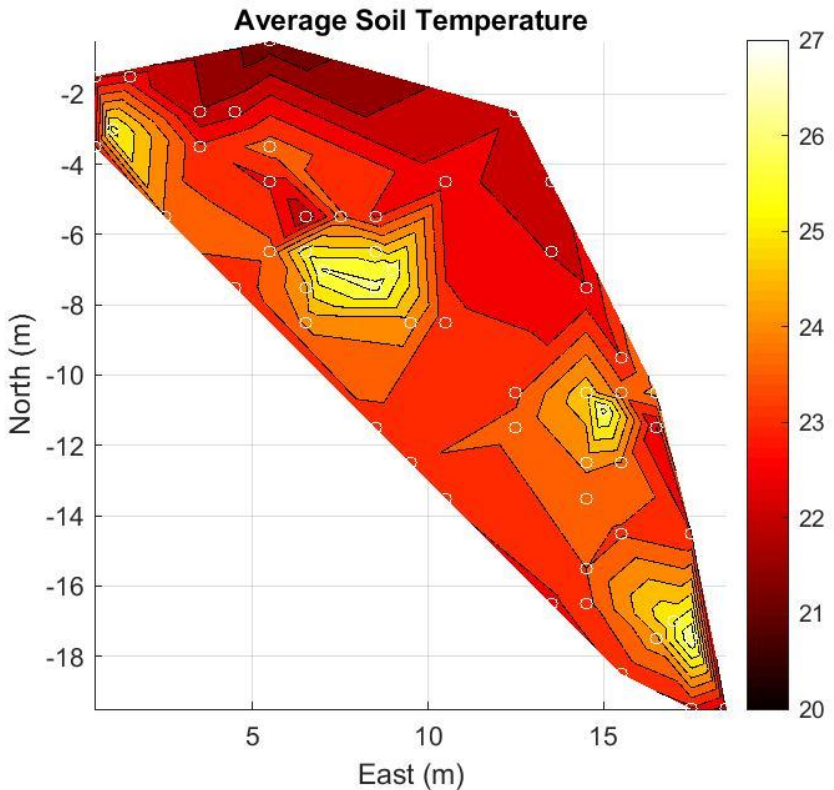


Figure 3.9 Average soil temperature across the fieldsite from November 2018 to August 2019 at the Lyon Arboretum. The white dots are the sampling locations

The fieldsite had a gradient of average soil temperatures based off proximity to the heating probes (Figure 3.9). The sampling sites closest to the heating probes were the “hotspots” of the site shown in bright yellow. The farther away the temperature sensors were from the heating probes the cooler the soil temperature. This heatmap validates that even though there were inconsistencies within the average Δ soil temperature at the radius of heating, soil temperature sensors within the radius of heating achieved the +4°C from ambient over time.

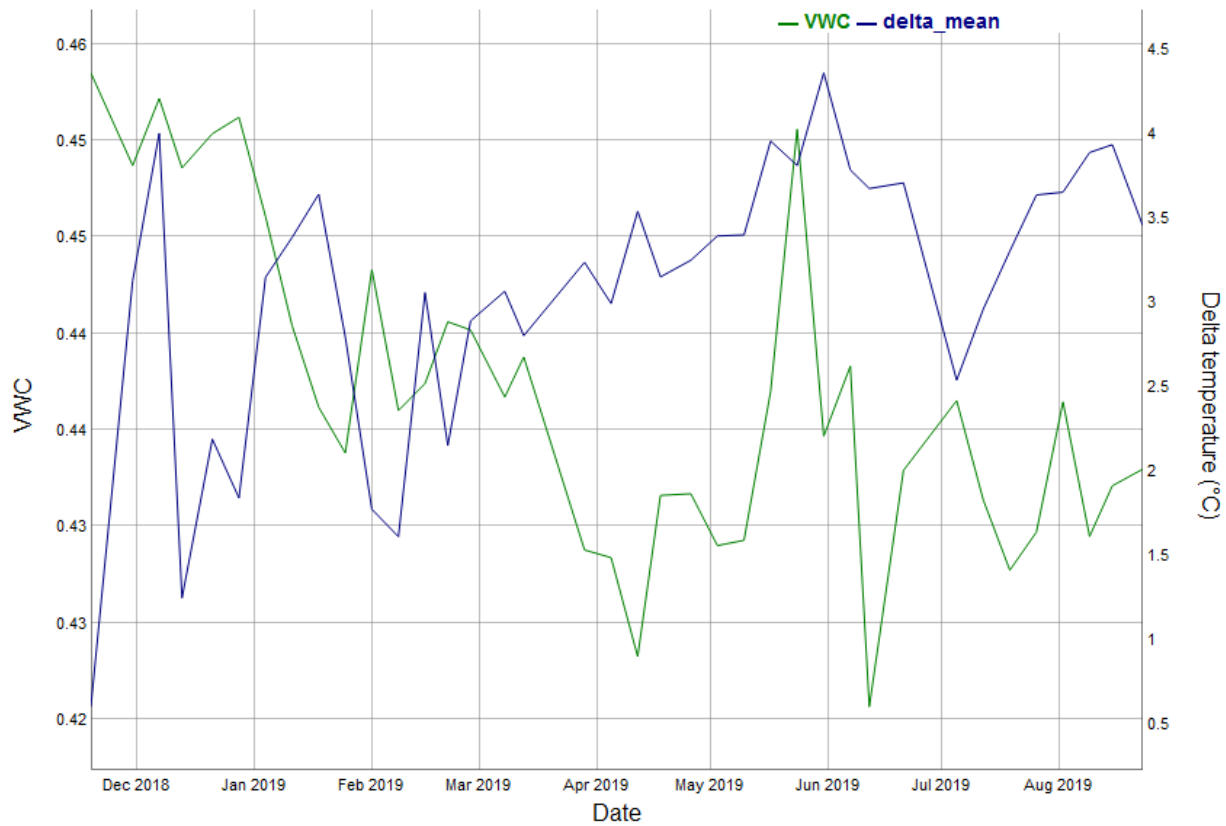


Figure 3.10 Average Δ soil temperature and average volumetric water content (VWC) for the control sensors for the sampling time period at the Lyon Arboretum

There are apparent relationships between soil temperature and soil moisture. Large changes in soil moisture effected the soil temperatures. Wetter soil was warmer while drier soil was cooler. This is most likely due to the heat capacity of water effecting the ability of the soil to hold more heat in its pore space. More water means higher heat capacity of the soil and less water means lower heat capacity for the soil. Figure 3.10 shows some instances of this phenomenon effecting the soil temperature at the fieldsite. When the soil had lower soil moisture it took longer for it to get up to temperature at the radius of heating compared to wetter sampling time periods.

3.5 CONCLUSION

With improvements to this low cost, novel deep soil heating and sensor system it has potential to put many new soil and climate types into the iSEN, that otherwise could not receive adequate funding. Large scale deep soil warming projects can be costly to build and maintain. In order to add more empirical data to strengthen climate models with changing soil carbon components, low cost deep soil warming, and sensor networks are needed to include the effects of deep soil warming on soil carbon in underrepresented climate and soil types like the very important tropical soils. Improvements on network security and connectivity can allow more systems like the Lyon Arboretum deep soil warming project to provide accurate and critical data to soil carbon and climate models.

The Lyon deep soil warming project maintained a gradient of soil temperatures from 0-4°C, despite some setbacks that come with troubleshooting a novel methodology. The novel methodology included robust soil temperature sensors that measured the soil temperature at different depths (20, 40, 60, 80, 100cm) in real time. The low-cost soil temperature sensors were adapted by the SMART Ala Wai project from their original stream temperature sensor design. The data from the soil temperature sensors was updated real time to an online database, by low cost dataloggers, that allowed for remote monitoring of the soil temperature sensors. The soil temperature sensors controlled the rate of soil heating from the soil heating probes. The soil heating probes were based off Pries et al. and were 2.5 steel conduit with Brisk heating cable inside and backfilled with sand to allow for conduction of the heating cable to the soil. The ambient soil temperature was measured outside the radius of heating and fed back to the PID controller which kept the radius of heating from the heating probes (0.7m) a consistent 4°C above the average ambient soil temperature mimicking the effects of the IPCC RCP 8.5 (business as usual) model.

Soil temperature sensors closest to the heaters experienced the greatest degree of heating while the soil temperature sensors the farthest away from the heaters experienced the lowest degree of heating.

Several setbacks influenced the rate of heating at the fieldsite. In late November 2018, the heaters were turned on and it took a month for the soil to reach the target +4°C. In late December 2018, site vandalism compromised some of the dataloggers requiring new installations of sensors and dataloggers at the site. The period between the vandalism and the new deployment of datalogger affected the ability of the soil temperature sensors to communicate with the soil heaters and therefore there was a dip in the target soil heating rate. In both late February and July 2019, there were connectivity problems to the internet via the Visitors Center. Unanticipated maintenance required the internet be shut off and in this situation the heaters are programmed to shutdown to avoid catastrophic overheating of the soil which could potentially destroy microbial communities. These unexpected shutdowns in the heating made maintaining an ambient +4°C soil temperature at the radius of heating difficult however, the target +4°C soil temperature was still maintained at locations within the radius of heating. Therefore, the goal of a gradient of heating from + 0-4°C soil temperature was still acquired.

This study provides a novel methodology as a low-cost option to traditional soil warming experiments. Traditional warming experiments are expensive to install and maintain and the high cost inhibits new soil warming experiments from entering the soil warming experimental network. By creating a randomization design to allow for an unbiased gradient of temperatures, this novel methodology eliminated the need for treatment and control replicates that quickly add up overall costs. Beyond this, collaborating with the SMART Ala Wai project allowed for the creation of site-specific sensors that were designed to withstand high heat and moisture, that were simple

enough to keep costs low. The dataloggers were created from low cost Raspberry Pis that uploaded the soil temperature data in real time allowing for remote monitoring of the soil temperature system. The heating controller was also custom built by the SMART Ala Wai project, which cut down costs. The Lyon deep soil warming heating controller was only 15% of the cost of one of the heating controllers at the Blodgett Experimental Forest (Pries et al, 2017). The in-house production of custom temperature sensors and dataloggers greatly decreased the cost as compared to soil warming experiments that order prefabricated sensors and data logging systems.

Overall, the Lyon deep soil warming experiments novel methodology provides a viable option for deep soil warming experiments that lack adequate funding. By creating a randomized soil warming experimental network, a successful gradient of soil temperatures from + 0-4°C was achieved at the select study depths of 20,40,60, 80 and 100cm. This design, with improvements to network security and connectivity, can aid in creating more deep soil warming projects to inform global carbon and climate models with empirical data.

CHAPTER 4 : INTERACTIVE FEEDBACKS OF CLIMATE, MINERALOGY AND
MICROBIAL COMMUNITIES ON SOIL CARBON



Figure 4.1 Looking upslope at the fieldsite at the Lyon Arboretum and novel temperature sensor system in August 2019.

4.1 INTRODUCTION

Climate change is the largest issue facing humanity today. Natural systems exist that could potentially drawdown large amounts of carbon from the atmosphere and aid in the preservation of global ecosystems while long term solutions to destructive human behavior are enacted into policy. Soils are one such system with high potential to drawdown carbon and reduce atmospheric greenhouse gas concentration. But, this benefit may only occur if the mechanisms for stabilizing and storing carbon are not overwhelmed by the interactive effects of rapid warming on multiple soil processes.

Empirical evidence for how deep soil processes (>30cm) will react to the rising global temperature is lacking. The International Soil Experiment Network (iSEN) documents the effects of deep soil warming on the global carbon cycle, but tropical soils are underrepresented, and young volcanic soils, called Andisols, are absent (Torn et al., 2015). Andic soils are a critical end member for iSEN given their intrinsic ability to stabilize carbon through their unique mineralogy, which could have immense carbon drawdown potential.

Andisols are a unique soil order found in only 0.84% of the worlds surface area and are derived from volcanoclastic parent material (Leamy, 1984; McDaniel et al., 2012). Andisols have unique soil properties including, variable charge, high water retention, low bulk density, and highly stable soil aggregates making them a highly desirable soil for anthropogenic resources, like agriculture (Shoji et al., 1993). These volcanic ash derived soils are rich in aluminum and iron, specifically, non-crystalline or short-range order minerals of allophane, imogolite, ferrihydrite and organically complexed Al/Fe (Shoji et al., 1987; Shoji and Ono, 1978). Aluminum as a colloid in humid soil environments exists in a continuum between purely organically complexed Al/Fe (non allophanic) and pure allophane and imogolite (allophanic) (Mizota and Reeuwijk, 1989). The

organically complexed Al colloids are the dominant form of active Al (acid oxalate-extractable Al) within non-allophanic soils (Takahashi and Dahlgren, 2016).

Andisols hold a disproportionate amount of soil organic carbon (SOC) for their global spread. While Andisols are the worlds least common soil order, they hold 1.8% of the worlds soil organic carbon (SOC) (Hillel and Rosenzweig, 2009). This is partially due to the capabilities of this soil to stabilize soil organic matter (SOM). SOM in non-allophanic Andisols bond to active Al and Fe in the soil to form organo-mineral complexes. SOM has a unique affinity to amorphous Al and Fe clays because of the high surface area and charge. The complexity of this phenomena is not fully understood however, studies have linked the complexation of multivalent cations (ie. Al^{3+}) with OM resulting in condensed functional groups making them less susceptible to decomposition (Balldock and Broos, 2011). For this reason, Andisols can be considered an end member soil order in terms of mineralogical controls on SOM decomposition, displaying unique organo-mineral complexes.

Within these stabilization properties for Andisols, it was found that SOC stock and turnover did not vary across a 5°C mean annual temperature (MAT) gradient across Hawaiian tropical montane forest system (Giardina et al., 2014). It should be noted that the MAT gradient is not representative of the intensive warming over a short time period that may result from climate change. Therefore, the stability of the carbon sequestration properties under the pressures of climate change are still unknown. Hawaiian tropical Andisols are an ideal place to study the mineralogical controls of Andisols and whether they resist soil warming under manipulative deep soil heating conditions.

4.2 OBJECTIVES AND HYPOTHESES

The objectives are outlined below along with the corresponding hypothesis, broken down into a prediction, justification, and approach.

4.2.1 Objective

Understand the disturbance effect of soil warming on soil respiration along a deep soil profile for a Hawaiian Andisol and if Al/Fe organo-mineral complexes exert a mineralogical control on soil respiration especially at depth.

4.2.2 Hypothesis

If soil respiration follows the Arrhenius equation, then as temperature increases, soil respiration rates will initially rapidly increase and then level off, indicating a threshold of warming which is controlled by Al/Fe organo-mineral complexes especially at depth.

4.2.3 Prediction

It is expected that with increased soil temperature from rapid heating disturbance, there will be an increase in overall soil respiration. The initial increase in soil respiration under warming will be rapid and then gradually level off the rate of soil respiration over time. Areas with the highest concentration of Al/Fe organo-mineral complexes (most likely at depth >30cm) will resist changes to soil respiration by augmented soil warming.

4.2.4 Justification

Conceptual model –Soil respiration rates in Andisols will have logistic growth over time with consistent manipulative warming and will likely reach a soil respiration threshold where soil respiration will increase rapidly in the initial stages of heating then gradually decrease in the rate of respiration until a “threshold of warming” is reached. The threshold of warming will be controlled by Al/Fe organo-mineral complexes that exhibited similar control across a 5°C MAT in the Giardina et al (2014) study. The soil respiration rate with intensified warming overtime will likely follow Arrhenius equation:

$$k = Ae^{-\frac{E_A}{RT}} \quad \text{Equation 4.1}$$

Where k is the rate coefficient, A is a constant, E is the activation energy, R is the universal gas constant and T is temperature (Arrhenius, 1889). The Arrhenius equation is used for measuring reaction rates to increases in temperature. It is expected that this relationship will look like the model below:

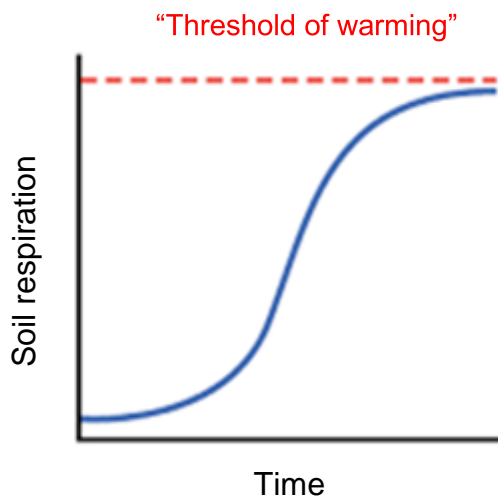


Figure 4.2 Relationship between soil respiration and time with period of intensified warming.

Initial data – Initial data was collected from September 2017 to September 2018 on the rates of surface soil respiration to establish the heterogeneity of the site (Chapter 2).

Following the GRACEnet protocol, the flux of CO₂ coming from the soil surface was estimated over time and developed into heatmaps to visualize the changes in flux. These flux maps cover over a year of soil moisture and temperature gradients for the entire fieldsite. The heatmaps of the CO₂ flux determined the randomization design by identifying soil respiration “hotspots” that are excluded from the potential locations for probe placement. This ensures initial homogeneity of the soil respiration across the fieldsite.

4.2.5 Approach

The approach to this objective was to heat the deep soil profile using 2.5m heating probes at five randomized locations across the hillslope to get a gradient of deep soil temperatures, which was measured by the novel temperature sensor network. CO₂ was measured from gas wells down the soil profile to 1m to measure the effects of deep soil profile heating on soil respiration in a Hawaiian Andisol. Information on the inherent soil properties like non-crystalline minerals and SOC was sampled before warming occurs to analyze across the gradient of soil warming.

4.3 METHODS

4.3.1 Field Sampling

Soil pit sampling for soil characterization

The site was sampled at 50 randomized locations from 0-100cm to characterize the soil profile across the hillslope. Soil sampling was performed using the JMC Environmentalist's Subsoil Probe. The depths sampled at each location were 20, 40, 60, 80 and 100cm. The sample was then homogenized and frozen at -20°C for later analysis. After homogenization and before freezing approximately 10g of field moist soil was weighed and put into a tin to air dry. After recording the air-dry weight, the samples were then oven dried at 60°C for 48 hours and the weight was recorded. Then the 60°C oven dried soil samples were passed through a 250 micron sieve and stored in labeled scintillation vials. An additional 10g of field moist soil was weighed out and placed into a tin to be oven dried at 105°C for 48 hours and recorded as the dry weight of the soil.

This dry weight is used to find the moisture content of the soil.



Figure 4.3 Soil sampling using the JMC Environmentalist's Subsoil Probe in the field in June 2018 (left). The 3cm diameter, 1m depth hole, leftover from each sampling that eventually caved in a few weeks after sampling completion leaving no air large air gaps.

4.3.2. Laboratory Analysis

Soil carbon and nitrogen

Soil carbon and nitrogen levels were determined from the 50 randomized soil sampling locations on the hillslope. Using a microbalance ~10 μ g of 60°C oven dried, and 250-micron sieved soil were packed into aluminum tins. Then these samples were processed in a Perkin Elmer Elemental Analyzer to determine the percent carbon in each sample.

Soil pH

Soil pH was determined from field moist soil samples at the 50 randomized hillslope locations. First, 5g of field moist soil was weighed out into Falcon tubes (taking out only ten samples at a time to preserve field moist conditions). Then, 15mL of deionized water was pipetted into Falcon tubes (using 2 (water): 1 (soil) ratio). Next, the Falcon tube is vortexed 30 seconds and left to sit for 30 minutes. Using the VWR soil pH meter the bulbous tip of soil probe was placed into the soil solution until the pH meter stabilizes with a value and then it was recorded. This same protocol was used for the KCl pH solution method using 1M KCl solution instead of deionized water. Using both the deionized water pH method and the KCl pH method, Δ pH can be found by Δ pH = KCl pH - deionized water pH.

Non-crystalline mineral extractions

Three different extraction methods were used to determine the Fe, Al and Si content of the 50 randomized locations across the hillslope. These extractions are hydroxylamine hydrochloride, citrate dithionite, sodium pyrophosphate. The hydroxylamine hydrochloride extraction is based off methods found in Ross et al. (1985). For the hydroxylamine hydrochloride extraction 0.100g of

field moist soil was weighed and added to a 50ml Falcon tube. Then, 25ml of 0.25M hydroxylamine hydrochloride and 0.25M hydrochloric acid was pipetted into each Falcon tube and placed on an end over end shaker for 16 hours. After, the samples were centrifuged at 1500rpm for 20 minutes and filtered through 52 Whatman paper. Samples were stored in the fridge before being shipped for Inductively Coupled Plasma analysis (ICP).

The citrate dithionite extraction is based off methods found in Holmgren (1967). For the citrate dithionite extraction, 0.500g of field moist soil was weighed and added to a 50ml Falcon tube. Then 8g of sodium citrate, 0.50g of sodium dithionite and 30ml of deionized water was added to the Falcon tube, which was then capped and shaken for 15 seconds and then uncapped to off gas. The Falcon tubes were then capped again and placed on an end over end shaker for 16 hours. Once off the shaker the solution was transferred into 50ml volumetric flasks and 12 μ l of Power Floc solution was added to each tube and covered with parafilm to shake for 15 seconds. Next the flasks were filled to volume with deionized water and shaken again for 15 seconds. The solution was then transferred back into the 50ml Falcon tubes and the samples were centrifuged at 1800rpm for 30 minutes and filtered through 52 Whatman paper. Samples were stored in the fridge before being shipped for Inductively Coupled Plasma analysis (ICP).

The sodium pyrophosphate extraction is based on methods found in McKeague (1967). For the sodium pyrophosphate extraction, 0.25g of field moist soil was weighed and added to a 50ml Falcon tube. Then, 25ml of 0.1M sodium pyrophosphate solution was pipetted into each Falcon tube and placed on an end over end shaker for 16 hours. After the samples were centrifuged at 20,000rpm for 15 minutes and filtered through 52 Whatman paper. Samples were stored in the fridge before being shipped for analysis. Before being shipped all extractions had 15ml of solution

added to 15ml Falcon tubes. 75 μ l of Yttrium was added to each 15ml Falcon tube for quality control. Then the samples were shipped to UH Hilo Analytical Laboratory for ICP analysis.

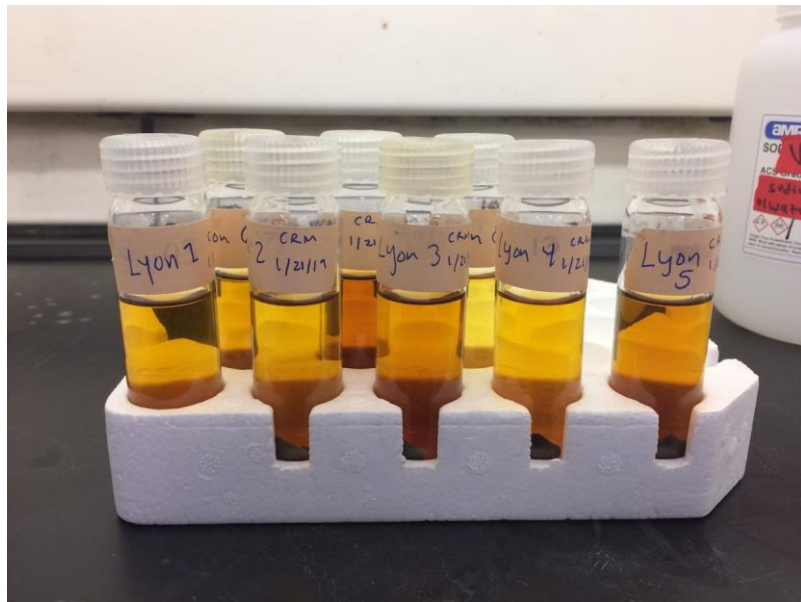


Figure 4.4 Sodium pyrophosphate extractions after being taken off the high speed centrifuge.

Microbial extractions and bioinformatics

Using the same 50 randomized locations used for the soil sample processing, the project looked at microbial communities across depth. Using the depth of interest for each of the 50 randomized soil sampling locations (Appendix A) the upper and lower 20cm around this depth of interest were also sampled for microbial communities, making 130 samples in total (top 20cm soil samples have no upper 20cm to sample). First, the DNA was extracted using the Qiagen DNeasy PowerSoil Kit following the Quick-Start Protocol. The extracted DNA was then quantified using Thermo Fisher Scientific NanoDrop One to ensure there is enough DNA extracted to start the PCR process. The PCR process for 16s and ITS was completed by CMAIKI and sent to UC Berkeley for sequencing of the library through the Illumina MiSeq system. Once the sequencing results were

returned, bioinformatics were performed using a pipeline created in Qiime 2.0 (**APPENDIX D**.
QIIME 2.0 ITS PIPELINE TAKEN FROM NHU NGUYEN MICROBIOLOGY LAB Appendix
EChapter 0

APPENDIX E. QIIME 2.0 16S PIPELINE TAKEN FROM NHU NGUYEN MICROBIOLOGY LAB).

4.3.3 Data Analysis

Several methods of data analysis were used to understand the data. Data included information on soil properties, timeseries variables and microbial properties with much of the data having a non-parametric distribution. For this reason, in order to model the most significant factors affecting the response of CO₂ production at depth, generalized additive modeling (GAM) was used since it is robust to both parametric and non-parametric data. GAM fits a smoother to each of the covariates and then adds up these smoothed relationships to predict the response variable (Hastie and Tibshirani, 1986). The GAM structure can be written as Equations 4.2:

$$g(E(Y) = \alpha + s_1(x_1) + \dots + s_p(x_p)) \quad \text{Equation 4.2}$$

Where Y is the respond variable, and E(Y) is the predicted value. $s_1(x_1) + \dots + s_p(x_p)$ are the predicted non-parametric variables fit with a smoothing function. To rule out spatial autocorrelation and subsequent geospatial analysis of the data a variogram was used to determine if any spatial correlation existed between the points. Given the results of the variogram and the small size of the study area it was determined geospatial analysis would not be valid and therefore we moved forward with non-spatial analysis techniques.

Before assessing collinearity with a correlation matrix and principal component analysis (PCA), an analysis on the seasonality of the time series variables of soil temperature, soil moisture (VWC) and soil respiration (CO₂ produced) was completed using the autocorrelation function

(ACF) and Augmented Dickey Fuller (ADF) test. Variables with a seasonal trend were transformed using a Fourier transformation to eliminate any confounding effect seasonality might have on selecting the most significant predictors of CO₂ production.

To inform the GAM model a correlation matrix and principal component analysis (PCA) was used on the data to understand the existing relationships and further eliminate collinearity. The correlation matrix was created using the “corrplot” package in R. The PCA was created using the “devtools” and “ggbioplot” package in R. A PCA uses orthogonal transformation to take transform variables in linearly uncorrelated variables called principal components (PC). These relationships are then shown by the magnitude and direction of eigenvectors on a 2D plot of the PC plotted against each other (Lever et al., 2017). A PCA simplifies the complexity, especially in large datasets, to extract overall trends to establish existing relationships in the data. Using the seasonal transformed data, results from the correlation matrix and PCA visualizations, a global model was developed using the “mgcv” package in R (Wood, 2006). A log transformation was used on the response variable of the model, CO₂ production to optimize the fit of the model. The global model was then dredged using the “MuMIn” package in R (Barton, 2019) following the same technique as used in Peters et al. (Peters et al., 2019). Using the results from the dredging and keeping in mind the original hypothesis, optimal models were created for the most significant predictors of CO₂ production by depth. The dredge function cannot fit a smoother by depth since it is limited by number of smoothers by the large number of terms already in the global model. By manually comparing models by AIC, we can optimize the model to be fitted by depth and be a better representation of the system it represents.

The number of smoothers fit to the data cannot exceed the degrees of freedom. Part of the model summary statistics determines whether k (the number of smoothers) is an over fit or under

fit for the data. It was determined that $k \geq 3$ for all the parameters within the model to limit under fitting, while including the maximum number of terms in the model equation. Given these limitations for k , only 4 terms could be included in the optimization modeling when looking at each term by depth. Within this manual dredge by depth, models were selected based on the differences in Akaike information criterion (AIC) by each model using the equation below. The AIC is a measure of the relative quality of statistical models against nested models within the dataset and is the backbone of the dredging function of the “MuMIn” dredging function.

$$\Delta i = AIC_i - AIC_{min} \quad \text{Equation 4.3}$$

Where AIC_i is the AIC for the i th model and AIC_{min} is the minimum of AIC for all model candidates. Models with $\Delta i > 10$ were not considered further as candidates for the optimal model. The optimal model is $\Delta i = \Delta_{min} = 0$ (Burnham and Anderson, 2003). AICc was used in place of AIC because of the sample size ($n < 100$) (Takezawa, 2014).

For the microbial component of the study (which included in the original data exploration and GAM modeling) the R “vegan” package was used to create species diversity and abundance indices from the Qiime 2.0 pipeline results (Oksanen et al., 2019). The FUNGuild open annotation was used to determine what guilds exists within the ITS results (Nguyen et al., 2016).

Table 4.1 Timeseries parameters from weekly sampling across 50 sampling locations from November 2018 to August 2019 at the Lyon Arboretum fieldsite.

Parameter	Sampling frequency	Method	Units
Mean CO ₂ produced	Weekly (time of sampling)	Gas wells	µmol m ⁻³ hr ⁻³
Mean volumetric water content (VWC)	Weekly (time of sampling)	SENTEK Diviner probe	%
Mean temperature	Weekly (time of sampling)	Thermistor	°C
Mean Δ temperature	Weekly (time of sampling)	Mean ambient temperature – mean temperature (for each id)	°C

Table 4.2 One time soil sampling parameters across 50 sampling locations sampled before heating began at fieldsite June 2018 at the Lyon Arboretum fieldsite.

Parameter	Method	Units
Carbon (C)	Elemental Analyzer	%
Nitrogen (N)	Elemental Analyzer	%
pH	Deionized water	NA
ΔpH	Deionized water method - KCl method	NA
Non crystalline minerals	$\text{Al}_H + 0.5\text{Fe}_H$ (Shoji et al., 1993)	mg kg^{-1} soil
Active Fe ratio	$\frac{\text{Fe}_H}{\text{Fe}_D}$ (Schwertmann, 1964)	NA
Organically complexed aluminum	Al_P (McKeague, 1967)	mg kg^{-1} soil
Organically complexed iron	Fe_P (McKeague, 1967)	mg kg^{-1} soil
Proportion of organo-aluminum complexes to non-crystalline aluminum oxides (andic horizon delineation)	$\frac{\text{Al}_P}{\text{Al}_H}$ (Shoji et al., 1993)	NA
Shannon Index (H)	$H = \sum p_i \ln p_i$	NA
Species richness (S) (Menhinick's index)	$S = s \sqrt{N}$	NA

4.4 RESULTS

4.4.1 Interactive effects of warming on CO₂ produced

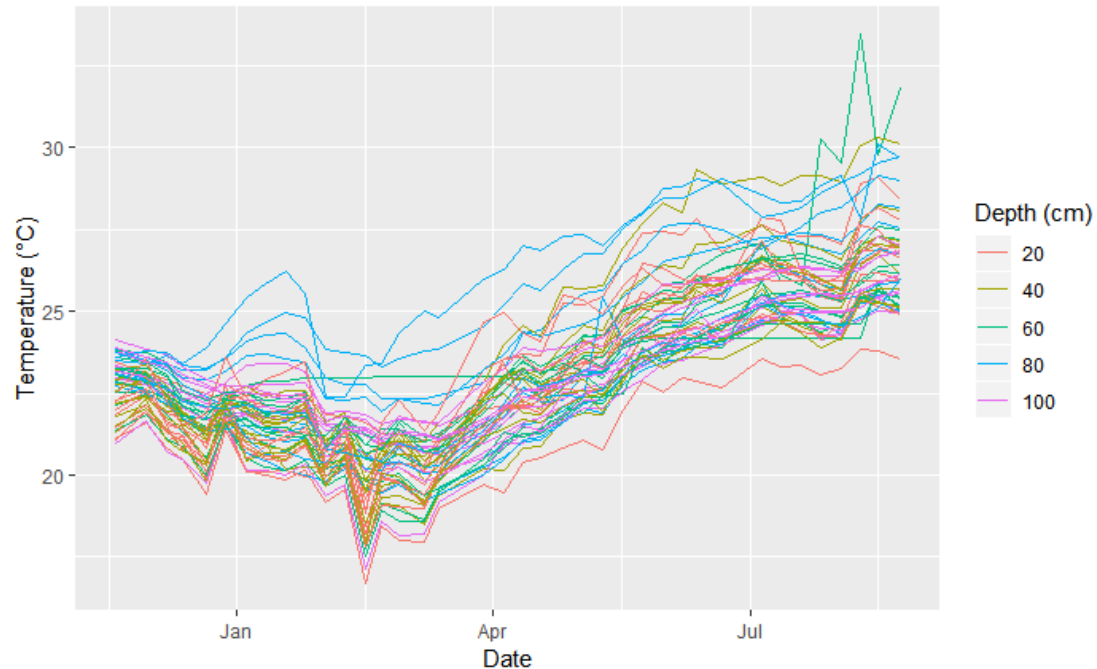


Figure 4.5 Soil temperature raw data timeseries at each depth across the fieldsite at the Lyon Arboretum from November 2018 to August 2019.

The soil temperature from November 2018 to August 2019 follows an expected seasonality curve (Figure 4.5). The soil temperature dips down in the winter months along with the air temperature and increases in the summer along with the air temperature. Based on proximity to the heating probes some depths experience a greater heating effect than others, therefore temperature distinction by depth is not apparent. An Augmented Dickey Fuller (ADF) test for stationarity at all sampling locations suggest that this trend is significant over time and a significant seasonal effect is present. This trend was also apparent in autocorrelation (ACF) plots of soil temperature at each sampling location over time. To account for the seasonality effect in the data a Fourier transformation was used to detect the seasonal signal and adjusted the data to remove the seasonal trend.

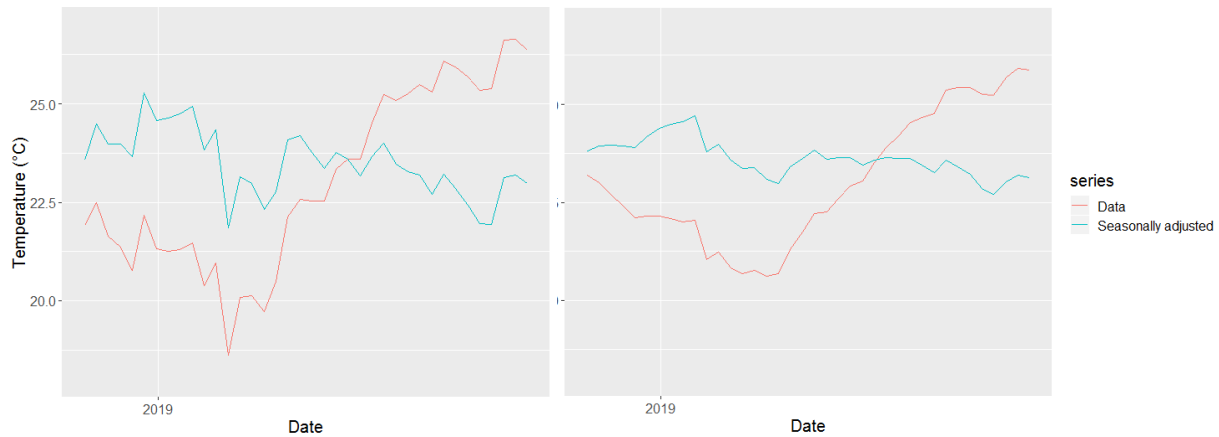


Figure 4.6 The seasonality of soil temperature at the fieldsite for 20cm (left) and 100cm (right) for the time period of soil sampling. Red is the raw data with seasonality and blue is the seasonally adjusted data used to eliminate bias in further analysis

There is a stronger effect of seasonality in soil temperature at 20cm than at 100cm, suggesting that shallower depths experience more seasonal variation. However, all depths experience the same trend of seasonality with cooler winter months and warmer summer months. The Fourier transformation in blue adjusts the data so the mean soil temperature can be used in further analysis without a strong seasonal bias.

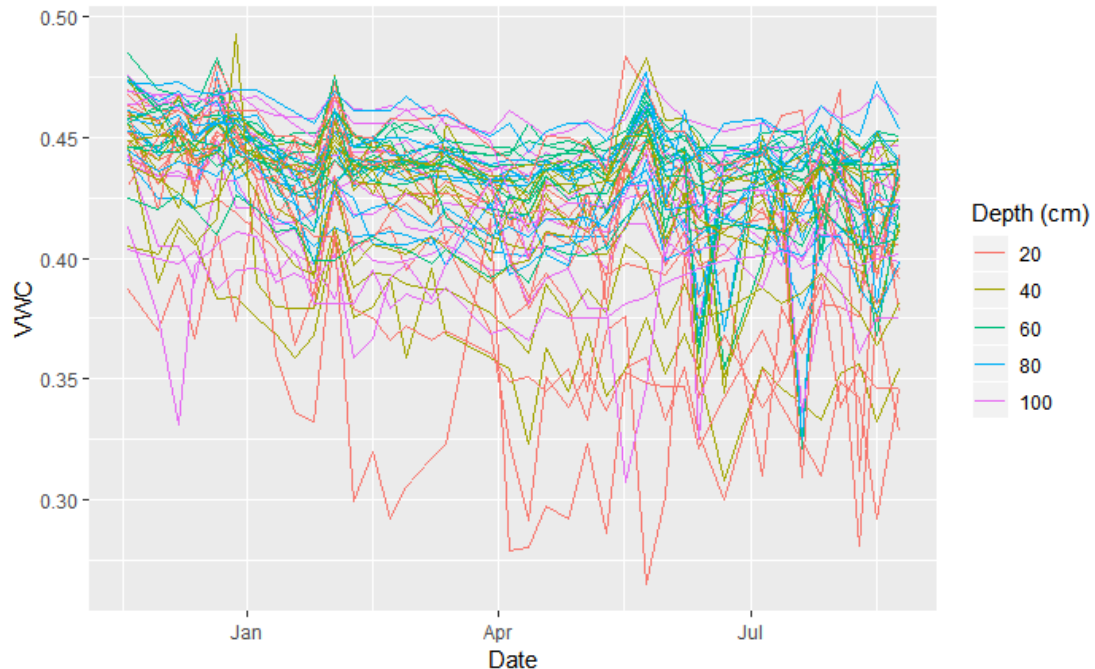


Figure 4.7 Volumetric water content (VWC) raw data timeseries at each depth across the fieldsite at the Lyon Arboretum from November 2018 to August 2019.

The volumetric water content as a measure of soil moisture has an overall trend of decreasing over time (Figure 4.7). This is consistent with the seasonal trends in precipitation for the study site with the winter months having greater precipitation and the summer months having less precipitation. Although the seasonality effect is less apparent than in soil temperature, an ADF test for stationarity at all sampling locations suggests that this trend is significant over time and a significant seasonal effect is present. This trend was also supported by ACF plots. To account for the seasonality effect in the data a Fourier transformation was used to detect the seasonal signal and adjusted the data to remove the seasonal trend.

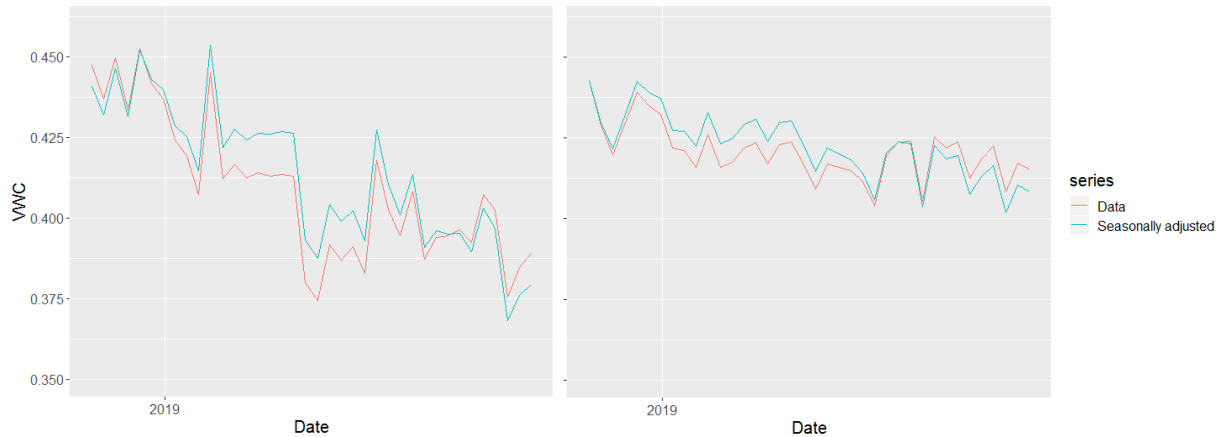


Figure 4.8 The seasonality of volumetric water content (VWC) at the fieldsite for 20cm (left) and 100cm (right) for the time period of soil sampling. Red is the raw data with seasonality and blue is the seasonally adjusted data used to eliminate bias in further analysis

There is a stronger effect of seasonality in soil moisture as determined by volumetric water content (VWC) at 20cm than at 100cm, suggesting that shallower depths experience more seasonal variation. However, all depths experience the same trend of seasonality with wetter winter months and drier summer months. The Fourier transformation in blue adjusts the data so the mean soil moisture (VWC) can be used in further analysis without a strong seasonal bias.

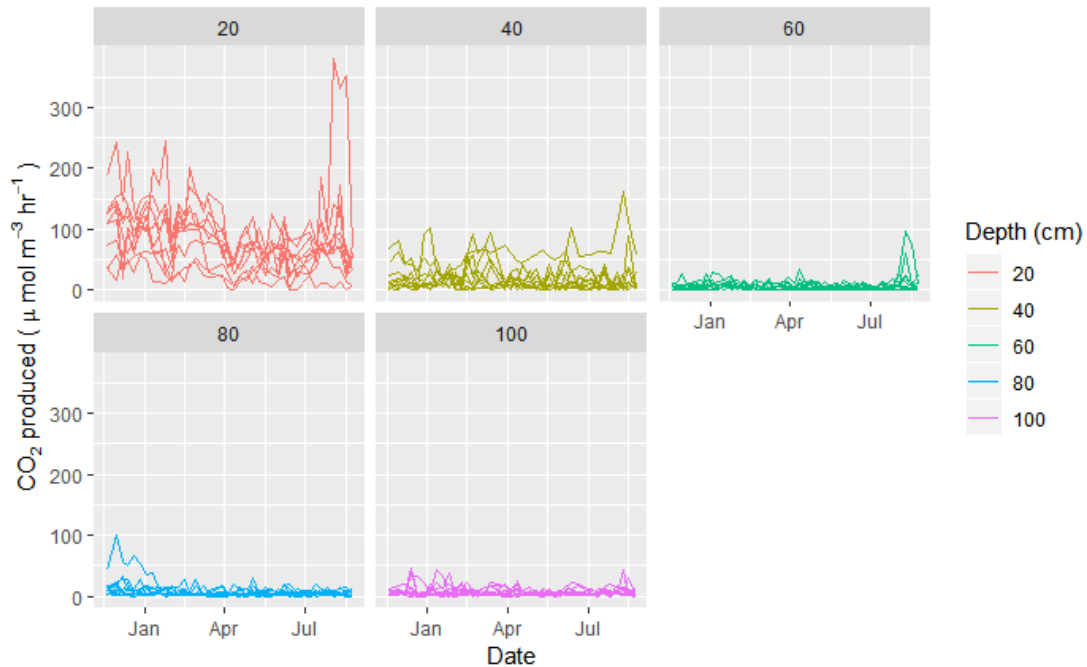


Figure 4.9 CO₂ produced by depth section for the raw data timeseries of the gas well sampling at the Lyon Arboretum from November 2018 to August 2019.

CO₂ produced by depth section shows the highest amount of CO₂ produced in the shallower soil at 20 and 40cm (Figure 4.9). The seasonal trend for CO₂ produced was tested for stationarity using an ADF test at each depth section. 20cm was the only depth section with a detected trend in seasonality. This trend was also supported by ACF plots at each sampling location. To account for the seasonality effect in the data a Fourier transformation was used to detect the seasonal signal and adjust the data to remove the seasonal trend at 20cm.

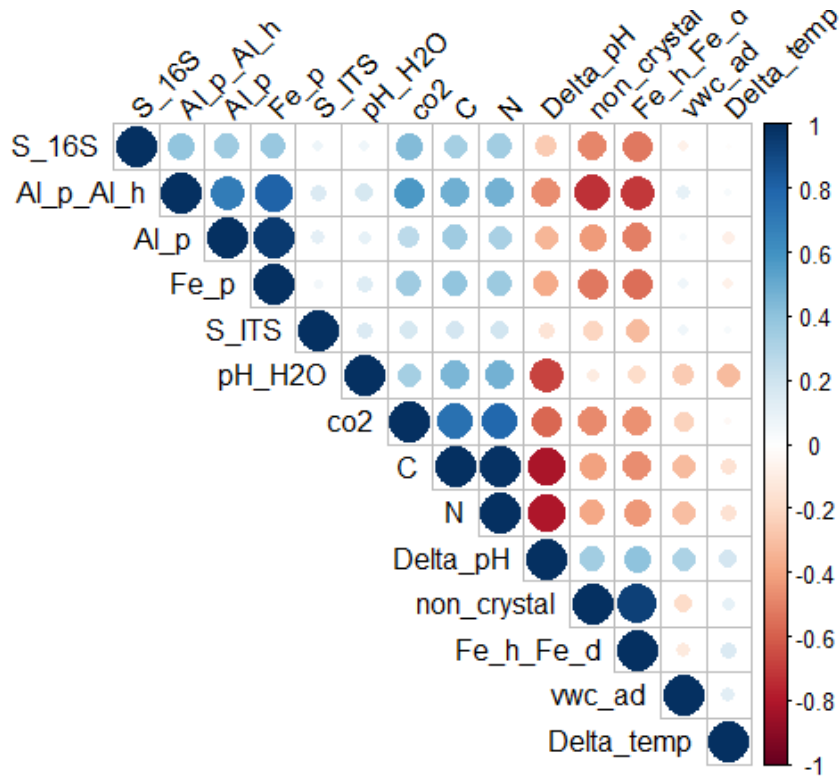


Figure 4.10 Correlation matrix for the mean seasonally adjusted timeseries parameters and initial soil sampling parameters at all depths from November 2018 to August 2019 at the Lyon Arboretum.. Dark blue shows a strong positive correlation while dark red shows a strong negative correlation (see scale on right)

There are several strong correlations evident from the correlation matrix. The strongest negative correlations are Δ pH with C, N, CO₂ produced and pH. Other strong negative correlation includes non-crystalline minerals and the active Fe ratio with C, N, CO₂ produced, OM complexed minerals and 16S abundance. There are strong positive correlations between C and N, CO₂ produced, OM complexed minerals and pH. Other strong positive correlations include pH and N and the active Fe ratio and Δ pH. Using a Principal Component Analysis (PCA) these correlations are tested further. For the correlation matrix and subsequent analysis, the Shannon's Diversity index was not used since more diversity does not technically equate to more CO₂ produced.

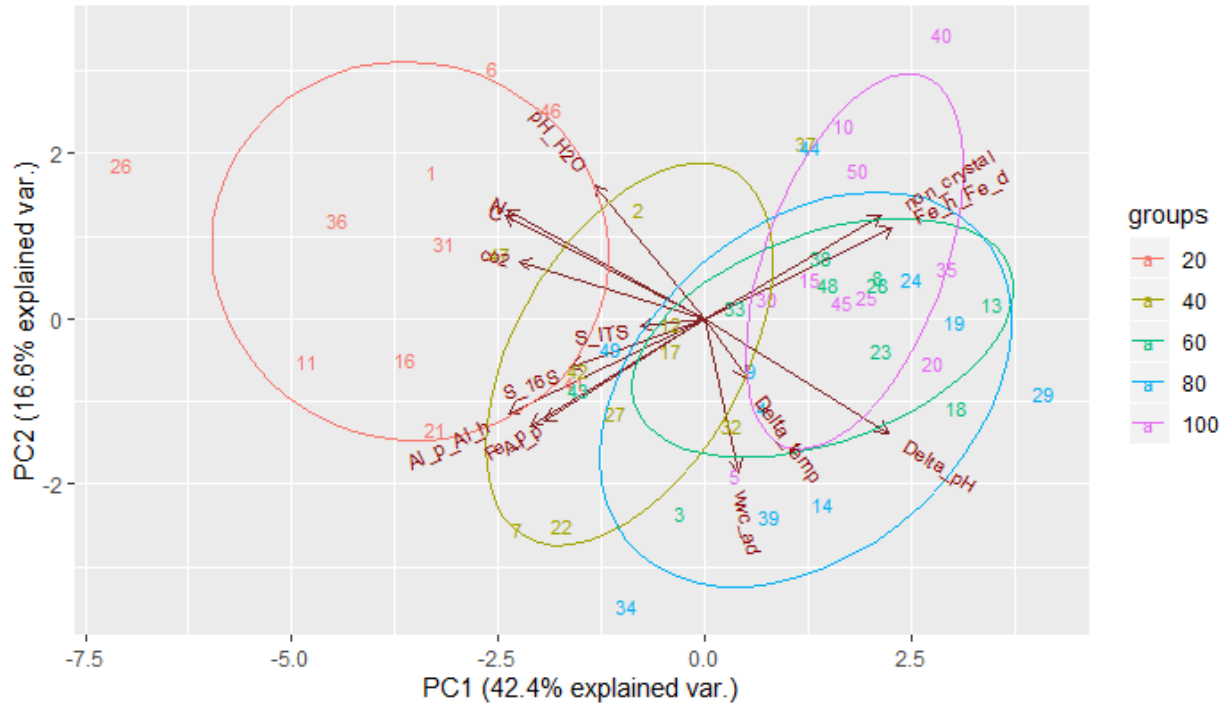


Figure 4.11 PCA of the parameters considered for model analysis, including the mean seasonally adjusted timeseries parameters and initial soil sampling parameters at all depths from November 2018 to August 2019 at the Lyon Arboretum.

The Principal Component Analysis (PCA) for the mean seasonally adjusted timeseries parameters and initial soil sampling parameters at all depths from November 2018 to August 2019 at the Lyon Arboretum explained 59% of the variance in the data within the first two principal components. There are several clear trends evident from the eigenvector's magnitude and direction as well as the grouping by depth. The first trend is that 20 and 40cm depth groupings are separated from the deep sampling depths of 60, 80 and 100cm, which are more overlapped. The eigenvectors for C, N, 16S abundance (S_16S), ITS abundance (S_ITs), pH, OM complexed minerals and mean CO₂ produced all point in the direction of 20 and 40cm. The eigenvectors for non-crystalline minerals, the active Fe ratio, Δ temperature, Δ pH and seasonally adjusted VWC are all pointed in the directions of 60, 80 and 100cm. Several eigenvectors overlap in magnitude and direction

suggesting a strong positive correlation. C, N and CO₂ produced are all similar in eigenvector magnitude and direction. In the opposite direction is the eigenvector of Δ pH suggesting a negative correlation. 16S abundance and ITS abundance eigenvectors also overlap in magnitude and direction, with OM complexed minerals. In the opposite direction are non-crystalline minerals and the active Fe ratio. The magnitude of the amorphous minerals eigenvectors is larger than the microbial abundance eigenvectors however there still could be a negative correlation given the opposite direction of the eigenvectors. Other notable trends include the perpendicular relationship of the eigenvectors of CO₂ produced and VWC suggesting no correlation between the parameters and a weak perpendicular relationship with CO₂ produced and Δ temperature.

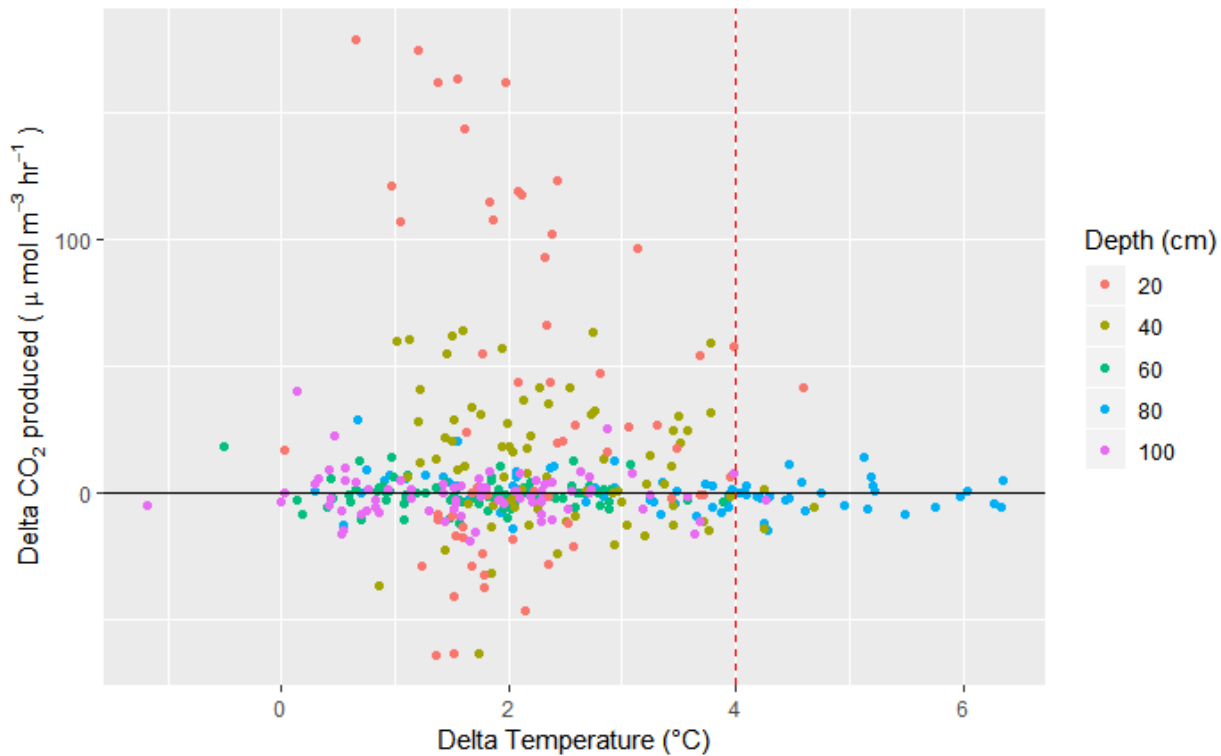


Figure 4.12 ΔCO₂ produced vs. Δ seasonally adjusted temperature over time at the highest and lowest 20% of temperature ranges at all depths from November 2018 to August 2019 at the Lyon Arboretum. Red dashed line at the target Δ temp of 4°C from soil heating.

The ΔCO_2 produced against the Δ seasonally adjusted soil temperature varies in spread across the sampling depths for the highest and lowest 20% of soil temperature ranges (Figure 4.12). 20cm has the greatest spread in both the y and x axis, followed by 40cm. For the sampling depths 60, 80, and 100cm there is little spread in the y axis but definite spread in the x axis. This suggests that as Δ seasonally adjusted soil temperature changes there is little response from ΔCO_2 produced.

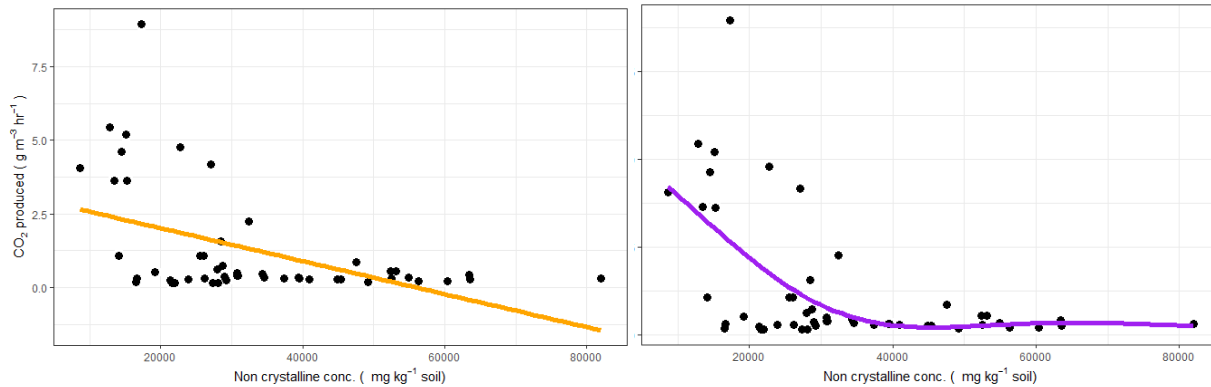


Figure 4.13 CO_2 produced plotted against non-crystalline concentration for the 50 soil sampling locations across depths. Orange is a generalized linear model trend whereas purple is the trend fit with a GAM smoother.

Before modeling the entire dataset, it was important to provide evidence for GAM modeling as opposed to traditional linear modeling. Figure 4.13 illustrates the non-linear relationships in the data that are better suited with a GAM smoother opposed to a linear smoother. Figure 4.14 and Figure 4.15 are select examples of other nonlinear relationships within the data fit with a GAM smoother. Looking at these relationships are important for interpreting the global model and how the smoothers are added up as predictors of CO_2 produced.

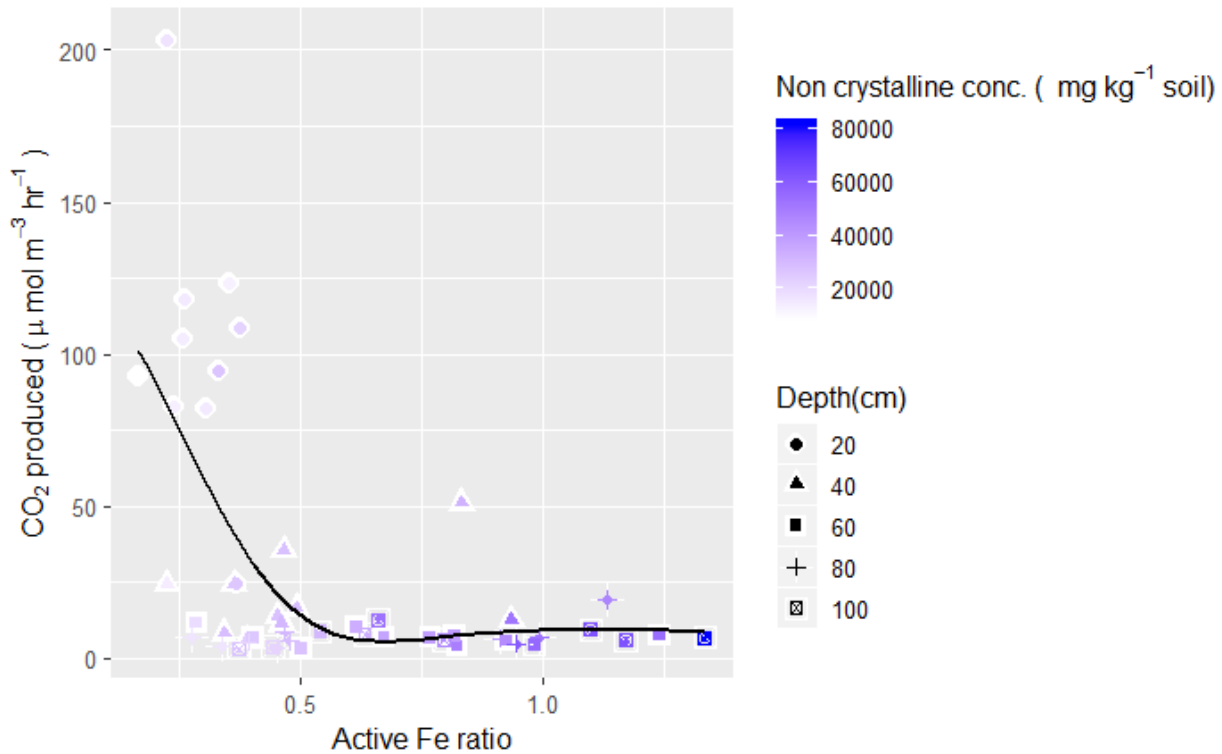


Figure 4.14 Mean CO₂ produced against the active Fe ratio (Fe_H/Fe_D) with a GAM smoother ($k=4$) fitted across all depths from November 2018 to August 2019 at the Lyon Arboretum. The colors are the non-crystalline mineral concentration and the shapes are the depths.

In Figure 4.14, there is a nonlinear relationship between CO₂ produced and the active Fe ratio. There is an inflection point around active Fe ratio = 0.5 where a steep negative slope of the variable of CO₂ produced out and stays relatively flat, suggesting that as the active Fe ratio increases, CO₂ produced decreases. Along with this, the CO₂ produced decreases as non-crystalline minerals increase as shown by the colors of the points. There are also some trends across sampling depths with 20cm being separate from 40, 60, 80 and 100cm in terms of CO₂ produced plotted against the active Fe ratio.

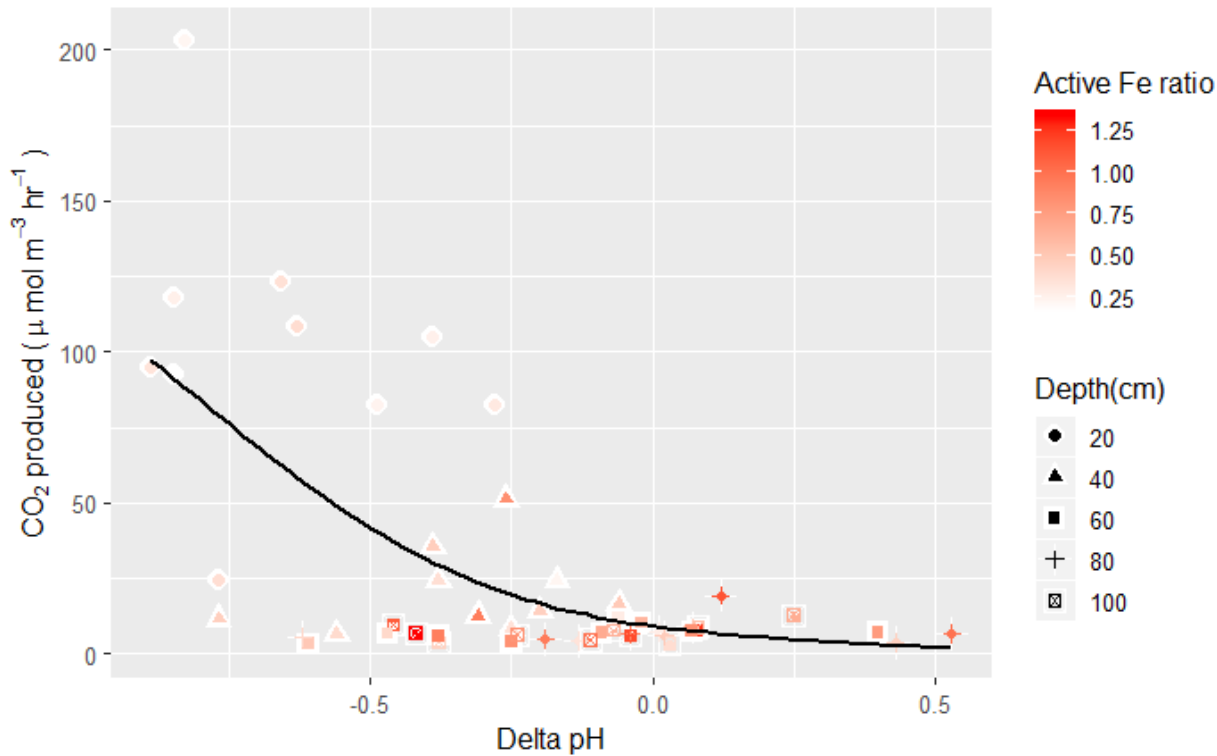


Figure 4.15 Mean CO₂ produced against Δ pH with a GAM smoother ($k=4$) fitted across all depths from November 2018 to August 2019 at the Lyon Arboretum. The colors are the active Fe ratio and the shapes are the depths.

In Figure 4.15 there is a nonlinear relationship between CO₂ produced and ΔpH. There is an inflection point around ΔpH = 0 where the negative slope of CO₂ produced levels out and stays relatively consistent, suggesting that as ΔpH increases CO₂ produced decreases. Along with this, the CO₂ produced decreases as the active Fe ratio increases as shown by the colors of the points. Along with this there are also some trends across depth with 20cm being separate from 40, 60, 80 and 100cm in terms of CO₂ produced plotted against the active Fe ratio. After exploring these relationships to validate the use of GAM, a global model was developed to begin to select the most significant predictors of CO₂ produced.

Global Model Formula:

$$\log(\text{co2}) \sim s(\text{vwc_ad}, k=4) + s(\text{Delta_temp}, k=4) + s(\text{C}, k=4) + s(\text{N}, k=4) + s(\text{pH_H2O}, k=4) + s(\text{Delta_pH}, k=4) + s(\text{non_crystal}, k=4) + s(\text{Fe_h_Fe_d}, k=4) + s(\text{Al_p_Al_h}, k=4) + s(\text{Al_p}, k=4) + s(\text{Fe_p}, k=4) + s(\text{S_16S}, k=4) + s(\text{S_ITS}, k=4) + s(\text{depth}, k=4) + s(\text{id}, \text{bs} = "re") + 1$$

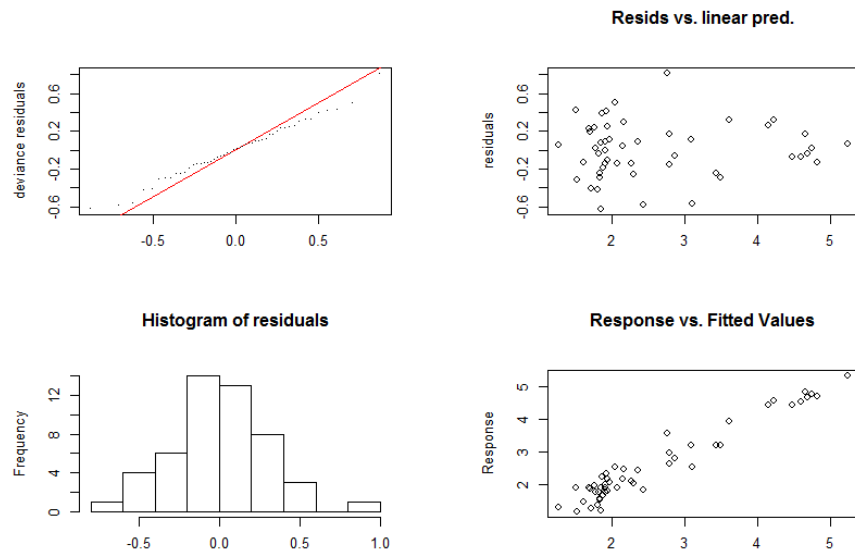


Figure 4.16 Quality check plots for global model of $\log(\text{CO}_2)$ response as predicted by delta temperature, VWC and relevant soil properties by depth with sampling locations as a random effect for mean data from November 2018 to August 2019 at the Lyon Arboretum fieldsite. ($R^2 = 0.885$, Deviance explained = 92.4%, $n = 50$.)

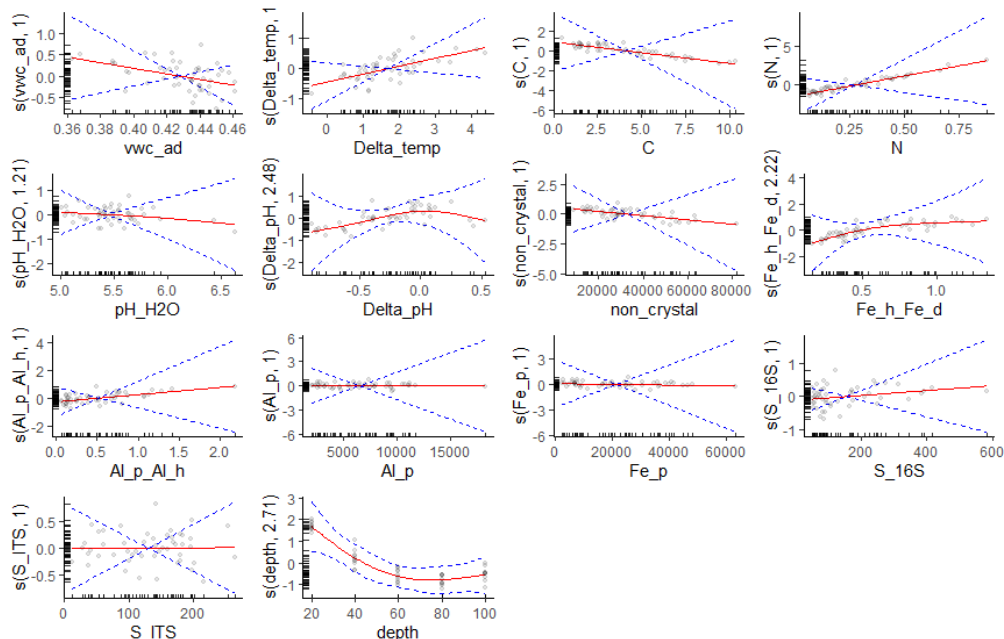


Figure 4.17 Smoothers fit for each parameter of the global model individually for mean data from November 2018 to August 2019 at the Lyon Arboretum fieldsite ($k = 4$)

The global model explained 92.4% of the model's deviance. All parameters included in the exploratory PCA were included in the global model. Within the model summary only select parameters were statistically significant. These parameters were Δ temperature ($P = 0.02 * 10^{-01}$, $k = 4$), Δ pH ($P = 0.02$, $k = 4$), N ($P = 0.04$, $k = 4$), depth ($P = 1.27 * 10^{-08}$, $k = 4$), and non-crystalline minerals ($P = 0.05$, $k = 4$, only slightly significant). The global model also was a good fit for all included parameters as predicting log transformed CO₂ produced as shown by the quality check plots (Figure 4.16). The QQ plot showed little evidence for outliers with a strong straight line across the datapoints. The histogram of the residuals displayed normal distribution. The residuals vs. the linear predictor showed a cloud of points with little clustering. The response vs. the fitted values displayed a linear relationship. Within the GAM check plots, the value chosen for k was also validated in the smoother fit test for over or under fitting. The smoother test tests the k selected for each parameter and by the p-values. The null hypothesis that k is a good fit for smoothing the data was supported. The validation of the global model was important for the next step of dredging the model shown in Figure 4.18.

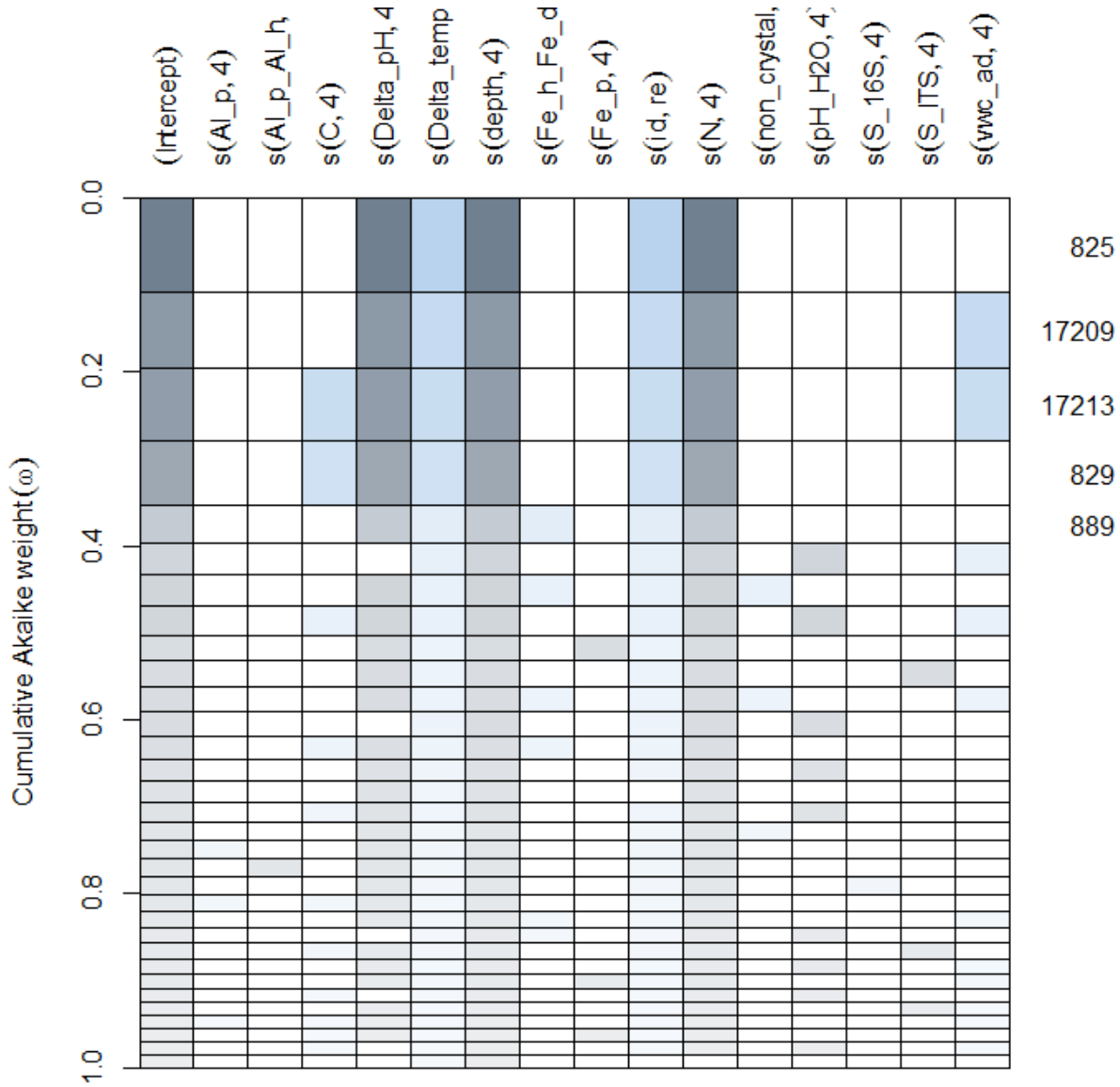


Figure 4.18 Results of global model dredge using “MuMin” package in R. Darker terms are more significant predictors for optimal model. Akaike information criterion (AIC) as a measure of model fit are the y axis.

The dredging of the global model using the “MuMin” package in R showed Δ temperature, Δ pH and N as the most significant predictors of log transformed CO₂ (**Figure 4.18**). The second most statistically significant predictors of log transformed CO₂ were Δ temperature, Δ pH, N and

soil moisture (VWC). Next, we tried different iterations of the global model dredging to optimize the fit of the model and the deviance explained. For tighter optimization each smoother was fit “by = depth” since we expect different depths to behave differently in terms of CO₂ produced, which is highly supported by the literature. Model iterations were based off the top ten models output by the “dredge” function (top 10 lines in Figure 4.18).

Table 4.3 Table of the top ten model iterations from the global model dredging including terms used, AIC score and model deviance explained.

Model name	Variables	AICc	Deviance explained (%)	Removed for smoother
Dredge 1	Δ temperature, Δ pH, N	127.01	88.5	
Dredge 2	Δ temperature, Δ pH, N, VWC	172.47	91.5	
Dredge 3	Δ temperature, Δ pH, C, VWC	171.04	91.7	N
Dredge 4	Δ temperature, Δ pH, N,C	158.31	93.3	
Dredge 5	Δ temperature, Δ pH, N, Active Fe ratio	175.12	96.8	
Dredge 6	Δ temperature, N, pH, VWC	151.32	92.1	
Dredge 7	Δ temperature, Δ pH, N, non-crystalline minerals, Active Fe ratio	156.73	95.9	Active Fe ratio
Dredge 8	Δ temperature, Δ pH, pH, VWC	163.85	91.9	N, C
Dredge 9	Δ temperature, Δ pH, Fe _p	127.75	90.5	
Dredge 10	Δ temperature, Δ pH, N, S_ITC	152.51	94.1	

All but one of the top ten models within the dredge found Δ temperature and Δ pH as the most significant predictors of log CO₂ produced. The model with the best fit, after model optimization by depth as a factor, was “Dredge 1”, which was the best model selected by the “MuMIn” package. This model explained 88.5% of the model deviance with an R² = 0.81. The parameters that were statistically significant by depth were Δ pH at 20cm (P=7.91 *10⁻⁰³, k =3), and N at 20cm (P = 0.04, k =4). The model that explained the most deviance (96.8%) was “Dredge 5” which included Δ temperature, Δ pH, N, and the active Fe ratio, however the AICc score and

QQ-plot suggest that the model is a poor fit for the data. The results from the smoother suggest that further optimization could be established by manual model selection. The issue is that the dredge function cannot fit a smoother by depth since it is limited by number of smoothers by the large number of terms already in the global model. By manually comparing models by AIC, we can optimize the model to be fitted by depth and be a better representation of the system it represents.

The number of smoothers fit to the data cannot exceed the degrees of freedom. Part of the model summary statistics determines whether k (the number of smoothers) is an over fit or under fit for the data. It was determined that $k \geq 3$ for all the parameters within the model to limit under fitting, while including the maximum number of terms in the model equation. Given these limitations for k , only 4 terms could be included in the optimization modeling when looking at each term by depth. Given the results of the global model dredging, Δ temperature and Δ pH are two known terms for the optimal model for the data. This leaves space for two more terms to optimize the fit of the model while increasing the model deviance explained.

Using the results of the model dredging N, VWC, C, active Fe ratio, non-crystalline minerals, pH and OM complexed Fe were the next most important terms to be included into the model given the amount of deviance explained. ITS abundance for “Dredge 10” is not included as a term for optimization because in the deeper depths (>60cm) there are many null values as a result of the sequencing runs. Therefore, it was decided to omit ITS abundance since the significance could be heavily bias by this lack of data. The 11th best model to replace “Dredge 10” includes non-crystalline minerals, Active Fe ratio and VWC, which are already within the top ten dredge results to be considered for optimization.

A second model optimization looking to improve the AICc score while increasing the deviance explained was fit using Δ temperature and Δ pH as the model base and different iterations of N, VWC, C, active Fe ratio, non-crystalline minerals, pH and OM complexed Fe as the other two model terms. Some of the optimization models were models already dredged from the “MuMIn” package and therefore were included in as such.

Table 4.4 Table of the model iterations using the strongest terms from the global model dredging including terms used, AIC score and model deviance explained. Highlighted models are where $\Delta i < 10$ from equation 4.3 for optimal model candidate selection.

Model name	Variables	AICc	Deviance explained (%)
<i>Optimize 1</i>	Δ temperature, Δ pH, N, non-crystalline minerals	156.73	95.9
<i>Optimize 2</i>	Δ temperature, Δ pH, C, non-crystalline minerals	155.91	95.5
<i>Optimize 3</i>	Δ temperature, Δ pH, VWC, non-crystalline minerals	178.02	97.5
<i>Optimize 4</i>	Δ temperature, Δ pH, pH, non-crystalline minerals	161.12	95.8
<i>Optimize 5</i>	Δ temperature, Δ pH, non-crystalline minerals	122.55	94.6
<i>Optimize 6 (Dredge 5)</i>	Δ temperature, Δ pH, N, Active Fe ratio	175.12	96.8
<i>Optimize 7</i>	Δ temperature, Δ pH, C, Active Fe ratio	166.14	97.1
<i>Optimize 8</i>	Δ temperature, Δ pH, VWC, Active Fe ratio	167.63	96.4
<i>Optimize 9</i>	Δ temperature, Δ pH, pH, Active Fe ratio	175.10	96.8
<i>Optimize 10</i>	Δ temperature, Δ pH, Active Fe ratio	115.90	95.7
<i>Optimize 11</i>	Δ temperature, Δ pH, N, OM complexed Fe	176.31	93.0
<i>Optimize 12</i>	Δ temperature, Δ pH, C, OM complexed Fe	178.59	93.5
<i>Optimize 13</i>	Δ temperature, Δ pH, VWC, OM complexed Fe	176.75	93.8
<i>Optimize 14</i>	Δ temperature, Δ pH, pH, OM complexed Fe	150.10	92.2
<i>Optimize 15</i>	Δ temperature, Δ pH, OM complexed Fe	127.75	90.5
<i>Optimize 16 (Dredge 2)</i>	Δ temperature, Δ pH, N, VWC	172.47	91.5

Model name	Variables	AICc	Deviance explained (%)
<i>Optimize 17 (Dredge 4)</i>	Δ temperature, Δ pH, N,C	158.31	93.3
<i>Optimize 18</i>	Δ temperature, Δ pH, N,pH	156.23	92.0
<i>Optimize 19 (Dredge 1)</i>	Δ temperature, Δ pH, N	127.01	88.5
<i>Optimize 20 (Dredge 3)</i>	Δ temperature, Δ pH, C, VWC	171.04	91.7
<i>Optimize 21</i>	Δ temperature, Δ pH, C, pH	154.78	92.1
<i>Optimize 22</i>	Δ temperature, Δ pH, C	122.03	91.5
<i>Optimize 23 (Dredge 8)</i>	Δ temperature, Δ pH, pH, VWC	163.85	91.9
<i>Optimize 24</i>	Δ temperature, Δ pH, VWC	132.80	89.0
<i>Optimize 25</i>	Δ temperature, Δ pH, pH	125.40	89.4
<i>Optimize 26</i>	Δ temperature, Δ pH, non-crystalline minerals, Active Fe ratio	166.91	
<i>Optimize 27</i>	Δ temperature, Δ pH, non-crystalline minerals, OM complexed Fe	188.66	
<i>Optimize 28</i>	Δ temperature, Δ pH, Active Fe ratio, OM complexed Fe	171.10	

There were four models where $\Delta i < 10$ from equation 4.3 for optimal model candidate selection. The four best fits for the optimization models all included Δ temperature, Δ pH, measures of non-crystalline minerals, C and pH. The best fit model was Δ temperature, Δ pH and the active Fe ratio ($AICc = 115.90$, $R^2 = 0.92$, $n= 50$) with 95.7% of the model deviance explained. The second-best fit model was Δ temperature, Δ pH and carbon ($AICc = 122.01$, $R^2 = 0.86$, $n= 50$) with 91.5% of the model deviance explained. The third-best fit model was Δ temperature, Δ pH and non-crystalline minerals ($AICc = 122.55$, $R^2 = 0.89$, $n= 50$) with 94.6% of the model deviance explained. The fourth-best fit model was Δ temperature, Δ pH and pH ($AICc = 125.40$, $R^2 = 0.83$, $n= 50$) with 89.4% of the model deviance explained. The quality check plots of the top four models from model optimization are included in Appendix C.

The parameters that were statistically significant by depth in the best model “Optimize 10” were Δ temperature at 20cm ($P= 4.87 *10^{-03}$, $k = 3$) and Δ pH at 40cm ($P = 5.91 *10^{-06}$, $k = 3$) and 60cm ($P= 0.04$, $k = 3$) and the active Fe ratio at 20cm ($P=3.92 *10^{-09}$, $k = 3$), 40cm ($P=9.46 *10^{-09}$,

05 , $k = 3$) and 100cm ($P = 0.04$, $k = 3$). The parameters that were statistically significant by depth in the second best model, model “Optimize 22”, were Δ temperature at 20cm ($P = 2.29 * 10^{-2}$, $k = 3$), Δ pH at 40cm ($P = 4.01 * 10^{-3}$, $k = 3$) and carbon at 20cm ($P = 8.24 * 10^{-6}$, $k = 3$) and 40cm ($P = 0.04$, $k = 3$). The parameters that were statistically significant by depth in the third best model, model “Optimize 5”, were Δ temperature at 20cm ($P = 0.02$, $k = 3$) and 40cm ($P = 1.81 * 10^{-3}$, $k = 3$), and Δ pH at 40cm ($P = 5.07 * 10^{-3}$, $k = 3$) and 60cm ($P = 0.04$, $k = 3$) and non-crystalline minerals at 20cm ($P = 3.00 * 10^{-8}$, $k = 3$) and 40cm ($P = 5.46 * 10^{-4}$, $k = 3$). Lastly, the parameters that were statistically significant by depth in the fourth best model, model “Optimize 25”, were Δ temperature at 20cm ($P = 0.02$, $k = 3$) and Δ pH at 20cm ($P = 1.16 * 10^{-13}$, $k = 3$) and pH at 40cm ($P = 0.02$, $k = 3$). Because the fourth best model $\Delta i \approx 10$ it was dropped from further discussion since it was deemed a weak fit for the data.

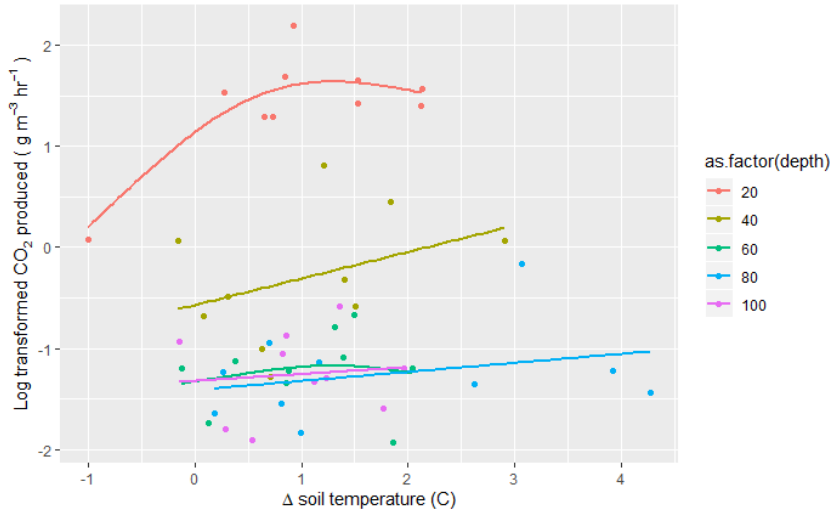


Figure 4.19 Log-transformed CO_2 produced plotted against Δ soil temperature factored by depth (20, 40, 60, 80, 100cm). Only the top 20cm presented carbon as a significant predictor of log-transformed CO_2 produced (20cm: $P = 0.02$) (factor in all models)

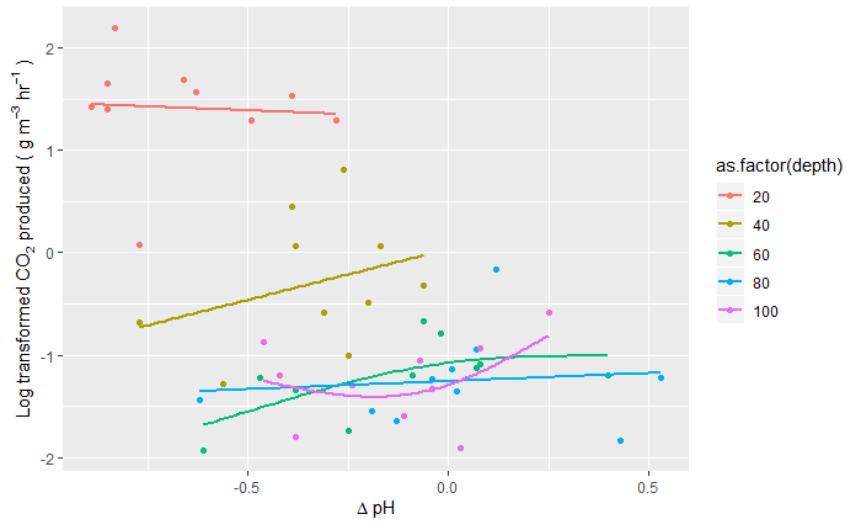


Figure 4.20 Log-transformed CO₂ produced plotted against Δ pH factored by depth (20, 40, 60, 80, 100cm). Only the top 40cm presented carbon as a significant predictor of log-transformed CO₂ produced (20cm: P = >2*10⁻¹⁶, 40cm: P = 1.04*10⁻⁰⁴) (factor in all models)

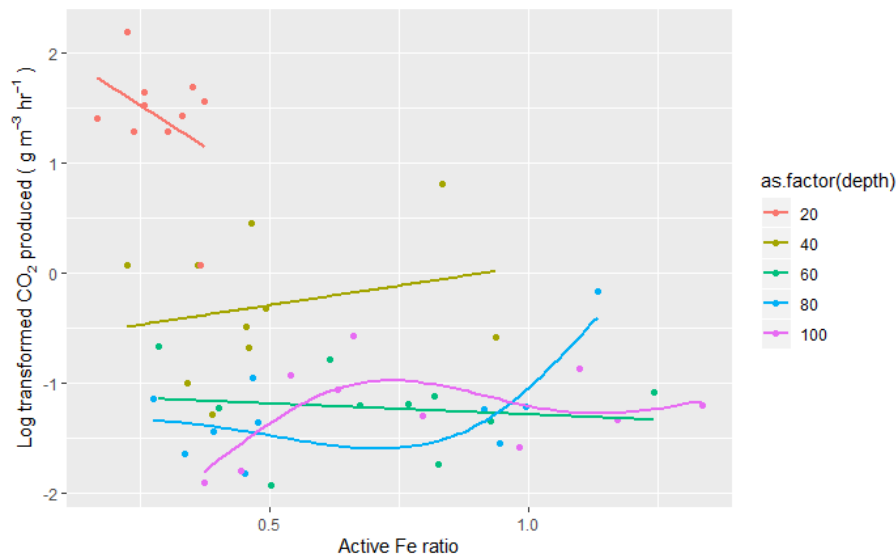


Figure 4.21 Log-transformed CO₂ produced plotted against Active Fe ratio factored by depth (20, 40, 60, 80, 100cm). Only the top 40cm presented carbon as a significant predictor of log-transformed CO₂ produced (20cm: P = 3.92*10⁻⁰⁹, 40cm: P = 9.46*10⁻⁰⁵) (factor in best model)

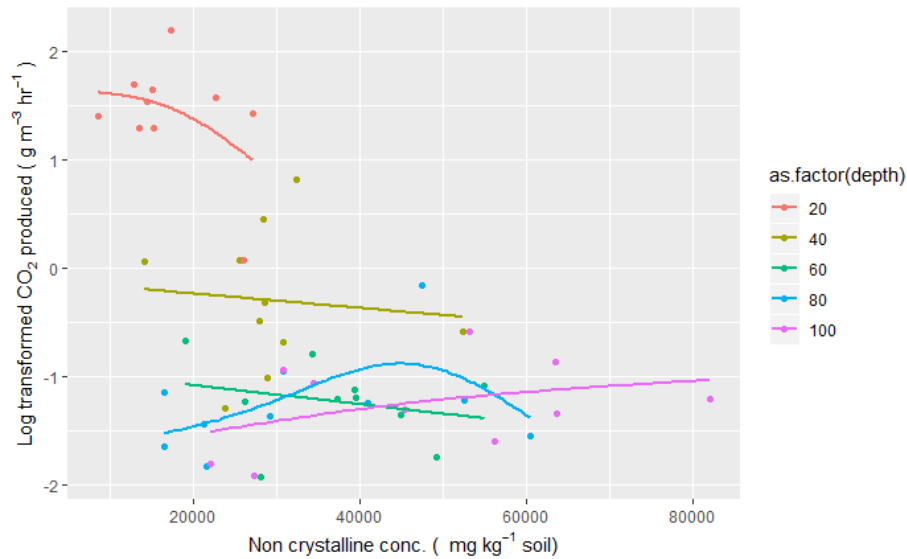


Figure 4.22 Log-transformed CO₂ produced plotted against non-crystalline mineral concentration factored by depth (20, 40, 60, 80, 100cm). Only the top 40cm presented carbon as a significant predictor of log-transformed CO₂ produced (20cm: $P = 3.00 \times 10^{-8}$, 40cm: $P = 5.46 \times 10^{-4}$) (factor in second best model)

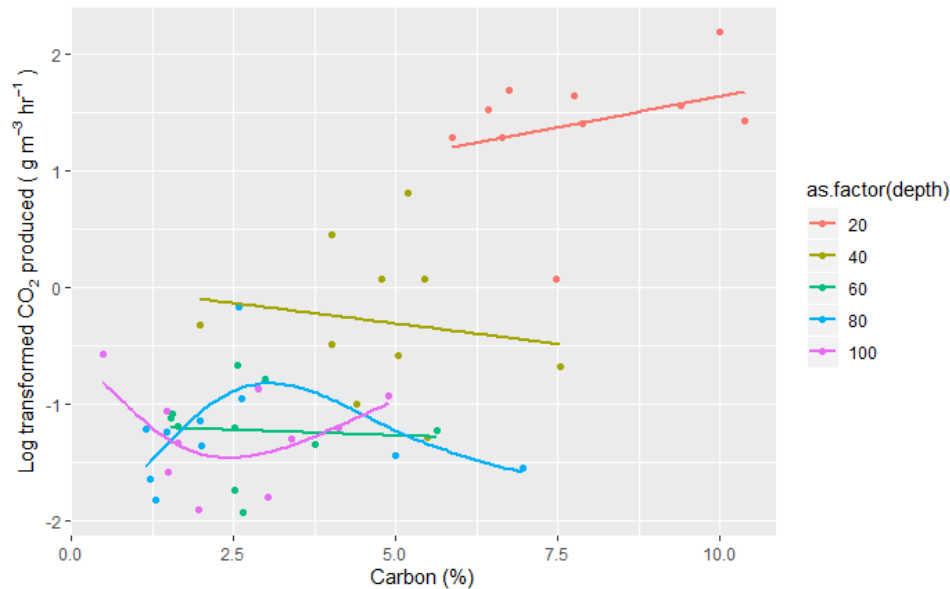


Figure 4.23 Log-transformed CO₂ produced plotted against carbon (C%) factored by depth (20, 40, 60, 80, 100cm). Only the top 40cm presented carbon as a significant predictor of log-transformed CO₂ produced (20cm: $P = 8.24 \times 10^{-6}$, 40cm: $P = 0.04$) (factor in third best model)

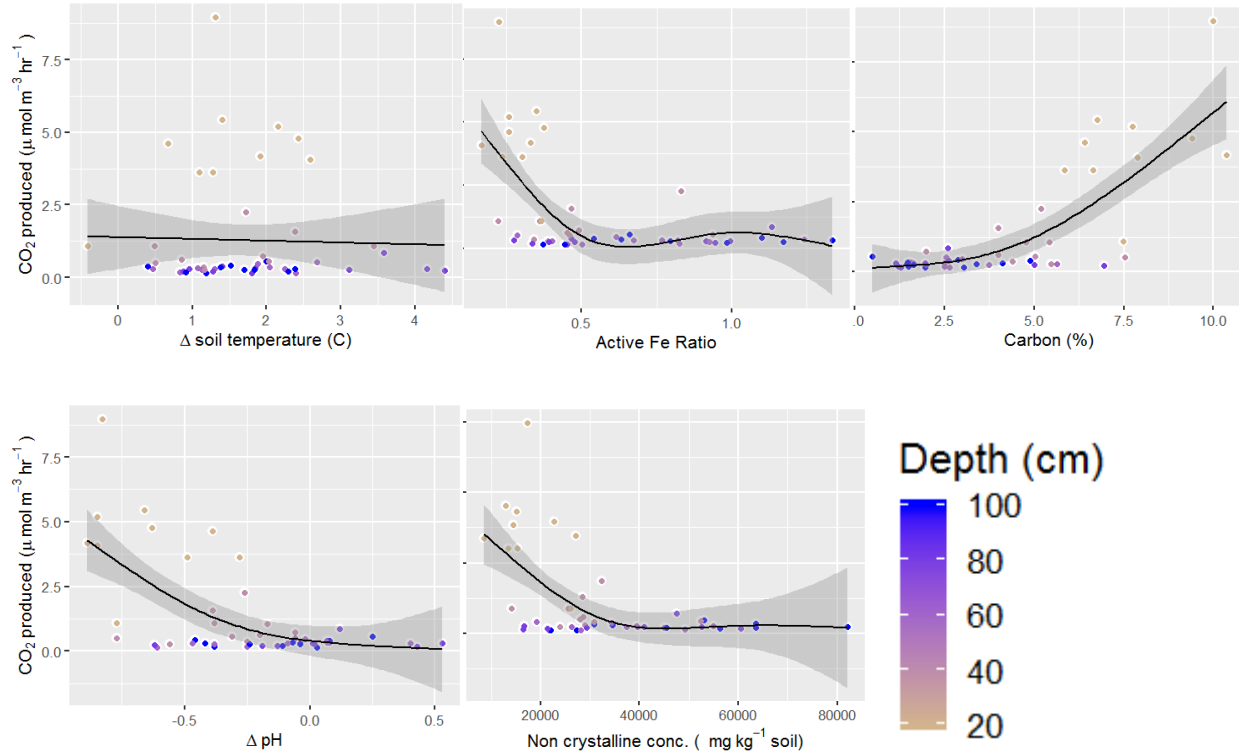


Figure 4.24 CO₂ produced plotted against the top predictors of CO₂ produced at the fieldsite for the mean values for the timeseries sampling from November 2018 to August 2019 at the Lyon Arboretum. The top left is Δ soil temperature, top middle Active Fe ratio, top right %C, bottom left Δ pH and bottom middle non-crystalline minerals all plotted across all depths.

There is clearly a depth separation shown by the modeling of the most important predictors of CO₂ by depth shown by Figures 4.19 to Figure 4.23. However to put the parameters into context Figure 4.24 shows the trend across depths. For Δ soil temperature, 20cm had a response to changing temperatures while all other depths did not. This means that heating depths 40cm there was no response from CO₂ produced. For Δ pH up to 40cm there is a response of CO₂ produced, but as Δ pH increases the net charge of the soil colloids go from negative to positive and there is little to no response of CO₂ produced. The Active Fe ratio shows an inflection point at 0.5, as you go towards more non crystalline soil, with a lack of CO₂ response. Similarly as non-crystalline

content increases the amount of CO₂ produced decreases to little to no response. Finally, as carbon increases the CO₂ response increases in the study soil.

4.4.2 Microbial depth dependence

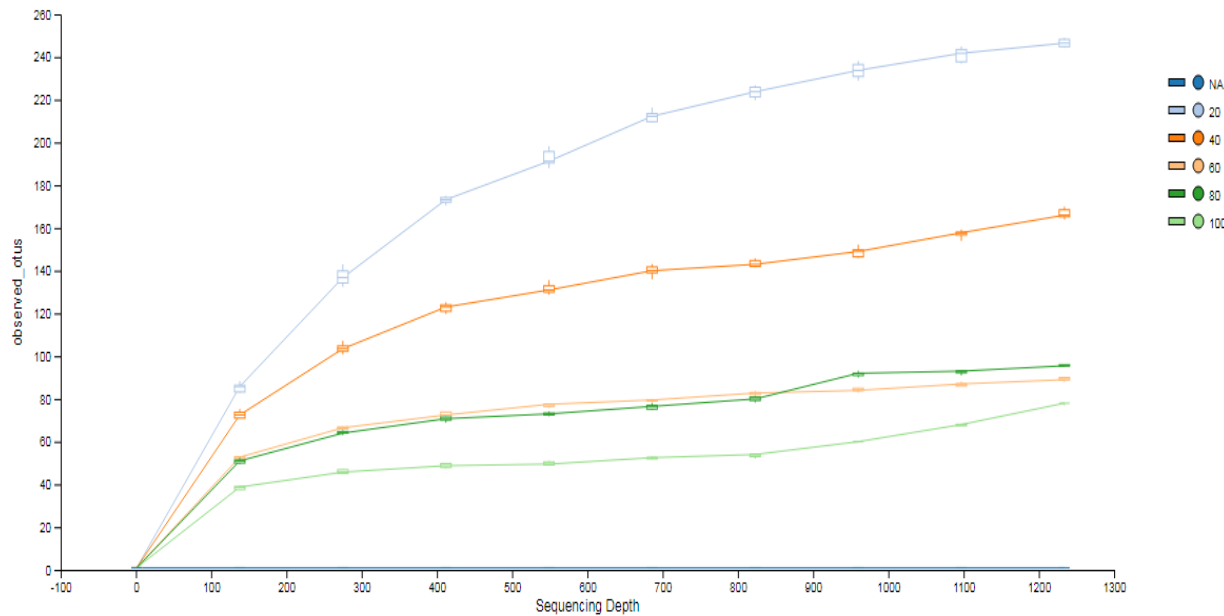


Figure 4.25 Alpha rarefaction curve for observed taxonomic units (OTUs) by depth for 16S (bacteria) sampling from the initial soil sampling at the Lyon Arboretum fieldsite generated by Qiime 2.0. The lines represent the different depths and the dots are the levels of samples.

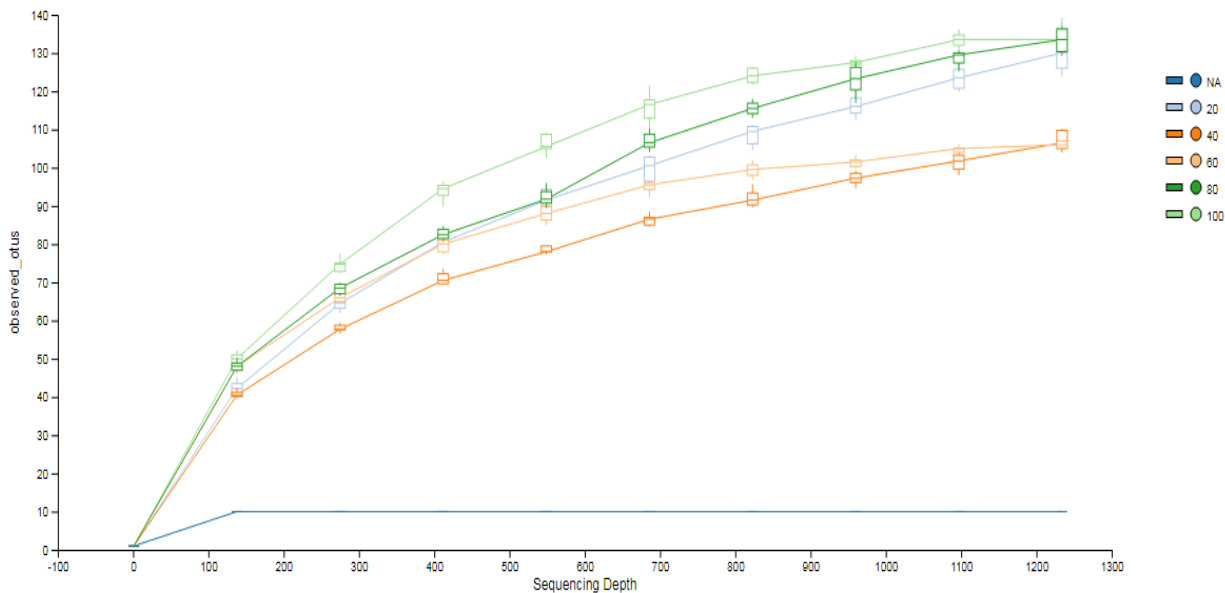


Figure 4.26 Alpha rarefaction curve for observed taxonomic units (OTUs) by depth for ITS (fungi) sampling from the initial soil sampling at the Lyon Arboretum fieldsite generated by Qiime 2.0. The lines represent the different depths and the dots are the levels of samples.

The leveling off seen in both alpha rarefaction curves as sequencing depth increases for both ITS and 16S, suggests that sampling is nearly saturated with an accurate representation of species sampled by the study. The alpha rarefaction for 16S (Figure 4.25) was more saturated than the ITS alpha rarefaction curve (Figure 4.26) given the slope of the line at higher sequencing depths.

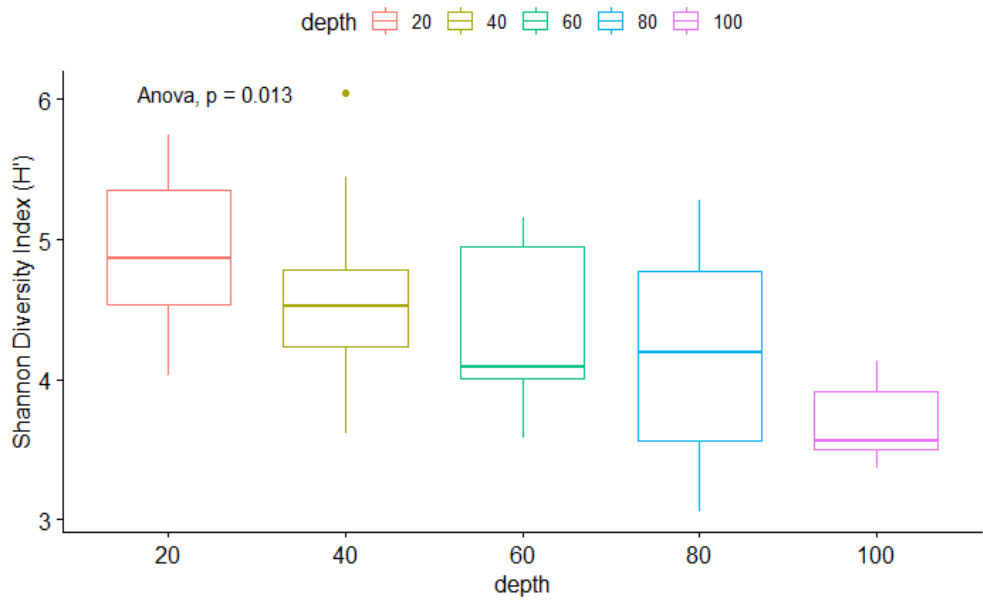


Figure 4.27 Boxplot of Shannon Diversity Index (H') for 16S (bacteria) data, with ANOVA between depth groups ($\alpha = 0.05$) from the initial soil sampling at the Lyon Arboretum fieldsite.

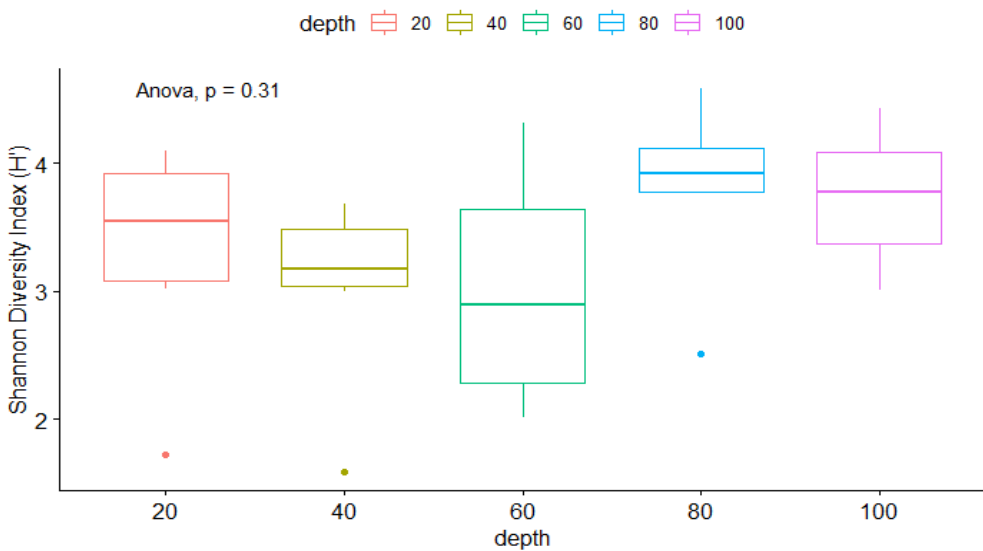


Figure 4.28 Boxplot of Shannon Diversity Index (H') for ITS (fungi) data, with ANOVA between depth groups ($\alpha = 0.05$) from the initial soil sampling at the Lyon Arboretum fieldsite.

The highest Shannon Diversity Index was at 20cm and decreased with increasing depth for the 16S data (Figure 4.27). For the ITS data, the Shannon Diversity Index distributions varied (Figure 4.28). The highest diversity of fungi was found at 80 and 100cm, followed by 20cm and 40cm. 60cm has the lowest Shannon Diversity Index. The results from the ANOVA test for differences between group means suggests that there were significant differences between depths for the 16S data and not for the ITS data. A post-hoc Tukey pairwise comparisons test from the 16S data found that the only significantly different Shannon Diversity Index was at 20cm when compared to 100cm ($P = 0.01$).

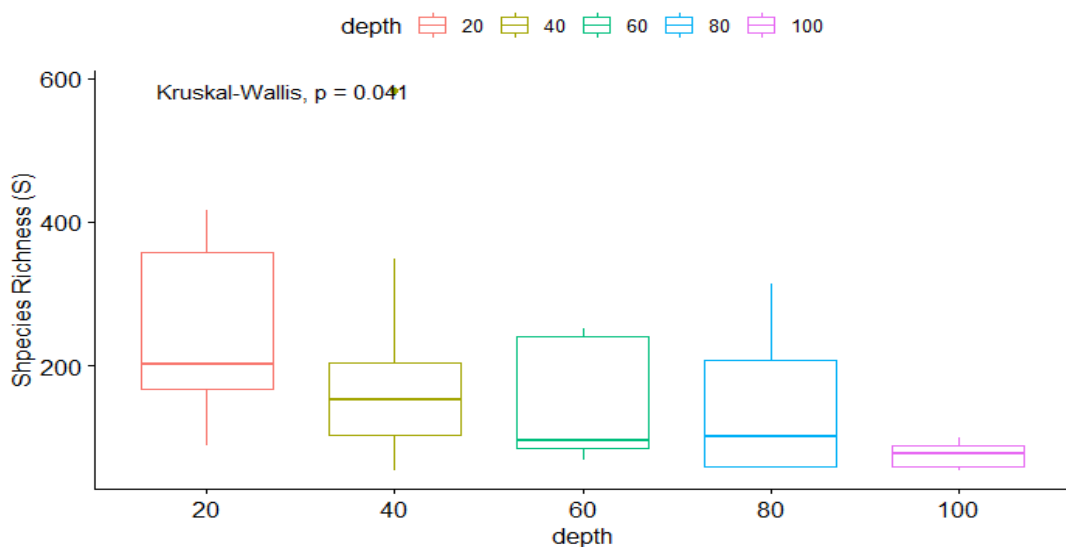


Figure 4.29 Boxplot of Species Richness (S) for 16S data, with Kruskal Wallis test between depth groups ($\alpha = 0.05$) from the initial soil sampling at the Lyon Arboretum fieldsite.

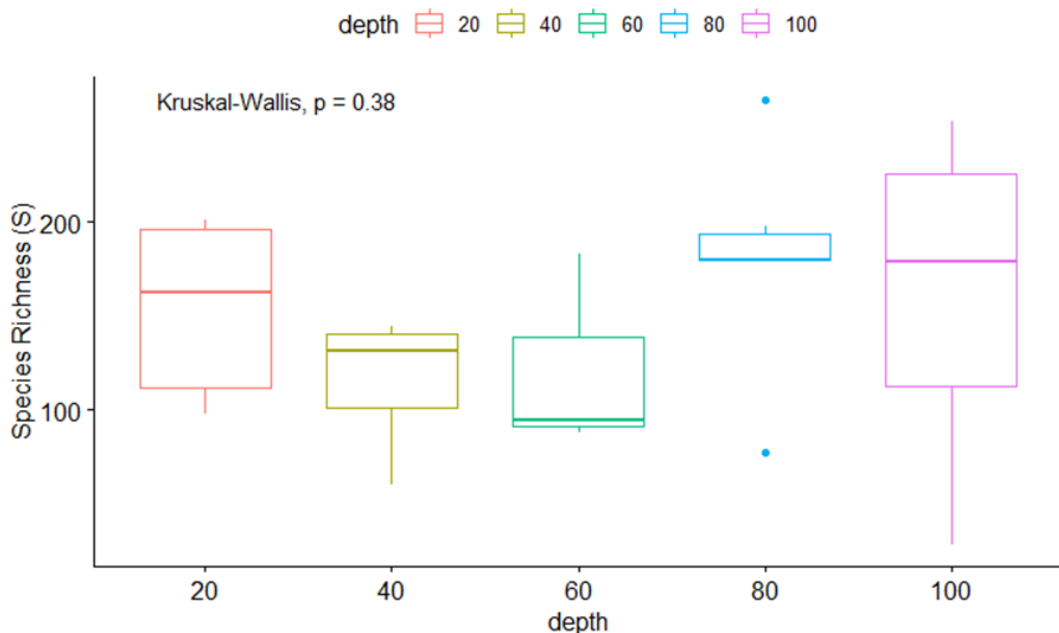


Figure 4.30 Boxplot of Species Richness (S) for ITS data, with Kruskal Wallis test between depth groups ($\alpha = 0.05$) from the initial soil sampling at the Lyon Arboretum fieldsite.

For the 16S data, the highest species abundance was at 20cm and the species abundance decreased with depth (Figure 4.29). For the ITS data, the highest species abundance was at 80 and 100cm, followed by 20cm and 40cm. 60cm had the lowest species abundance (Figure 4.30). A Kruskal Wallis test for differences between mean ranks among non-parametric groups found significant differences in the 16S data but, not the ITS data. A post-hoc Dunn's test of pairwise comparisons from the 16S data found that the only significantly different species abundance was at 20cm when compared to 100cm ($P = 0.01$).

Table 4.5 Summary of mean values with standard deviation for 16S and ITS across five sampling depths for Shannon's Diversity Index (H') and Species Richness (S) from the initial soil sampling at the Lyon Arboretum fieldsite.

Depth (cm)	H' 16S	H' ITS	S 16S	S ITS
20	4.89 ± 0.57	3.31 ± 0.88	239.70 ± 122.14	154.17 ± 48.41
40	4.62 ± 0.70	3.03 ± 0.76	198.10 ± 158.76	166.83 ± 33.65
60	4.32 ± 0.58	3.02 ± 1.04	143.22 ± 79.53	94.25 ± 69.95
80	4.19 ± 0.78	3.80 ± 0.70	142.88 ± 100.31	179.83 ± 60.26
100	3.69 ± 0.32	3.73 ± 0.54	76.00 ± 19.13	122.67 ± 96.06

Table 4.6 Summary of count of species found per guild by depth using FUNGuild developed by Nhu et al. (2016) from ITS data. Text in red is the highest count per guild by sampling depth.

Depth	20	40	60	80	100
<i>Arbuscular Mycorrhizal</i>	130	53	96	32	64
<i>Dung Saprotoph</i>	0	11	1	1	4
<i>Ectomycorrhizal</i>	10	10	28	5	12
<i>Endophyte</i>	1	4	1	1	3
<i>Fungal Parasite</i>	0	2	0	0	0
<i>Fungal Parasite/Wood Saprotoph</i>	0	1	0	0	0
<i>Leaf Saprotoph</i>	16	14	8	15	28
<i>Lichenized</i>	7	12	5	19	13
<i>Plant Pathogen/Wood Saprotoph</i>	27	5	39	12	17
<i>Soil Saprotoph</i>	0	0	0	0	1
<i>Undefined Saprotoph/Wood Saprotoph</i>	2	1	0	0	0
<i>Wood Saprotoph</i>	14	14	30	46	25

In Table 4.6 the most abundant fungal guild is arbuscular mycorrhiza, which was highest at 20cm. The second most abundant guild is the wood saprotrophs, which was highest at 80cm, followed by the closely related plant pathogens/ wood saprotrophs. By depth, excluding arbuscular mycorrhiza, the most abundant guild for each depth varied. At 20cm the most dominant guild groups were plant pathogen/wood saprotroph and leaf saprotroph. At 40cm the most dominant groups were leaf saprotroph and wood saprotroph. At 60cm the most dominant groups were plant pathogen/wood saprotroph and ectomycorrhiza. At 80cm the most dominant groups were leaf saprotroph and wood saprotroph. At 100cm the most dominant groups were leaf saprotroph and wood saprotroph.

4.5 DISCUSSION

Seasonal component of timeseries

There was a seasonal component detected across all timeseries variables of soil temperature, soil moisture and CO₂ produced. Soil temperature and moisture experienced direct effect of seasonality at all depths from 20cm to 100cm, clearly displayed by the ACF plot and the results of the ADF test for stationarity. The CO₂ produced only experienced a seasonal effect at 20cm, which is supported by the results of the static chamber experiment presented in Chapter 2. It is likely that the CO₂ produced only experienced a seasonal trend because it is a function of several factors including soil temperature and soil moisture which is mostly influencing the shallower depths.

The estimation of seasonality could be improved with more years of data collection. Given that there was only a year of data collection, the usual method of modeling the seasonal trend or pattern over time (at least two years) did not apply. Instead, a Fourier transformation was used to detect signals of seasonality and applied to extract the “seasonal” trend. While the seasonal trend can be improved in the future, the Fourier transformation did detect the expected higher temperatures in summer months and lower temperatures in the winter months. The soil moisture seasonal trend was less explicit with a seasonal pattern, but still significant as detected by the ADF test at all sampling locations. The soil moisture was lower in the months associated with less precipitation and higher in the rainy season. It is important to detect patterns of seasonality and properly transform the data to control for any confounding effect the change in seasonality might have for a model predicting significant factors contributing to changes in CO₂ production.

Interactive effects of deep soil warming

There are several factors significantly affecting the production of CO₂ at depth under experimental warming. The first group affecting CO₂ production were the timeseries variables of Δ soil temperature and soil moisture. While not the strongest grouping of predictors for CO₂ produced among soil properties, there is still a significant effect of seasonally adjusted Δ soil temperature and soil moisture on CO₂ produced at certain depths. Soil moisture in other tropical studies was found to be a significant factor of soil respiration, (Hashimoto et al., 2004) however, VWC was considered a weak predictor of CO₂ produced within the global model. The study soil is well drained and it studies have found that well drained soils are less affected by changes in precipitation than poorly drained soils (Davidson et al., 1998). Across the study period there was only a small significant change in soil moisture from the rain season to the dry season, however the iterative GAM modeling detected that VWC was not a good fit for predicting CO₂ produced ($\Delta i = 16.9$) when compared with other models including mineralogy, nutrients and pH. Therefore, soil moisture was not considered a significant predictor of CO₂ when compared to Δ soil temperature and other soil properties.

Seasonally adjusted mean Δ soil temperature was significant only at the surface of the profile at 20cm ($P = 1.44 \times 10^{-14}$) when modeled as a sole predictor of CO₂ produced ($R^2 = 0.81$, Deviance explained = 84.4%, n = 50). All other depths did not have a significant effect with mean seasonally adjusted soil temperature on CO₂ produced. This result is unique amongst other deep soil warming experiments which had a significant response of CO₂ across the whole profile. Soil microbes have the highest abundance in the top 20cm of the soil profile, therefore it is expected that there would be a statistically significant difference in CO₂ produced for the highest and lowest soil temperatures up to 20cm (Xiang et al., 2017). The increase in heat increases the rate of

metabolization for soil microbes therefore increasing rates of decomposition. Looking at Table 4.5, there was a higher abundance of bacteria at 20cm compared to other depths, however there was only statistically significantly differences from the abundance of bacteria at 100cm. The fungal abundance was not found to be statistically significantly different by a Kruskal Wallis test. Therefore, there must be other factors influencing the lack of CO₂ produced under augmented warming at depth >20cm.

It is expected that even deep within the soil profile (>30cm), for most soil orders, an increase in soil temperatures affects the amount of CO₂ being released by mobilizing a greater population of microbes. One study on a temperate Alfisol, found that the soil surface to 100cm, experienced a response to warming which increased soil respiration by 3% when compared to unheated profiles. About 20% of the soil respiration and 10% of the temperature response occurred at depths greater than 30cm (Pries et al., 2017). This was not the case within this study soil of a tropical Hawaiian Andisol. The mean temperature response was only significant at the upper 20cm of the soil profile for the period of November 2018 to August 2019. Within Andisols at depths deeper than 40cm, it is likely that mineralogical controls are stabilizing SOC and making organo-mineral complexes resistant to decomposition, even under augmented heating.

The other significant predictor term found from dredged global models for CO₂ produced was Δ pH. Δ pH is a measure of the net charge of soil colloids had a significant effect on CO₂ produced at 20cm ($P = 2.00 \times 10^{-14}$, n = 50) and 40cm ($P = 1.17 \times 10^{-04}$, n = 50). Figure 4.15 suggests that as net charge of the soil colloids goes from negative to positive and depth increases the response of CO₂ produced decreases. SOM has a net negative charge therefore could create strong bonds with non-crystalline minerals that exhibit a net positive charge in acidic environments. Therefore, this model is suggesting that at depths > 40cm with an increasingly positive net charge

of soil colloids could be increasing the stabilization of organic matter making it inaccessible to microbes.

In most soil types as soil temperature increases, so does the rates of soil respiration. The addition of heat increases the metabolic activity of the microbial communities and increases the rate at which CO₂ is produced. Other deep soil warming projects have experienced this change in CO₂ produced, consistent with the Arrhenius equation, where soil respiration increases then levels off. For this study, our original hypothesis was that Andisols would also follow the Arrhenius equation but, their unique mineralogy would be a limiting factor for CO₂ produced even under heating.

The original hypothesis states that even with experimental deep soil warming, areas with high non-crystalline mineral content will resist an increase in CO₂ produced. Non-crystalline minerals create organo-mineral complexes with SOM making it inaccessible to microbial decomposition. The high specific surface area and charge of the non-crystalline minerals attract SOM that otherwise could be metabolized by bacteria and saprotrophic fungi. In Figure 4.14, the relationship of decreasing CO₂ produced with increasing non-crystalline minerals is evident. There is an inflection point within the active Fe ratio at 0.5 at which there is lack of response in CO₂ produced even with soil warming. An active Fe ratio of 0.5 is the beginning of more non-crystalline minerals than crystalline minerals within the soil. There is also an inflection point within the Al +0.5Fe, non-crystalline concentration at 40,0000 mg kg⁻¹ soil, where the CO₂ response is resistant to soil warming. At 60, 80 and 100cm there is no response in soil respiration likely because of the high non-crystalline mineral concentration.

It is important to consider the effect of carbon (%C) on the amount of CO₂ produced. There is a strong delineation between differences in %C and non-crystalline minerals across depth. The

%C at depths < 40cm are statistically significantly greater than the %C at depths > 40cm. For non-crystalline minerals the opposite was true, non-crystalline minerals were statistically significantly greater at depths > 40cm than depths < 40cm. This depth delineation could be the reasoning that the model indicates a significant difference in CO₂ produced by depth. The mean %C at depths >40cm is ~2.6% and does not suggest that %C is a limiting factor at depth for microbial respiration. Therefore, even though the deep soil has less carbon, there should still be considerable metabolic activity at depth given the microbial abundance and low bulk density of the soil. The model fitted to non-crystalline minerals, Δ soil temperature and %C as predictors of CO₂ produced across all depths rather than by depth factor, found non-crystalline minerals as the most significant predictor of CO₂ produced, suggesting that the effect of non-crystalline minerals overwhelms the effect of %C. This finding suggests that even with augmented warming that is expected from climate change, non-crystalline mineralogy may help to resist loss of soil carbon at depth.

Microbial component

There were varied results in how bacterial and fungal communities exist over depth for the initial soil sampling. For the bacterial (16S) communities, species diversity and sequence abundance decreased with depth. Given existing knowledge on bacterial communities this result is expected. The upper 40cm is where the greatest amount of labile SOM exists for microbial metabolism, therefore the upper 40cm of the soil supports most of the microbial biomass. Fungal (ITS) communities produced similar results of high species diversity and sequence abundance at 20cm and 40cm. Unlike 16S communities, the ITS community diversity and richness were also highest at 80 and 100cm. Higher species diversity could mean that rarer fungi have developed at depth to exist in less than optimal conditions and maintain a unique functional niche.

Higher species abundance for fungi at depth is highly unusual. Given that most fungi require, oxygen, SOM, and ideal moisture conditions to survive, it is likely this unique soil is providing these needs at depth. Andisols can have very low bulk density allowing for large pore space where oxygen and water can be stored. Andisols are also rich in SOM, even at depth, when compared with other soils. These unique properties might be allowing for the ideal conditions at which hardy fungi can survive. Referring to the most abundant guilds by depth, 80 and 100cm have some of the highest levels of wood and leaf saprotrophs suggesting that there are available sources of C at depth. Even with high sequence abundance for ITS at depth, the effect of rising soil temperature did not significantly affect the rate of soil respiration for 80cm and 100cm. It is possible with prolonged warming the fungal communities at depth may experience significant changes in the rates of soil respiration that were not seen within the time constraints of this study.

It was expected that the “threshold of warming” could be reached in a few months or years, based off similar study designs found in the literature. It is expected that bacterial sequence abundance will increase while fungal sequence abundance will decrease from the initial sampling to the threshold of warming sampling time period which was not indicated by the top 20cm for this study period. It is also predicted that community diversity (calculated by the Shannon Diversity Index) for both bacteria and fungi will decrease based on the highly specific functional niche created by the intensified warming.

It has been shown that biological activity increases with temperature following the Boltzmann’s factor. This relationship is sustained for temperatures for normal metabolic function from 0° to 40° (Brown et al., 2002).

$$e^{(-\frac{E}{kT})} \quad \textbf{Equation 4.4}$$

Where E is the activation energy, k is Boltzmann's constant, and T is absolute temperature in K (Boltzmann, 1879). Pietikainen et al. (2005) found that beyond 30°C, there was a dramatic decrease in fungal abundance. Therefore, with a +4°C soil warming to the fieldsite it is expected that there will be a decrease fungal abundance. For bacteria, the mesophilic thermal threshold is 40 °C. Therefore, with soil warming the overall abundance of bacteria will increase since the amount of warming will not exceed the 40 °C threshold. Changes in Shannon Diversity were not analyzed after warming since a longer period of warming is expected to shift community diversity.

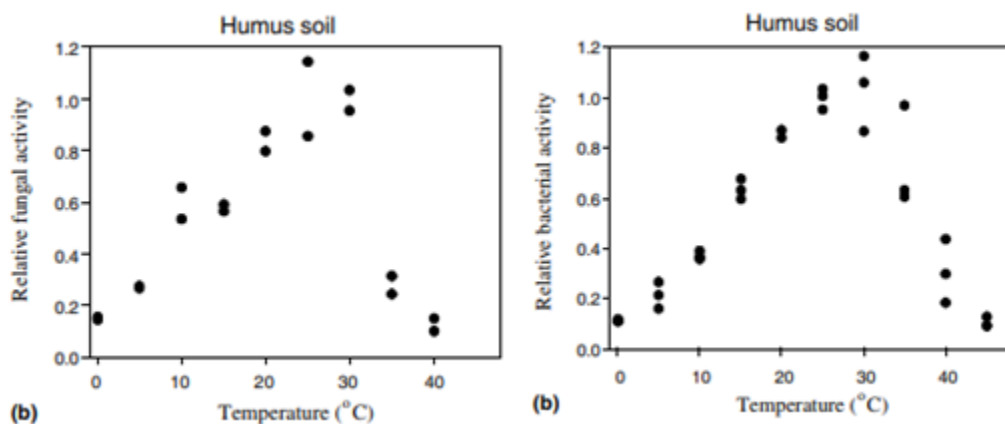


Figure 4.31 Results from the high organic matter soils for relative bacterial activity (left) and relative fungal activity (right) from Pietikainen et al. (2005)

Allen et al. (2002), found the Boltzmann's factor has the same relationship between species richness and environmental temperature, with metabolic rate and environmental temperature.

$$\text{Log transformed bacterial species richness} = \log(S \propto e^{-E/kT})$$

Equation 4.5

Where S is species richness, k is Boltzman's constant, T is absolute temperature (in Kelvin) and E is the 'activation energy' in eV characterizing the temperature dependence of species

richness. Based off this function and the literature review, it is expected that overall richness in species will decrease with increased temperature because of the highly specific functional niche created by the intensified warming for both bacteria and fungi. After it is indicated that a threshold of warming is reached for this study, a second soil sampling for microbial communities should be taken to understand how species richness and diversity has been affected by warming.

4.6 CONCLUSION

Understanding the feedbacks of soil respiration to rising global air temperatures provides critical information to climate models and how the carbon cycle may be impacted by future climatic changes. Within the International Soil Experimental Network (iSEN), underrepresented soil and climate types must be expanded upon in order to develop an accurate representation of the future of soil organic carbon (SOC). This study piloted a low-cost methodology on a soil type new to iSEN, while adding to the lack of empirical evidence on the effects of soil warming on tropical soils. Andisols are a critical tropical soil to be integrated given their unique mineralogy.

Through a low-cost novel temperature sensor and soil warming network this study heated the soil profile of a Hawaiian Andisol from November 2018 to August 2019. The site was heated across a gradient of temperatures rather than several heated and ambient control sites cutting down on overall costs. The in-house production of the temperature sensors, dataloggers, heating controller and soil heating probes also sufficiently cut down on costs compared to other soil warming experiments within the iSEN. The most expensive piece of field equipment, the heating controller, was only 15% of the cost of one of the heating controllers at the Blodgett Experimental Forest from the Pries et al (2017) study. This low-cost methodology could be used to quickly integrate other soil and climate types that are not within the iSEN due to insufficient funding.

It was found that only the top 20cm responded to increased soil temperatures while deeper within the soil profile was resistant to change. In all other soil warming experiments the whole soil profile responded to augmented heating rather than just the upper 20cm. This suggests that there is a limiting factor to soil respiration at deeper depths within a Hawaiian Andisol. Using a multimodal approach several factors were determined to be the most significant predictors of CO₂ produced. First, a global model was developed of all the variables collected using generalized

additive modeling using the “mcgv” package in R. Then, the global model was “dredged” to select the most significant predictors of CO₂ produced. For the model dredging, model subsets were compared using the Akaike Information Criterion (AIC) in the “MuMIn” package in R and the subset models were ranked from the lowest to highest AIC scores. The top ten predictors of CO₂ produced were selected by the results of the results of the model dredging. Then we looked to Principal Component Analysis (PCA) to understand the deeper trends within the model and to fine tune the model results to be more representative of the fieldsite. The PCA displayed distinct depth categories, therefore using the top ten predictors of CO₂ produced we performed a “manual dredge” to look at all possible model iterations of the top ten predictors by each sampling depth. Using a AIC threshold of $\Delta i = 10$ where $\Delta i = AIC_i - AIC_{min}$, the top models for predicting CO₂ produced were selected as the top predictors of CO₂ produced. Within the global model it is not possible to fine tune the model due to the lack of availability of extra smoothers when trying to fit a model for all potential predictors. Therefore, the steps to create the global model, dredge it, then fine tune the model by the trends within the PCA was the best way to include all parameters but avoid selection biases.

Resulting from the multimodal process the five main predictors of CO₂ produced were selected from the top three models. Δ soil temperature and Δ pH were both included as important predictors of CO₂ produced. Δ soil temperature was only significant at 20cm, unlike any other soil warming project where all depths were significant. Δ pH was a significant predictor only for the upper 40cm. Δ pH is a measure of the net charge of soil colloids within acidic soils. For the top 40cm the net charge is overwhelming negative, however within the deeper depths the net charge of the soil colloids, as measured by Δ pH, moves toward a positive net charge. CO₂ produced could be limited at these deeper depths by these positively charge soil colloids bonding with net

negatively charged organic matter and making it inaccessible to soil microbes. Non-crystalline minerals that are expected to be abundant at depth within Hawaiian Andisols exhibit a net positive charge in acidic soils. The net positive charge as displayed by the Δ pH in the acidic soils at the fieldsite, could be indicator of net positively charged non-crystalline minerals deep within the soils.

The top two models for predictors of CO₂ produced found Δ soil temperature, Δ pH and non-crystalline minerals as the most significant factors inhibiting the soil respiration response under augmented warming. The Active Fe ratio and Al + 0.5Fe as measures of non-crystalline mineralogy were both significant predictors of CO₂ produced in the upper 40cm of the soil profile. As the non-crystalline mineral concentration increased deeper within the soil profile there was a lack of a significant CO₂ response. This could be potentially because of the non-crystalline minerals complexing with the soil organic matter making the soil carbon unavailable to soil microbes. Understanding this end member process is crucial to determine the fate of SOC within these unique soils.

The third best model presented Δ soil temperature, Δ pH and carbon (%C) as the most important predictors of CO₂ produced. The relationship between CO₂ produced and carbon is a known positive relationship. The increased availability of carbon increases the rates of soil respiration in the presence of microbes; therefore, this is an expected predictor of CO₂ produced. As the concentration of non-crystalline minerals increases, it is expected that carbon would also increase because of complexation, however within this study site this was not the case. This unique relationship needs to be addressed before moving forward in understanding the mineralogical controls on SOC under rapid augmented warming. Further studies recommended would be an incubation study to test different concentrations of non-crystalline minerals and carbon content under a Q10 context of warming (rate of reaction increase in microbial activity with each 10°C

increase in warming). A subset of soil samples testing the whole gradient of non-crystalline minerals and carbon content found across the field site, could be incubated in three different chambers set at ambient soil temperature, ambient soil temperature - 5°C and ambient soil temperature + 5°C. Then within the samples soil respiration could be measured until a threshold of warming is reached. Using the changes in soil respiration across the temperature and mineralogy gradient the Q10 value could be developed to determine the rate at which microbes are respiring within different levels of non-crystalline mineral concentrations.

Within the microbial component of this study, there are limitations to the conclusions that can be made on the overall influence of microbial communities. Overall, bacterial sequence abundance was only significantly different at the shallowest depth (20cm) and the deepest depth (100cm). Fungal sequence abundance was not significantly different across depths. The fieldsite soil has a low bulk density which could be allowing for oxygen to be available to microbes at deeper depths. The fungal sequence abundance could be higher than the bacterial sequence abundance at depth since bacteria cannot function in high charge environments due to the need to exchange protons. The limitation with this data however is that all analysis is product of DNA sequencing which can include dead microbes. Further studies should investigate using RNA to look at the live communities in the soil and see if the trends of high fungal abundance still exist at depth. Studies should also investigate resampling the fieldsite after a few more years of heating to see how microbial communities may have changed.

Overall this study found that Hawaiian Andisols only responded to augmented soil temperature at the top 20cm of the profile, unlike any other soil warming experiment. The multimodal approach to data analysis suggests that non-crystalline minerals are the main parameter influencing the lack of significant CO₂ response at depth. With more studies looking at the specific

controls of mineralogy and the microbial component at depth, Andisols could be managed as a climate change mitigation tool due to their lack of response from the expected rise in temperatures from climate change. Andisol conservation could offer a potential low cost and easy to implement option to carbon sequestrations under a changing climate, while longer term solutions to destructive human behavior are enacted.

LITERATURE CITED

- Allen, Andrew P., et al. "Global Biodiversity, Biochemical Kinetics, and the Energetic-Equivalence Rule." *Science*, vol. 297, no. 5586, Aug. 2002, pp. 1545–48. doi:10.1126/science.1072380.
- Baldock, J., and K. Broos. "Soil Organic Matter." *Handbook of Soil Sciences*, CRC Press, 2011, pp. 1–52.
- Barton, Kamil. *MuMIn: Multi-Model Inference. R Package Version 1.43.6*. 2019, <https://CRAN.R-project.org/package=MuMIn>
- Bekku, Yukiko Sakata, et al. "Effect of Warming on the Temperature Dependence of Soil Respiration Rate in Arctic, Temperate and Tropical Soils." *Applied Soil Ecology*, vol. 22, no. 3, Mar. 2003, pp. 205–10. doi:10.1016/S0929-1393(02)00158-0.
- Brady, N., and Raymond Weil. *The Nature and Properties of Soil*. 13th ed., Prentice-Hall, Inc, 2005.
- Burnham, Kenneth, and David Anderson. *Model Selection and Multimodel Inference*. Springer Science & Business Media, 2003.
- Chadwick, Oliver A., et al. "The Impact of Climate on the Biogeochemical Functioning of Volcanic Soils." *Chemical Geology*, vol. 202, no. 3–4, Dec. 2003, pp. 195–223. doi:10.1016/j.chemgeo.2002.09.001.
- Chadwick, Oliver A., and Jon Chorover. "The Chemistry of Pedogenic Thresholds." *Geoderma*, vol. 100, no. 3–4, May 2001, pp. 321–53. doi:10.1016/S0016-7061(01)00027-1.
- Crow, Susan E., et al. "Optimization of Method to Quantify Soil Organic Matter Dynamics and Carbon Sequestration Potential in Volcanic Ash Soils." *Biogeochemistry*, vol. 123, no. 1–2, Mar. 2015, pp. 27–47. doi:10.1007/s10533-014-0051-6.
- Crowther, T. W., et al. "Quantifying Global Soil Carbon Losses in Response to Warming." *Nature*, vol. 540, no. 7631, Dec. 2016, pp. 104–08. doi:10.1038/nature20150.
- Davidson, Eric A., et al. "Soil Water Content and Temperature as Independent or Confounded Factors Controlling Soil Respiration in a Temperate Mixed Hardwood Forest." *Global Change Biology*, vol. 4, no. 2, Feb. 1998, pp. 217–27. doi:10.1046/j.1365-2486.1998.00128.x.
- Eversole, D., and A. Andrews. *Climate Change Impacts in Hawai'i: A Summary of Climate Change and Its Impacts to Hawai'i's Ecosystems and Communities*. University of Hawai'i at Mānoa Sea Grant College Program, 2014
- Field, Christopher, and Michael Raupach. *The Global Carbon Cycle: Integrating Humans*,

Climate, and the Natural World. Island Press, 2004.

Giardina, Christian P., et al. "Warming-Related Increases in Soil CO₂ Efflux Are Explained by Increased below-Ground Carbon Flux." *Nature Climate Change*, vol. 4, no. 9, Sept. 2014, p. 822. doi:10.1038/nclimate2322.

Gislason, S. R., et al. "Chemical Weathering of Basalt in Southwest Iceland; Effects of Runoff, Age of Rocks and Vegetative/Glacial Cover." *American Journal of Science*, vol. 296, no. 8, Oct. 1996, pp. 837–907. doi:10.2475/ajs.296.8.837.

Hanson, Paul J., et al. "Attaining Whole-Ecosystem Warming Using Air and Deep-Soil Heating Methods with an Elevated CO₂ Atmosphere." *Biogeosciences*, vol. 14, no. 4, Feb. 2017, pp. 861–83. doi:10.5194/bg-14-861-2017.

Hashimoto, Shoji, et al. "Soil Respiration and Soil CO₂ Concentration in a Tropical Forest, Thailand." *Journal of Forest Research*, Feb. 2004. Tokyo, doi:10.1007/s10310-003-0046-y.

Hastie, Trevor, and Robert Tibshirani. "Generalized Additive Models." *Statistical Science*, vol. 1, no. 3, Aug. 1986, pp. 297–310. *projecteuclid.org*, doi:10.1214/ss/1177013604.

Hernández-Soriano, María C. "The Role of Aluminum-Organo Complexes in Soil Organic Matter Dynamics." *Soil Health and Land Use Management*, InTech, 2012.

Hillel, D., and C. Rosenzweig. "Soil Carbon and Climate Change: Carbon Exchange in the Terrestrial Domain and the Role of Agriculture." *CSA News*, vol. 54, no. 6, 2009, pp. 4–11.

Hobbs, Thompson. "Modification of Ecosystems by Ungulates." *The Journal of Wildlife Management*, vol. 60, no. 4, Oct. 1996, pp. 695–713.

Hodder, A., et al. "Towards an Understanding of Thermodynamic and Kinetic Controls on the Formation of Clay Minerals from Volcanic Glass under Various Environmental Conditions." *Recent Research Developments in Chemical Geology*, 1996, pp. 1–11.

Holmgren, G. "A Rapid Citrate-Dithionite Extractable Iron Procedure." *Soil Sci. Soc.A. J*, vol. 31, no. 2, 1967, pp. 210–211.

Jackson, Robert B., et al. "The Ecology of Soil Carbon: Pools, Vulnerabilities, and Biotic and Abiotic Controls." *Annual Review of Ecology, Evolution, and Systematics*, vol. 48, 2017, pp. 419–445.

Jobbágy, Esteban G., and Robert B. Jackson. "The Vertical Distribution of Soil Organic Carbon and Its Relation to Climate and Vegetation." *Ecological Applications*, vol. 10, no. 2, 2000, pp. 423–436.

Lammel, Daniel R., et al. "Specific Microbial Gene Abundances and Soil Parameters Contribute

to C, N, and Greenhouse Gas Process Rates after Land Use Change in Southern Amazonian Soils.” *Frontiers in Microbiology*, vol. 6, Oct. 2015.
doi:10.3389/fmicb.2015.01057.

Leamy, M. “International Committee on the Classification of Andisols (ICOMAND).” *New Zealand Soil Bureau. DSIR, Lower Hutt.*, vol. 6, 1984.

Lehmann, Johannes, and Markus Kleber. “The Contentious Nature of Soil Organic Matter.” *Nature*, vol. 528, Nov. 2015, p. 60.

Lever, Jake, et al. “Principal Component Analysis.” *Nature Methods*, 29 June 2017,
doi:10.1038/nmeth.4346.

Lloyd, J., and J. A. Taylor. “On the Temperature Dependence of Soil Respiration.” *Functional Ecology*, vol. 8, no. 3, June 1994, p. 315. doi:10.2307/2389824.

Lowe, David. “Controls on the Rates of Weathering and Clay Mineral Genesis in Airfall Tephras: A Review and New Zealand Case Study.” *Rates of Chemical Weathering of Rocks and Minerals*, Academic Press, 1986, pp. 265–330,

Matus, Francisco, et al. “Soil Carbon Storage and Stabilization in Andic Soils: A Review.” *CATENA*, vol. 120, Sept. 2014, pp. 102–10. doi:10.1016/j.catena.2014.04.008.

McDaniel, Paul, et al. *Andisols*. 2nd ed., vol. 1, CRC Press (Taylor & Francis), 2012, pp. 3329–48.

McKeague, J. A. “An Evaluation of 0.1Mpyrophosphate and Pyrophosphate-Dithionite in Comparison with Oxalate as Extractants of the Accumulation Productsin Podzols and Some Other Soils.” *Can. J. Soil Sci*, vol. 47, 1967, pp. 95–99.

Meyer, N., et al. “The Temperature Sensitivity (Q10) of Soil Respiration: Controlling Factors and Spatial Prediction at Regional Scale Based on Environmental Soil Classes.” *Global Biogeochemical Cycles*, vol. 32, no. 2, Feb. 2018, pp. 306–23.
doi:10.1002/2017GB005644.

Mizota, C., and L. P. van Reeuwijk. “Clay Mineralogy and Chemistry of Soils Formed in Volcanic Material in Diverse Climatic Regions.” *Clay Mineralogy and Chemistry of Soils Formed in Volcanic Material in Diverse Climatic Regions.*, no. No. 2, 1989.

Moyes, Andrew B., and David R. Bowling. “Interannual Variation in Seasonal Drivers of Soil Respiration in a Semi-Arid Rocky Mountain Meadow.” *Biogeochemistry*, vol. 113, no. 1–3, May 2013, pp. 683–97. link.springer.com, doi:10.1007/s10533-012-9797-x.

Nanzyo, Masami. “Unique Properties of Volcanic Ash Soils.” *Glob. Environ. Res.*, vol. 6, 2002.
Oksanen, Jari, et al. *Vegan: Community Ecology Package. R Package Version 2.5-5*. 2019,
<https://CRAN.R-project.org/package=vegan>.

- Ontl, T., and L. Schulte. *Soil Carbon Storage*. Nature Education Knowledge, 2012.
- Pachauri, R. K., et al., editors. *Climate Change 2014: Synthesis Report*. Intergovernmental Panel on Climate Change, 2015.
- Parfitt, R. L. "Allophane and Imogolite: Role in Soil Biogeochemical Processes." *Clay Minerals*, vol. 44, no. 1, Mar. 2009, pp. 135–55. *CrossRef*, doi:10.1180/claymin.2009.044.1.135.
- Peters, M., et al. "Climate-Land-Use Interactions Shape Tropical Mountain Biodiversity and Ecosystem Functions." *Nature*, vol. 568, no. 7750, 2019, pp. 88–92.
- Pietikainen, Janna, et al. "Comparison of Temperature Effects on Soil Respiration and Bacterial and Fungal Growth Rates." *FEMS Microbiology Ecology*, vol. 52, no. 1, Mar. 2005, pp. 49–58. *CrossRef*, doi:10.1016/j.femsec.2004.10.002.
- Post, W. M., and K. C. Kwon. "Soil Carbon Sequestration and Land-Use Change: Processes and Potential." *Global Change Biology*, vol. 6, no. 3, Mar. 2000, pp. 317–27. doi:10.1046/j.1365-2486.2000.00308.x.
- Pries, Caitlin E. Hicks, et al. "The Whole-Soil Carbon Flux in Response to Warming." *Science*, vol. 355, no. 6332, Mar. 2017, pp. 1420–23. doi:10.1126/science.aal1319.
- Risch, Anita C., et al. "Grubbing by Wild Boars (*Sus Scrofa L.*) and Its Impact on Hardwood Forest Soil Carbon Dioxide Emissions in Switzerland." *Oecologia*, vol. 164, no. 3, Nov. 2010, pp. 773–84. *link.springer.com*, doi:10.1007/s00442-010-1665-6.
- Ross, G., et al. "Hydroxylamine and Ammonium Oxalate Solutions as Extractants for Fe and Al from Soils." *Soil Sci. Soc. Am. J.*, vol. 49, pp. 783–785.
- Rousk, Johannes, Philip C. Brookes, et al. "Contrasting Soil PH Effects on Fungal and Bacterial Growth Suggest Functional Redundancy in Carbon Mineralization." *Applied and Environmental Microbiology*, vol. 75, no. 6, Mar. 2009, pp. 1589–96. *PubMed*, doi:10.1128/AEM.02775-08.
- Rousk, Johannes, Erland Bååth, et al. "Soil Bacterial and Fungal Communities across a PH Gradient in an Arable Soil." *The ISME Journal*, vol. 4, no. 10, Oct. 2010, pp. 1340–51. *PubMed*, doi:10.1038/ismej.2010.58.
- Rustdad, Lindsey, and Ivan Fernandez. "Experimental Soil Warming Effects on CO₂ and CH₄ Flux from a Low Elevation Spruce–Fir Forest Soil in Maine, USA." *Global Change Biology*, vol. 4, no. 6, 2004, doi: 10.1046/j.1365-2486.1998.00169.x.
- Scharlemann, Jörn PW, et al. "Global Soil Carbon: Understanding and Managing the Largest Terrestrial Carbon Pool." *Carbon Management*, vol. 5, no. 1, Feb. 2014, pp. 81–91.

CrossRef, doi:10.4155/cmt.13.77.

Schwertmann, W. "The Differentiation of Iron Oxide in Soils by a Photochemical Extraction with Acid Ammonium Oxalate." *Z. Pflanzenernaehr, Duens. Bodenk.*, vol. 105, 1964, pp. 194–201.

Shoji, S., R. Dahlgren, et al. "Chapter 2 Morphology of Volcanic Ash Soils." *Developments in Soil Science*, vol. 21, 1993, pp. 7–35

Shoji, S., Y. Suzuki, et al. "Clay Mineralogical and Chemical Properties of Nonallophanic Andepts (Andisols) from Oregon. USA." *Soil Sci. Soc. Am. J.*, vol. 51, no. 4, 1987, pp. 986–990.

Shoji, S., and Tsuyoshi Ono. "Physical and Chemical Properties and Clay Mineralogy of Andosols from Kitakami. Jpn." *Soil Science*, vol. 126, no. 5, 1978, pp. 297–312.

Smith, Pete. "Land Use Change and Soil Organic Carbon Dynamics." *Nutrient Cycling in Agroecosystems*, vol. 81, no. 2, June 2008, pp. 169–78.
doi:10.1007/s10705-007-9138-y.

Takahashi, T., and R. Dahlgren. "Nature, Properties and Function of Aluminum–Humus Complexes in Volcanic Soils." *Geoderma*, vol. 263, Feb. 2016, pp. 110–21.
doi:10.1016/j.geoderma.2015.08.032.

Takezawa, Kunio. *Learning Regression Analysis by Simulation*. Springer Science & Business Media, 2014.

Torn, M. S., et al. "A Call for International Soil Experiment Networks for Studying, Predicting, and Managing Global Change Impacts." *SOIL*, vol. 1, no. 2, Aug. 2015, pp. 575–82.
doi:10.5194/soil-1-575-2015.

Torn, Margaret S., et al. "Mineral Control of Soil Organic Carbon Storage and Turnover." *Nature*, vol. 389, no. 6647, Sept. 1997, p. 170, doi:10.1038/38260.

van der Heijden, Marcel G. A., et al. "The Mycorrhizal Contribution to Plant Productivity, Plant Nutrition and Soil Structure in Experimental Grassland." *New Phytologist*, vol. 172, no. 4, Dec. 2006, pp. 739–52. doi:10.1111/j.1469-8137.2006.01862.x.

Wood, Simon. *Generalized Additive Models: An Introduction With R*. Chapman and Hall/CRC Press, 2006

Xiang, Yun, et al. "Changes in Soil Microbial Community and Its Effect on Carbon Sequestration Following Afforestation on the Loess Plateau, China." *International Journal of Environmental Research and Public Health*, vol. 14, no. 8, Aug. 2017.
doi:10.3390/ijerph14080948.

APPENDIX A. The depths associated with each sample and the channel paths for the live data link (<http://grogdata.soest.hawaii.edu/>)

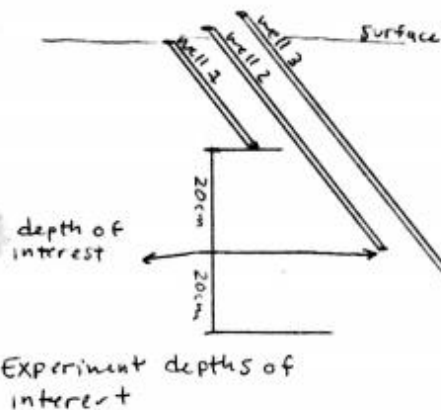
Sensor/gas well	Depth (cm)	Node	Node Channel	Type
1	20	146	T0	
2	40	142	T0	
3	60	142	T1	
4	80	146	T1	
5	100	142	T2	
6	20	146	T2	
7	40	142	T3	
8	60	146	T3	control
9	80	142	T4	
10	100	142	T5	
11	20	147	T0	
12	40	144	T0	
13	60	146	T4	
14	80	144	T1	
15	100	147	T1	
16	20	146	T5	
17	40	147	T2	
18	60	144	T2	
19	80	147	T3	
20	100	147	T4	
21	20	147	T5	
22	40	141	T0	
23	60	141	T1	
24	80	141	T2	
25	100	141	T3	
26	20	144	T3	
27	40	141	T4	
28	60	141	T5	control

29	80	147	T6	
30	100	141	T6	
31	20	143	T0	
32	40	143	T1	
33	60	143	T2	
34	80	144	T4	
35	100	143	T3	
36	20	143	T4	
37	40	140	T0	
38	60	144	T5	control
39	80	143	T5	
40	100	143	T6	
41	20	140	T1	
42	40	85	T0	
43	60	85	T1	
44	80	140	T2	
45	100	140	T3	
46	20	85	T2	
47	40	85	T3	
48	60	140	T4	control
49	80	85	T4	
50	100	140	T5	
51	60	142	T6	heating
52	60	146	T6	heating
53	60	147	T7	heating
54	60	141	T6	heating
55	60	85	T5	heating

APPENDIX B. Fick's law CO₂ production calculations.

Lyon flux density:

Experimental set-up



- 20 cm
 - 40 cm
 - 60 cm
 - 80 cm
 - 100 cm
- x 10 locations per depth of interest

① Find molar density of air from Ideal Gas Law

$$\frac{n}{V} = \frac{P}{RT}$$

↑
constant
local pressure @ time of interest

↑
at time and depth of interest
temp (in Kelvin)

② What part of air is CO₂? Use molar density of air (in μmol/m³) multiplied by CO₂ concentration in ppm (gas well data)

$$\frac{n}{V}_{\text{well 1}} = \frac{n}{V}_{\text{air}} \times \left(\frac{\text{well 1 conc.}}{1,000,000} \right)$$

$$\frac{n}{V}_{\text{well 2}} = \frac{n}{V}_{\text{air}} \times \left(\frac{\text{well 2 conc.}}{1,000,000} \right)$$

$$\frac{n}{V}_{\text{well 3}} = \frac{n}{V}_{\text{air}} + \left(\frac{\text{well 3 conc.}}{1,000,000} \right)$$

③ Ficks Law of diffusion: what is the flux between each depth layer?

since diffusion occurs in direction opposite increasing concentration

④

$$\frac{dc}{dz_1} = \frac{\frac{n}{V}_{\text{well 2}} - \frac{n}{V}_{\text{well 1}}}{-0.2 \text{ m}}$$

$$\frac{dc}{dz_2} = \frac{\frac{n}{V}_{\text{well 3}} - \frac{n}{V}_{\text{well 2}}}{-0.2 \text{ m}}$$

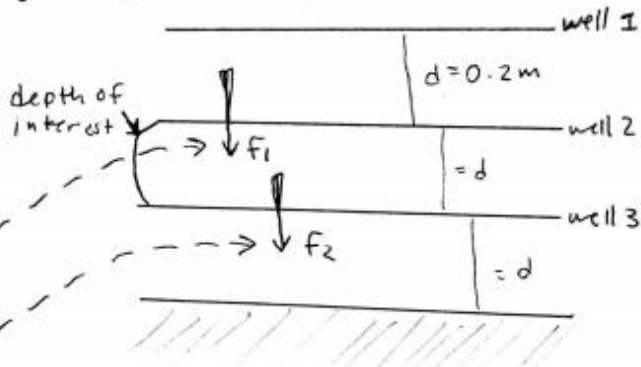
$$f_1 = \frac{dc}{dz_1} * -D$$

$$f_2 = \frac{dc}{dz_2} * -D$$

dimensionless tortuosity

where $-D = D_{00} * \zeta$

$$D_{00} \left(\frac{T}{293.15} \right)^{1.75} \left(\frac{101.3}{P} \right)$$



CO₂ is diffusing from high to low concentration (shallow to deep)

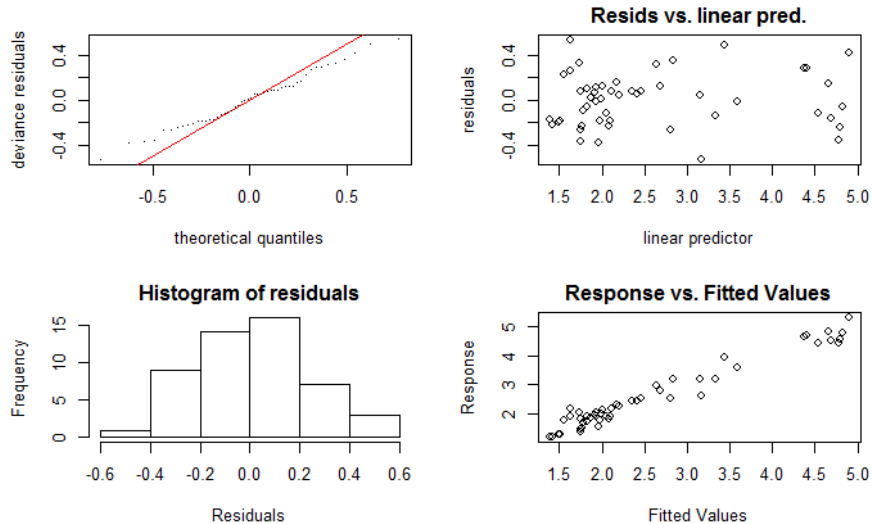
CO₂ produced from depth of interest = $\frac{f_2 - f_1}{d}$

$(\mu\text{mol m}^{-3} \text{s}^{-1})$

APPENDIX C. Quality check plots for the top four optimization equations.

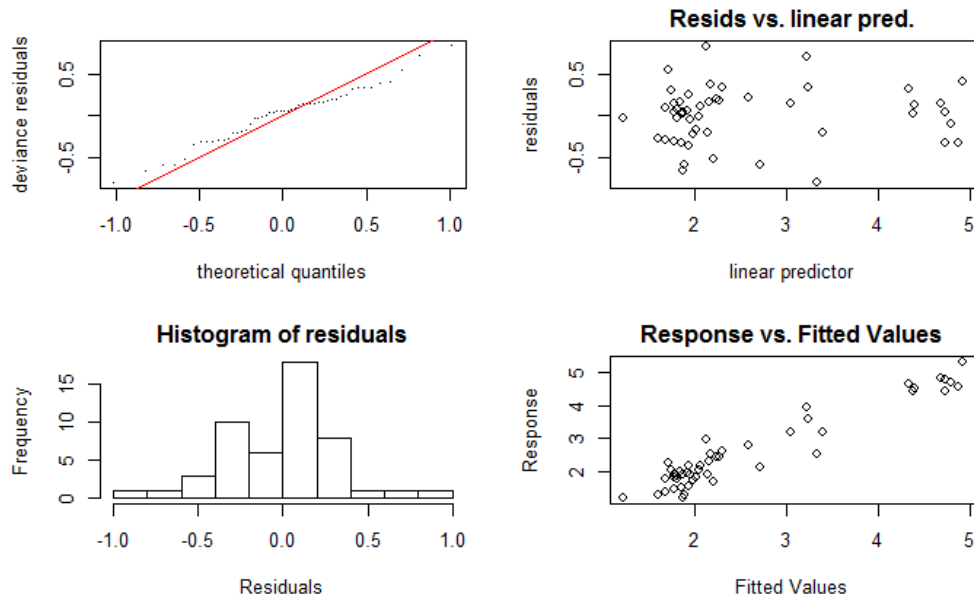
Formula:

$\log(\text{co2}) \sim s(\text{Delta_temp}, k=3, \text{by} = \text{depth}) + s(\text{Delta_pH}, k=3, \text{by} = \text{depth}) + s(\text{Fe_h_Fe_d}, k=3, \text{by} = \text{depth}) + s(\text{id}, \text{bs} = "re") + 1$



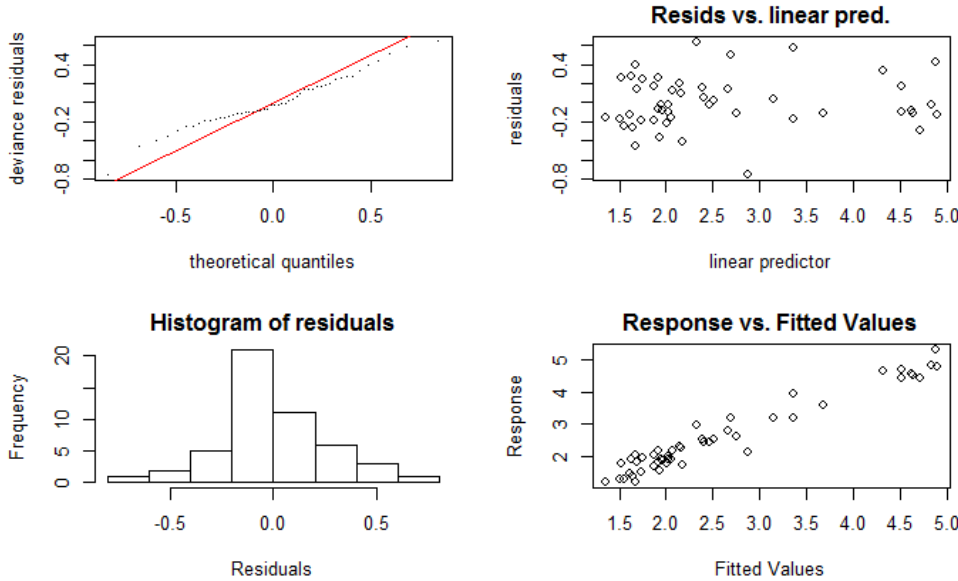
Formula:

$\log(\text{co2}) \sim s(\text{Delta_temp}, k=3, \text{by} = \text{depth}) + s(\text{Delta_pH}, k=3, \text{by} = \text{depth}) + s(\text{C}, k=3, \text{by} = \text{depth}) + s(\text{id}, \text{bs} = "re") + 1$



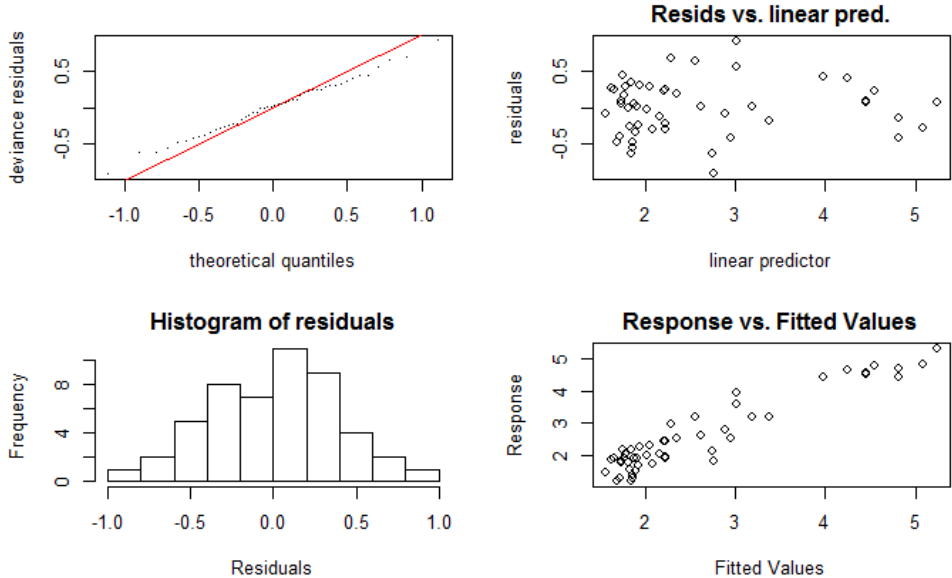
Formula:

$\log(\text{co2}) \sim s(\text{Delta_temp}, k=3, \text{by} = \text{depth}) + s(\text{Delta_pH}, k=3, \text{by} = \text{depth}) + s(\text{non_crystal}, k=3, \text{by} = \text{depth}) + s(\text{id}, \text{bs} = "re") + 1$



Formula:

$\log(\text{co2}) \sim s(\text{Delta_temp}, k=3, \text{by} = \text{depth}) + s(\text{Delta_pH}, k=3, \text{by} = \text{depth}) + s(\text{pH}, k=3, \text{by} = \text{depth}) + s(\text{id}, \text{bs} = "re") + 1$



APPENDIX D. Qiime 2.0 ITS pipeline taken from Nhu Nguyen Microbiology lab

```
#####
# CREATE A QIIME METADATA FILE
#####
#The QIIME metadata file is a tab-delimited file that contains the
#necessary information regarding your experimental data.
#It is necessary for processing raw reads and perform basic analyses
#at least the following columns are required:

#SampleID      BarcodeSequence          LinkerPrimerSequence
#Treatment     Description
Heated40C.1    CGTACGATAAGTCGAG      NA
+40C           Something

#"#" defines the header line
#"SampleID", for clarity should be something that is informative towards
the experiment not just the sample number.
#"BarcodeSequence" for dual-barcoding should be concatenated into a single
string. The format should be ReverseComplementI2+I1.
#"LinkerPrimerSequence" is for 454 pyrosequencing. Not required for
Illumina data.
#"Treatment" is the basic treatment. Add as many columns as necessary for
your experimental needs.
#"Description" has to be at the end. It's not used in analyses and is
typically useless but it's required.

#Use Keemei (plugin) to validate your metadata file in Google Sheets. Make
sure that it is error free before going forward!
https://keemei.qiime2.org/

#####data was demuxed by Nhu and then added to "demux" folder using
shell command#####
#!/bin/sh
for dir in */ ; do
    mv $dir/* ./demux/
done

#####importing data#####
#ACTIVATE the environment that QIIME2 was installed in
source activate qiime2-2018.11
source activate qiime2-2018.8
```

```

#####
##### PREPARING YOUR RAW SEQUENCE DATA FOR DEMULTIPLEXING #####
#####
#DOWNLOAD your raw data into a folder. You should have 4 files: R1, R2,
I1, I2.
mkdir rawdata_03
cd rawdata_03

#UNZIP all files, saving the original files .gz files (for later use)
gunzip -k *

#RENAME your raw data
mv CMAIKI-Miseq3-all_S1_L001_I1_001.fastq I1.fastq
mv CMAIKI-Miseq3-all_S1_L001_I2_001.fastq I2.fastq
mv CMAIKI-Miseq3-all_S1_L001_R1_001.fastq forward.fastq
mv CMAIKI-Miseq3-all_S1_L001_R2_001.fastq reverse.fastq

#MOVE the fastq files to the "gz_data" folder
cd..
mkdir gzdata_03
##### this directory for ITS MiSeq03 only, all others in gz_data
##### folder#####
mv rawdata_03/I1.fastq gzdata_03/I1.fastq
mv rawdata_03/I2.fastq gzdata_03/I2.fastq
mv rawdata_03/forward.fastq gzdata_03/forward.fastq
mv rawdata_03/reverse.fastq gzdata_03/reverse.fastq

#####below step done by Nhu after issues with getting code to run on
lab desktop#####
#EXTRACT barcodes from I1 & I2 files using macqiime (QIIME1)
#You will need to have QIIME1 (MACQIIME) intalled on your machine
#If you don't have MACQIIME installed, you can call the script
"extract_barcodes.py" from the lab's "Lab resources/Scripts/anaconda/bin"
shared folder. Download this folder and call the script from it locally.
#The program will create "read1.fastq", "read2.fastq", and
"barcodes.fastq". "The barcodes.fastq" file is the only useful file

cd gzdata_03
macqiime
python /Users/nguyenlab/Desktop/Casey/gzdata_03/bin/extract_barcodes.py --
fastq1 I1.fastq --fastq2 I2.fastq --bc1_len 8 --bc2_len 8 --input_type
barcode_paired_end

cd /Users/nguyenlab/Desktop/Casey/gzdata_03/bin/&&
python extract_barcodes.py --fastq1 I1.fastq --fastq2 I2.fastq --bc1_len 8
--bc2_len 8 --input_type barcode_paired_end

#REMOVE the extraneous files
rm reads1.fastq reads2.fastq I1.fastq I2.fastq

#COMPRESS the remaining files before importing to QIIME2

```

```

gzip *
cd..
#####
#IMPORT DATA
#####
#ACTIVATE the latest environment that QIIME2 was installed in
#You can list all discoverable environments with `conda info --envs`.
source activate qiime2-2019.4

-----
#IMPORT MULTIPLEXED DATA
-----
cd..
#IMPORT multiplexed sequence and barcode reads from a directory
#Your "gz_data" directory should contain only three files:
"forward.fastq.gz", "reverse.fastq.gz", and "barcodes.fastq.gz"
qiime tools import \
--type EMPPairedEndSequences \
--input-path gzdata_03 \
--output-path imported-paired-end-seqs_03.qza

#####next step done by previous pipeline (Lyon 16S)#####
#####skip to next step#####
#IMPORT DEMULTIPLEXED FILES
#Sometimes demux files are stored in multiple different folders. Use a
shell loop to move them all into one single folder to be imported into
qiime.

find . -name "*.gz" | while read file
do
    mv $file /Volumes/GoogleDrive/My\ Drive/Projects/C-MAIKI/c-maiki-
analysis/run1/demux
done

#CREATE a "fastq manifest" file in order to import multiple individual
files into QIIME
#Example file:
sample-id,absolute-filepath,direction
sample-1,$PWD/some/filepath/sample1_R1.fastq.gz,forward
sample-2,$PWD/some/filepath/sample2_R1.fastq.gz,forward
sample-1,$PWD/some/filepath/sample1_R2.fastq.gz,reverse
sample-2,$PWD/some/filepath/sample2_R2.fastq.gz,reverse

#####
#IMPORTING DATA
#####
#####

```

```

#ACTIVATE the environment that QIIME2 was installed in
source activate qiime2-2018.11
source activate qiime2-2018.8

##mainfest files created with shell see Nhus examples

###DELETED FILES #####
#missing file paths, may not have sequenced, deleted from manifest and
edited mapping file
101525, 49_80_r2
101589, 17_40_r2
101590, SynMockCom_r2

####Quality score length doesn't match sequence length for record
beginning on line 23277
101540, 21_80_r2

#####BELOW GAVE ERROR SEE ISHWORA ALTERNATIVE FOR OTHER OPTIONS #####
qiime tools import \
--type 'SampleData[PairedEndSequencesWithQuality]' \
--input-path manifest-lyon-ITS_03.csv \
--input-format PairedEndFastqManifestPhred33 \
--output-path demux-ITS_03.qza

#####GIVE ERROR Plugin error from demux: from first try with CMAIKI .gz
files

#####Compressed file ended before the end-of-stream marker was
reached
#####some of the fastq.gz files are corrupt, forums say most likely
during gzip step, need forward and reverse reads from rerun

#VIEW a summary of demultiplexed data
#Create a summary file
qiime demux summarize \
--i-data demux-ITS_03.qza \
--o-visualization demux-ITS_03.qzv

qiime tools validate demux-ITS_03.qza

qiime dada2 denoise-paired \
--i-demultiplexed-seqs demux-ITS_03.qza \
--p-trim-left-f 20 \
--p-trunc-len-f 250 \
--p-trim-left-r 20 \
--p-trunc-len-r 120 \
--o-representative-sequences rep-seqs-ITS_03.qza \
--o-table table-ITS.qza \
--o-denoising-stats denoising-stats-ITS_03.qza \
--p-n-threads 0 \
--p-n-reads-learn 1030000

```

```

#####
##### DID NOT USE ITSXPRESS TO TRIM SINCE FILES WERE ALREADY DEMUXED
#####
#####
#####                                     #####
#SUMMARIZE and view summaries of the FeatureTable (OTU table) and
FeatureData (representative seqs)
qiime feature-table summarize \
--i-table table-ITS_03.qza \
--o-visualization table-ITS_03.qzv \
--m-sample-metadata-file metadata_lyon_ITS_03.txt

#VIEW feature table summaries
qiime tools view table-ITS_03.qzv

#####COMBINE FEATURE TABLES FROM BOTH RUNS HERE#####
#####                                     #####
qiime feature-table merge \
--i-tables table-ITS.qza \
--i-tables table-ITS_03.qza \
--o-merged-table table.qza

qiime feature-table merge-seqs \
--i-data rep-seqs-ITS.qza \
--i-data rep-seqs-ITS_03.qza \
--o-merged-data rep-seqs.qza

```

APPENDIX E. Qiime 2.0 16S pipeline taken from Nhu Nguyen Microbiology lab

```
#####
# CREATE A QIIME METADATA FILE
#####
#The QIIME metadata file is a tab-delimited file that contains the
#necessary information regarding your experimental data.
#It is necessary for processing raw reads and perform basic analyses
#at least the following columns are required:

#SampleID      BarcodeSequence          LinkerPrimerSequence
#Treatment     Description
Heated40C.1    CGTACGATAAGTCGAG      NA
+40C           Something

#"#" defines the header line
#"SampleID", for clarity should be something that is informative towards
the experiment not just the sample number.
#"BarcodeSequence" for dual-barcoding should be concatenated into a single
string. The format should be ReverseComplementI2+I1.
#"LinkerPrimerSequence" is for 454 pyrosequencing. Not required for
Illumina data.
#"Treatment" is the basic treatment. Add as many columns as necessary for
your experimental needs.
#"Description" has to be at the end. It's not used in analyses and is
typically useless but it's required.

#Use Keemei (plugin) to validate your metadata file in Google Sheets. Make
sure that it is error free before going forward!
https://keemei.qiime2.org/

#####
#data was demuxed by Nhu and then added to "demux" folder using
shell command#####
#!/bin/sh
# !bash shell loop for finding files from all files in a subdirectory and
moving them to another directory

find . -name "*.gz" | while read file
do
  cp $file /Users/nguyenlab/Desktop/Casey/demux
done

#####
# IMPORTING DATA
#####
#ACTIVATE the environment that QIIME2 was installed in
source activate qiime2-2018.11
source activate qiime2-2018.8
```

```

#####
##### PREPARING YOUR RAW SEQUENCE DATA FOR DEMULTIPLEXING #####
#####
#DOWNLOAD your raw data into a folder. You should have 4 files: R1, R2,
I1, I2.
mkdir raw_data
cd raw_data

#UNZIP all files, saving the original files
gunzip -k *

#RENAME your raw data
mv Undetermined_S0_L001_I1_001.fastq I1.fastq
mv Undetermined_S0_L001_I2_001.fastq I2.fastq
mv Undetermined_S0_L001_R1_001.fastq forward.fastq
mv Undetermined_S0_L001_R2_001.fastq reverse.fastq

#MOVE them to the "gz_data" folder
cd..
mkdir gz_data
mv raw_data/I1.fastq demultiplex/I1.fastq
mv raw_data/I2.fastq demultiplex/I2.fastq
mv raw_data/forward.fastq demultiplex/forward.fastq
mv raw_data/reverse.fastq demultiplex/reverse.fastq

#EXTRACT barcodes from I1 & I2 files using macqiime (QIIME1)
#You will need the script extract_barcodes.py from QIIME1
#The program will create "read1.fastq", "read2.fastq", and
"barcodes.fastq" = which is the only useful file
cd gz_data
macqiime
extract_barcodes.py --fastq1 I1.fastq --fastq2 I2.fastq --bc1_len 8 --
bc2_len 8 --input_type barcode_paired_end

##### ALL OF ABOVE DONE BY NHU#####

#REMOVE the extraneous files
rm reads1.fastq reads2.fastq I1.fastq I2.fastq

#COMPRESS data to gz before importing to QIIME2
gzip forward.fastq reverse.fastq barcodes.fastq

cd..

#####
##### IMPORTING DATA #####
#####
#ACTIVATE the environment that QIIME2 was installed in
source activate qiime2-2018.8

```

```

#IMPORT multiplexed sequence and barcode reads from a directory
qiime tools import \
--type EMPPairedEndSequences \
--input-path gz_data \
--output-path imported-paired-end-seqs-NN.qza

#IMPORT DEMULTIPLEXED FILES
#Sometimes demux files are stored in multiple different folders. Use a
shell loop to move them all into one single folder to be imported into
qiime.

find . -name "*.gz" | while read file
do
    mv $file /Users/nguyenlab/Desktop/Casey/demux
done

#CREATE a "fastq manifest" file in order to import multiple individual
files into QIIME
#Example file:
sample-id,absolute-filepath,direction
sample-1,$PWD/some/filepath/sample1_R1.fastq.gz,forward
sample-2,$PWD/some/filepath/sample2_R1.fastq.gz,forward
sample-1,$PWD/some/filepath/sample1_R2.fastq.gz,reverse
sample-2,$PWD/some/filepath/sample2_R2.fastq.gz,reverse

#missing file paths, may not have sequenced, deleted from manifest and
edited mapping file
101568, 65_100
101581, 63_100
101583, 64_80

##mainfest files created with shell see Nhus examples

qiime tools import \
--type 'SampleData[PairedEndSequencesWithQuality]' \
--input-path manifest-lyon-16S_03.csv \
--input-format PairedEndFastqManifestPhred33 \
--output-path demux-16S_03_rerun.qza

#VIEW a summary of demultiplexed data
#Create a summary file
qiime demux summarize \
--i-data demux-16S_03_rerun.qza \
--o-visualization demux-16S_03_rerun.qzv

#VIEW the summary file and determine the quality of the sequences
qiime tools view demux-16S.qzv

#####
SEQUENCE QUALITY FILTER & DENOISE
#####
##### FILTER sequences (quality filtering) using DADA2

```

```

#Quality control (can be done on either multiplexed or demultiplexed
sequences)
#--p-n-reads-learn default [1M seqs = 250Mb]; this is ~10% of the
demultiplexed data. Adjust this value to correspond to your data. If your
data has < 10M seqs, use the default.
#--p-n-threads 0 = use all available cores; with 8 cores & 64GB of memory,
the single run took about 12 hours.

qiime dada2 denoise-paired \
--i-demultiplexed-seqs demux-16S_03_rerun.qza \
--p-trim-left-f 0 \
--p-trunc-len-f 249 \
--p-trim-left-r 0 \
--p-trunc-len-r 190 \
--o-representative-sequences rep-seqs-16S_03.qza \
--o-table table-16S_03.qza \
--o-denoising-stats denoising-stats-16S_03.qza \
--p-n-threads 0 \
--p-n-reads-learn 1030000

#TABULATE the denoising statistics
qiime metadata tabulate \
--m-input-file denoising-stats-16S_03.qza \
--o-visualization denoising-stats-16S_03.qzv

#VIEW denoising stats; if there is a huge drop in your sequences after
pairing, reconsider sequence trimming criteria.
qiime tools view denoising-stats-16S_03.qzv

#SUMMARIZE and view summaries of the FeatureTable (OTU table) and
FeatureData (representative seqs)
qiime feature-table summarize \
--i-table table-16S_03.qza \
--o-visualization table-16S_03.qzv \
--m-sample-metadata-file metadata_lyon_16S_03.txt #####issues getting to
read ids in metadata cant create table-16S.qsv

#VIEW feature table summaries
qiime tools view table-16S_03.qzv

#####
#####LEFT OFF HERE#####
#####

#####COMBINE FEATURE TABLES FROM BOTH RUNS HERE#####
qiime feature-table merge \
--i-tables table-16S.qza \
--i-tables table-16S_03.qza \
--o-merged-table table.qza

qiime feature-table merge-seqs \

```

```
--i-data rep-seqs-16S.qza \
--i-data rep-seqs-16S_03.qza \
--o-merged-data rep-seqs.qza
```